Orthopaedic Application of Magnetic Sensors

David Ayokunle Okhiria

Wolfson Centre for Magnetics

School of Engineering

Cardiff University

A thesis submitted for the degree of

Doctor of Philosophy

June 2017.

Acknowledgements

First and foremost, I am eternally grateful to the almighty God for seeing me through the period of this project. It definitely was not solely by my power or might.

I wish to thank my supervisors – Dr. Turgut Meydan, Dr. Paul Williams and Dr. Yevgen Melikhov, for their constant guidance, encouragement and criticism throughout the project. Their continuous input was crucial to the completion of this work.

I would like to thank Dr. Franck Lacan, for his assistance with the molding and sintering techniques used in this research. I am grateful to Mr Andrew Rankmore, Mr Ian King and the workshop staff for their assistance with the polyethylene sample fabrication and the loading tests performed. I appreciate the guidance of Dr Tomasz Kutrowski, for helping me understand LabVIEW software.

My gratitude also goes to my colleagues at the Wolfson centre – Dr. Vishu Goel, Gregory Moreton, Warrick Okolo, Dr. Jerome Cuenca and Dr. Hafeez Hashimdeen, for their continuous motivation throughout the duration of this project.

I wish to use this medium to appreciate my family, particularly my parents Prince Ayodele Okhiria (Snr) and Dr. (Mrs) Olusola Okhiria, for realising the potential in me and encouraging me to pursue success. Finally, and by no means the least, my appreciation goes to my lovely wife Seun for her unending love, support and encouragement over the years, and for the gift of my son Darryl.

Abstract

The purpose of this thesis is to propose a novel application of amorphous magnetic ribbons for use as knee force measurement sensors, without the need for secondary windings.

This thesis demonstrates that the magnetic properties of amorphous ribbons are retained when embedded in Ultra-high molecular weight polyethylene (UHMWPE) tibial inserts, and these properties can be interrogated non-invasively. This is of importance, as it offers a viable solution for instrumented prosthesis which can be used for in-vivo monitoring.

The research conducted also demonstrates that the tibiofemoral contact force on the instrumented tibial insert can be measured by observing the impedance changes in adjacent coils. Other conventional methods, though effective, require additional circuitry for non-invasive retrieval of measured data. The work contained herein eliminates this need, thereby reducing the structural modification of the implant required to accommodate the additional components.

This research also shows that the variation in the coil impedance can be related to the permeability changes in the amorphous ribbons, and these can be quantified by tracking the resonant frequency of the coils. Amorphous ribbons have not been used in monitoring orthopaedic prosthesis before, and this work shows how the simplified measurement system can offer an alternative technique to knee implant monitoring.

Table of Contents

Appendix 1: Manuscript titled **"**In vivo monitoring of orthopaedic implant wear using amorphous ribbons" by D. Okhiria, D.E. Giebaly, T. Meydan, S. Bigot and P. Theobald.

Appendix 2: Manuscript titled "Non-invasive measurement of stress levels in knee implants using a magnetic based detection method" by D. Okhiria, T. Meydan and P.I. Williams.

List of Figures

List of Tables

List of Abbreviations

AA	Anatomic axis
AC	Alternating current
ACL	Anterior Cruciate Ligament
ASTM	American Society for Testing Materials
CAD	Computer Aided Design
CBMS	Chill Block Melt Spinning
CoCr	Cobalt Chromium
CoCrMo	Cobalt Chromium Molybdenum
DMLS	Direct Metal Laser Sintering
DUT	Device Under Test
EMF	Electromotive Force
FEA	Finite Element Analysis
FEM	Finite Element Model
GUEPAR	Le Groupe pour l'Utilisation et l'Etude des Prosthèses Articulaires
HPDE	High Density Polyethylene
HSS	Hospital for Special Surgery
ICLH	Imperial College London Hospital
InSb	Indium Antimonite
KPI	Knee Prosthesis Instability
LC	Inductance-Capacitance
LCL	Lateral Collateral Ligament
LLW	Super low Pressure
LVDT	Linear Variable Differential Transformer
LW	Low Pressure
MA	Mechanical Axis
MCL	Medial Collateral Ligament
MS	Medium Pressure
Ni-Fe-Mo	Nickel-Iron-Molybdenum
OA	Osterarthritis
PA	Polyamide

PCL	Posterior Cruciate Ligament
PE	Polyethylene
PMMA	Polymethyl Methacrylate
RC	Resistance-Capacitance
RF	Radio Frequency
SLS	Selective Laser Sintering
TENS	Transcutaneous Electrical Nerve Stimulation
TKR	Total Knee Replacement
UHMWPE	Ultra High Molecular Weight Polyethylene
UK	United Kingdom

List of Symbols

A	Area
a	Lattice spacing
B	Magnetic flux density
C	Capacitance
e	Strain
E	Modulus of elasticity (Young's modulus)
E_{λ}	Magnetoelastic energy
E_{BW}	Bloch wall energy
E_{ex}	Exchange energy
E_H	Zeeman energy
E_k	Magnetocrystalline energy
E_m	Magnetostatic energy
f	Frequency (Hertz)
H	Applied magnetic field
H_d	Demagnetisation field
I	Current
J_{ex}	Exchange integral
K_1, K_2	First and Second order anisotropy constants
l	Length of conductor
L	Inductance
M	Magnetisation of material
m	Magnetic dipole moment
M_s	Spontaneous magnetisation
N	Number of turns
N_d	Demagnetisation factor
R	Resistance
$\boldsymbol{S}_i$, $\boldsymbol{S}_j$	Angular momenta of atoms
v_d	Domain volume
X_C	Capacitive reactance
X_L	Inductive reactance
$\boldsymbol{\alpha_1, \alpha_2, \alpha_3}$	Cosines of magnetisation vector angles

$\beta_1, \beta_2, \beta_3$	Cosines of strain direction angles
$\gamma_1, \gamma_2, \gamma_3$	Direction cosines between applied stress and cubic edges
δ	Domain wall width
θ	Angle between saturation magnetisation and stress directions
λ	Magnetostriction
λ_0	Spontaneous magnetostriction
$\lambda_{100}, \lambda_{111}$	Saturation magnetostriction coefficients measured along <100> and <111> directions
λ_S	Saturation magnetostriction
μ	Magnetic permeability
μ_0	Vacuum permeability
μ_r	Relative permeability
ρ	Resistivity
σ	Stress
Φ	Magnetic flux
$\boldsymbol{\Phi}$	Angle between momenta of atoms
χ	Magnetic susceptibility
ω	Angular frequency
ω_0	Natural resonant frequency

1. Introduction

Technological advancements in knee arthroplasty (replacement) have made it prevalent around the world, with over half a million primary procedures performed in England and Wales alone during the last decade [1]. It is a complex surgical procedure, requiring precise alignment of the new and existing bearing surfaces, in combination with accurate re-positioning of the associated connective tissues as shown in Figure 1.1. The number of total knee replacement (TKR) surgeries is constantly rising due to increased population and life expectancy rates; as well as a general decline in the age at the time of initial TKR. As a result of this, extensive research is being carried out on how to improve the survival rates and prolong the lifespan of the implant [2]. That cases often exceed 15 years longevity [2], is due to surgical skill, evolving component designs and the use of enhanced bearing materials that minimise the wearing of these critical surfaces. Polyethylene (PE) bearings are the most common, having evolved through ultra-height molecular weight (UHMWPE), highly cross linked, and now chemically-impregnated derivatives. Simulator and computational studies have demonstrated the superior tribological characteristics of these materials over extended time periods; however, such performance is only achieved within an optimal bio-mechanical environment [3]. The realities and complexities of orthopaedic surgery, however, means a proportion of all PE bearings experience stresses that fall outside of the optimal boundaries, typically as a consequence of minor implant malpositioning and/or soft-tissue imbalance. Such instances are likely to cause accelerated wear of the bearing surfaces and/or fracture, leading to premature failure [3].

The integrity of the bearing surfaces is critical to implant longevity. On-going monitoring is, however, problematic due to PE being radiolucent (i.e. invisible when viewed via x-ray), meaning that cases of accelerated implant wear may only be detected when the patient reports discomfort and/or pain. This pain is likely to be caused by the implant (aseptic) loosening, a severe and irreversible physiological response to foreign debris generated from abrasive wear in the UHMWPE. Indeed, implant loosening is one of the primary causes of premature implant failure [4]. Such instances require further surgery, with an increased morbidity and mortality risk, and significant financial cost.

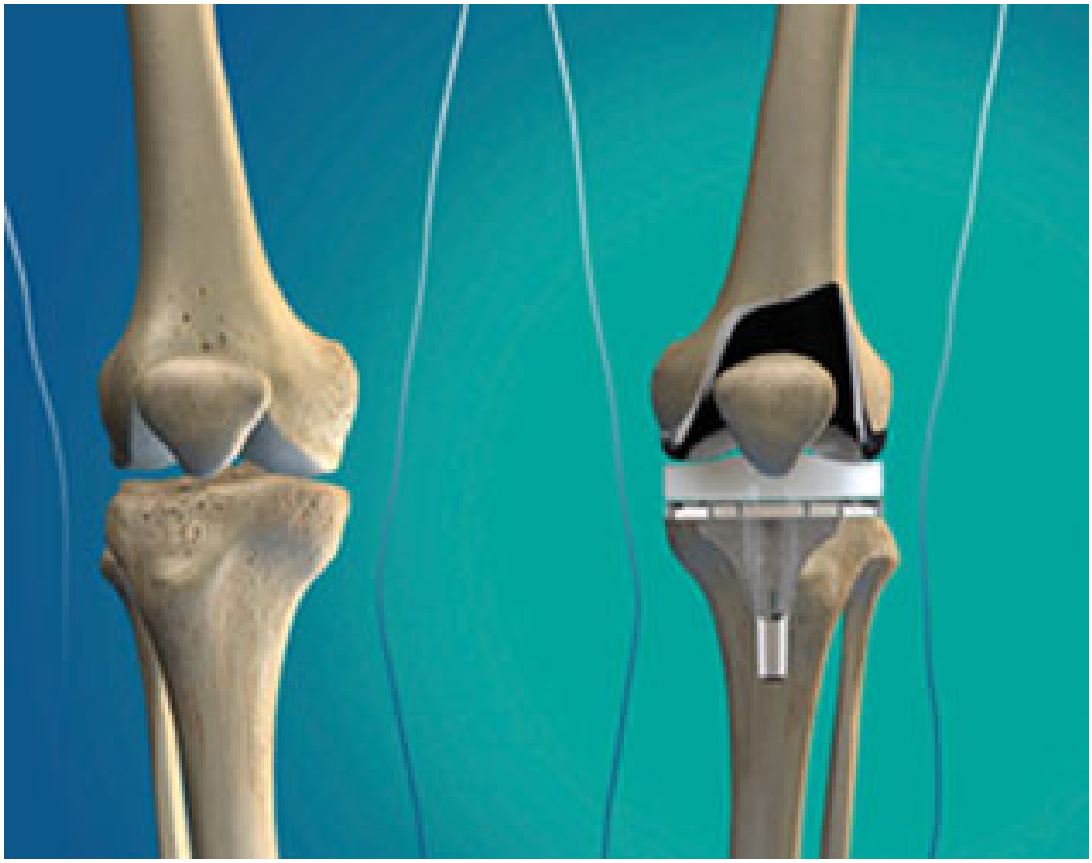

Figure 1.1 Knee joint before (left) and after (right) replacement surgery [5]

Therefore, effective monitoring of the active stresses within the UHMWPE insert can provide a clearer perception of knee biomechanics, and provide real-time observation on the condition of the knee implant. Early detection of high wear-rate cases would also allow for proactive treatment (physiotherapy, orthotics, etc.), providing the opportunity to avert premature implant failure.

International research groups have, for a number of years, been developing technologies to acquire highly valuable *in vivo* bio-mechanical data, and have achieved success across very small cohorts. Their techniques, however, typically require extensive retrofitting of strain gauges, batteries and antennae; many are only usable during the surgical process or require modifications to existing implant architecture and so are not viable solutions for mass-production [6] - [10]. One way around this is the utilisation of the magnetomechanical (Villari) effect exhibited by amorphous magnetic metallic glasses, in which their magnetic properties vary as a

function of mechanical strain. Magnetoelastic anisotropy is introduced in the amorphous material as a result of the strain, and this produces changes in its magnetic permeability. This effect has been researched extensively, and has been proposed as a basis for viable sensors [11] – [16].

The objective of this study is to integrate amorphous magnetostrictive ribbons in to UHMWPE as sensors, evaluating how the proportional change in their magnetic properties (with particular emphasis on the magnetic permeability) when subjected to a mechanical stress offers the potential to ultimately enable a mass-produced instrumented orthopaedic implant that may prevent premature failure. The intended implant would have the benefit of utilising low cost components, reduced circuitry and a non-invasive measurement technique, whilst maintaining the conventional implant design.

The literature review section of this thesis was split into two parts. Chapter 2 outlines the fundamental magnetic principles which form the basis for the sensing element used in this research. The characteristics and kinetics of the human knee joint are detailed in Chapter 3, along with the history, components and failure mechanisms associated with total knee replacement procedures. A summary of existing knee force measurement techniques is also contained within this chapter.

The experimental and results portion are split into four chapters. Chapter 4 deals with the measurement of permeability changes in amorphous ribbons due to mechanical stress whilst embedded in UHMWPE. These permeability variations induce changes in coil inductance which can be measured using a tuned circuit as depicted in the Chapter 5. Finite element modelling (FEM) was used to design and estimate the contact stresses, the results of these are presented in Chapter 6, while Chapter 7 describes experimental work carried out based on the modelled system including how these inductance changes can be easily tracked and related to the applied force or stress.

Chapter 8 presents a more detailed discussion of the results explained in Chapters 4 – 8, while the conclusions drawn and identified future work are contained in Chapter 9.

References

1. National Joint Registry for England, Wales, Northern Ireland and the Isle of Man, (2014). *11th Annual Report*. [online] Available at: http://www.njrreports.org.uk [Accessed 12 Dec. 2016].
2. Heinlein, B., Kutzner, I., Graichen, F., Bender, A., Rohlmann, A., Halder, A., Beier, A. and Bergmann, G. (2009). ESB clinical biomechanics award 2008: Complete data of total knee replacement loading for level walking and stair climbing measured in vivo with a follow-up of 6–10 months. *Clinical Biomechanics*, 24(4), pp.315-326.
3. D'Lima, D., Patil, S., Steklov, N., Slamin, J. and Colwell, C. (2006). Tibial Forces Measured In Vivo After Total Knee Arthroplasty. *The Journal of Arthroplasty*, 21(2), pp.255-262.
4. Arami, A., Simoncini, M., Atasoy, O., Hasenkamp, W., Ali, S., Bertsch, A., Meurville, E., Tanner, S., Dejnabadi, H., Leclercq, V., Renaud, P., Dehollain, C., Farine, P., Jolles, B., Aminian, K. and Ryser, P. (2011). Instrumented prosthesis for knee implants monitoring. *2011 IEEE International Conference on Automation Science and Engineering*.
5. Stutter Health CPMC (2015). *Knee joint before and after knee replacement surgery* [image] Available at: http://www.cpmc.org/learning/documents/knee_replacement.html [Accessed 5 Feb. 2017].
6. Taylor, S., Walker, P., Perry, J., Cannon, S. and Woledge, R. (1998). The forces in the distal femur and the knee during walking and other activities measured by telemetry. *The Journal of Arthroplasty*, 13(4), pp.428-437.
7. Kirking, B., Krevolin, J., Townsend, C., Colwell, C. and D'Lima, D. (2006). A multiaxial force-sensing implantable tibial prosthesis. *Journal of Biomechanics*, 39(9), pp.1744-1751.
8. Heinlein, B., Graichen, F., Bender, A., Rohlmann, A. and Bergmann, G. (2007). Design, calibration and pre-clinical testing of an instrumented tibial tray. *Journal of Biomechanics*, 40, pp. S4-S10.
9. Mohanty, L., Tjin, S., Lie, D., Panganiban, S. and Chow, P. (2007). Fiber grating sensor for pressure mapping during total knee arthroplasty. *Sensors and Actuators A: Physical*, 135(2), pp.323-328.

10. Hasenkamp, W., Thevenaz, N., Villard, J., Bertsch, A., Arami, A., Aminian, K., Terrier, A. and Renaud, P. (2013). Design and test of a MEMS strain-sensing device for monitoring artificial knee implants. *Biomedical Microdevices*, 15(5), pp.831-839.

11. Overshott, K. and Meydan, T. (1984). Unmagnetised amorphous ribbon transducers. *IEEE Transactions on Magnetics*, 20(5), pp.948-950.

12. Harada, K., Sasada, I., Kawajiri, T. and Inoue, M. (1982). A new torque transducer using stress sensitive amorphous ribbons. *IEEE Transactions on Magnetics*, 18(6), pp.1767-1769.

13. Seekircher, J. and Hoffmann, B. (1990). New magnetoelastic force sensor using amorphous alloys. *Sensors and Actuators A: Physical*, 22(1-3), pp.401-405.

14. Grimes, C., Roy, S., Rani, S. and Cai, Q. (2011). Theory, Instrumentation and Applications of Magnetoelastic Resonance Sensors: A Review. *Sensors*, 11(12), pp.2809-2844.

15. Grimes, C., Mungle, C., Zeng, K., Jain, M., Dreschel, W., Paulose, M. and Ong, K. (2002). Wireless Magnetoelastic Resonance Sensors: A Critical Review. *Sensors*, 2(7), pp.294-313.

16. Morón, C., Cabrera, C., Morón, A., García, A. and González, M. (2015). Magnetic Sensors Based on Amorphous Ferromagnetic Materials: A Review. *Sensors*, 15(11), pp.28340-28366.

2. Magnetism, Magnetostriction and Amorphous Metallic Materials

2.1 Synopsis

This chapter deals with the basic concepts of magnetism and the derivation of fundamental magnetic equations from first principles. The effects of stress on magnetism and vice versa in ferromagnetic materials are also discussed, as well as the intrinsic mechanisms influencing these phenomena. Finally, an overview of amorphous (glassy) metallic materials is provided, along with its characteristics and fabrication techniques.

2.2 Fundamental magnetic principles

One objective of the work carried in this research is to relate the changes in coil inductance to permeability variations of the material in its core. In doing this, a derivation of the correlation between these two quantities from first principles is necessary.

When a potential difference is applied across a conductor, the result is a movement of electrons through it. The stream of the electric charges carried by these electrons in motion causes a current, I (A) to flow in the conductor, and a corresponding magnetic field H (A/m) is generated in the region around it. Considering a symmetrical, circular current-carrying conductor with l length and N turns, the magnetic field produced can be related by the Maxwell-Ampere equation [1] as

$$H = \frac{NI}{l} \tag{2.1}$$

If this field is generated in a medium, the reaction of that medium to the field is its flux density (or magnetic induction) B, which can be defined as [2]

$$B = \mu H \tag{2.2}$$

with μ being the permeability, which is a measure of the capability of the medium to aid the formation of a magnetic field within itself. Ferromagnetic materials are

composed of singular randomly-magnetised domains which are oriented such that in the demagnetised state, the net magnetization within the material is approximately zero. Below the Curie point (the temperature at which they lose their magnetic characteristics), they exhibit spontaneous magnetisation and for such materials, Equation 2.2 becomes

$$B = \mu_0(H + M) \tag{2.3}$$

where μ_0 is the vacuum permeability, a physical constant equivalent to $4\pi * 10^{-7}$ (H/m) and *M* is the magnetisation of the material, which is defined as the density of the induced magnetic dipole moments (magnetic moments per unit volume) and is expressed as

$$M = \frac{m_m}{v} \tag{2.4}$$

where m_m is the magnetic dipole moments and v is the volume of the material. The magnetic field and the magnetisation are related by [1, 2]

$$M = \chi H \tag{2.5}$$

where χ is the magnetic susceptibility of the material. Thus, substituting Equation 2.5 into Equation 2.3 gives [1, 2]

$$B = \mu_0(H + \chi H) = \mu_0 H(1 + \chi) \tag{2.6}$$

The expression $(1 + \chi)$ is known as the relative permeability of the ferromagnetic medium μ_r. It should be noted that both μ_r and χ are tensors which describe the directionally-dependent response of the material to a magnetic field, while B and H are vectors. Comparing Equations 2.2 and 2.6,

$$\mu = \mu_0\mu_r \tag{2.7}$$

The flux density is defined as the amount of magnetic flux Φ, passing through a unit area A, given by [1, 2]

$$B = \frac{\Phi}{A} \tag{2.8}$$

For a solenoidal coil with *N* turns, an electromotive force (emf) is induced by the time-varying magnetic flux $^{d\Phi}/_{dt}$, which causes a current to flow through the coil in a

direction which opposes the initial flux. This is described by Faraday's second law of electromagnetic induction, and the induced emf which is measured in volts can be expressed as [3]

$$v = -N\frac{d\Phi}{dt} \tag{2.9}$$

The polarity (direction) of the emf is given by Lenz' law. Thus, fusing Equations 2.8 and 2.9,

$$v = -NA\frac{dB}{dt} \tag{2.10}$$

Now, incorporating Equations 2.1 and 2.7 into Equation 2.2, we obtain

$$B = \mu_0\mu_r\frac{NI}{l} \tag{2.11}$$

Substituting Equation 2.11 into 2.10,

$$v = -\frac{\mu_0\mu_r N^2 A}{l}\frac{dI}{dt} \tag{2.12}$$

In electromagnetics, a change in the current through an electrical conductor induces an emf in it which opposes the current change. This property is known as the inductance *L* (in Henries) and is related to the rate of change of the current by [4]

$$v = -L\frac{dI}{dt} \tag{2.13}$$

Combining Equations 2.12 and 2.13,

$$L = \frac{\mu_0\mu_r N^2 A}{l} \tag{2.14}$$

The equation above clearly illustrates the dependence of the inductance not only on the coil geometry, but also on the permeability of the magnetic core.

2.3 Magnetic domain theory

One of the peculiar characteristics of ferromagnetic materials is their unfilled 3d and 4f atomic subshells, which result in unpaired electron spins on adjacent atoms [5]. The exchange interaction between two adjacent spins is resisted by the thermal excitation

of the atoms caused by the rise in temperature, leading to the random orientation of the magnetic moments when the material is heated above its Curie temperature T_c [6, 7]. This temperature is material-dependent and above this temperature, the material exhibits paramagnetic properties.

During the cooling process of the material, the spins are rotated into a structured state. These spin motions are responsible for the magnetic moments within the bulk material, and they are aligned in small volumes known as domains [8] as depicted in Figure 2.1. These domains are formed in order to minimise the total energy and within each domain, the magnetic moments are oriented parallel to one another which results in spontaneous magnetisation even without an externally applied magnetic field. The spontaneous magnetisation is the sum of all magnetic moments *m* within the domain per unit volume, and can be given as

$$M_s = \frac{\sum m}{v_d} \tag{2.15}$$

where v_d is the volume of the domain. The spontaneous magnetisation is a vector quantity with a constant magnitude across all domains, although its direction varies between domains. The net magnetisation of the bulk material is the sum of the individual spontaneous magnetisation vectors, which is nearly zero in an un-magnetised specimen.

Domains are separated by walls, which are comparatively thin regions where the magnetic moments gradually transition between one orientation and the other [9, 10]. They can be categorised based on the angle of the magnetisation between the two neighbouring domains which the wall borders, as illustrated in Figure 2.2.

1. 90° wall: this is the boundary between two domains in which the magnetisation lies perpendicular to each another i.e. the magnetisation rotates by 90° from domain to domain.

2. 180° wall: this is the boundary between two oppositely magnetised domains. These can be further divided into two classes based on the plane of magnetisation rotation: Bloch walls and Neel walls, as illustrated in Figure 2.3. For Bloch walls, the magnetisation rotation is in a plane parallel to that of the domain wall whilst in Neel walls, it is perpendicular.

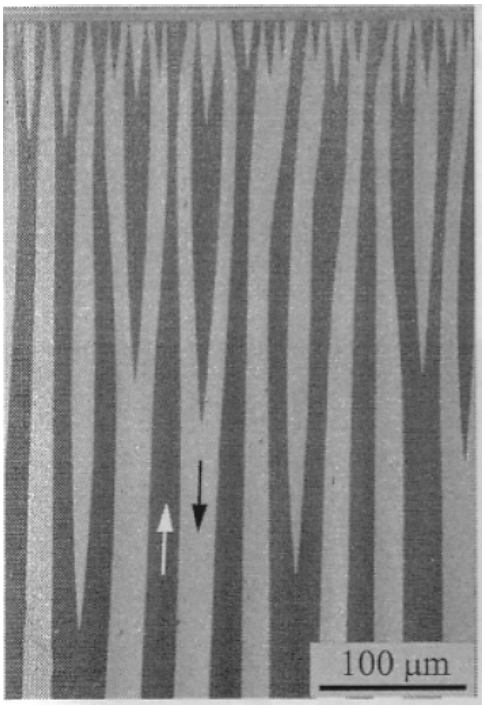

Figure 2.1 Illustrative representation of domain structure on the side plane of a Cobalt crystal. The directions of magnetisation are indicated by the arrows [11].

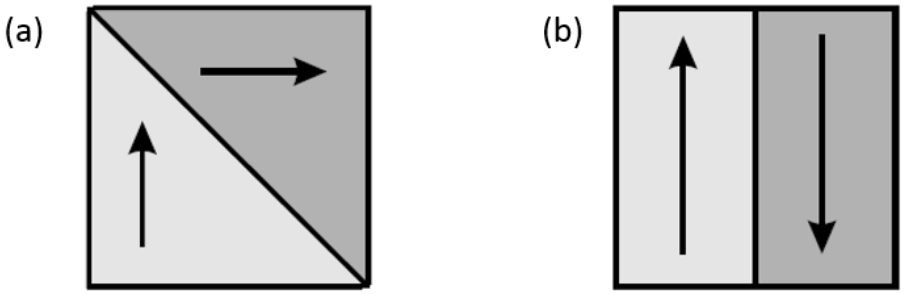

Figure 2.2 (a) 90^{o} and (b) 180^{o} domain walls [10]

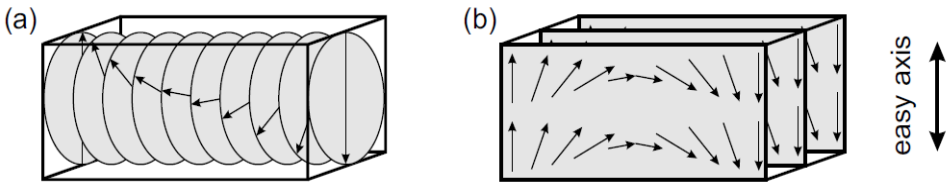

Figure 2.3 Magnetisation rotation in a (a) Bloch wall and (b) Neel wall [10]

Domain theory and micromagnetics are based on the same minimum energy principles which were derived from thermodynamics. The equilibrium domain structure of a material is one in which the free energy is minimised. As proposed by Landau and Lifshitz [12], the total free energy equation consists of five constituent magnetic energy densities: the exchange energy E_{ex}, magnetostatic energy E_m, magnetocrystalline anisotropy energy E_k, magnetoelastic energy E_λ, and the Zeeman energy E_H which is due to an externally applied magnetic field. Another term referred to as the domain wall or Bloch wall energy (E^{BW}) exists [1] and is regulated by the equilibrium between the exchange and magnetocrystalline anisotropy energies that create it. Thus, a robust equation for the total free energy can be expressed as

$$E_{total} = E_{ex} + E_m + E_k + E_\lambda + E_H \tag{2.16}$$

The Bloch wall energy often replaces E_{ex} and E_k in Equation 2.16. The individual energy densities are further discussed subsequently.

2.3.1 Exchange energy

The exchange energy is mostly dependent on the relative orientation of two adjacent atomic magnetic moments, and their propensity for parallel alignment. For two neighbouring atoms *i* and *j*, the exchange energy between them can be simplified as

$$E_{ex} = -2J_{ex}\boldsymbol{S_i}\boldsymbol{S_j} = -2JS^2\cos\phi \tag{2.17}$$

where J_{ex} is the exchange integral, $\boldsymbol{S_i}$ and $\boldsymbol{S_j}$ are the angular momenta of the atoms and ϕ is the angle between them [14]. It can be seen that for a positive value of J_{ex}, the exchange energy is minimum when the magnetic moments are parallel ($\phi = 0$, $\cos\phi = 1$) and maximum when they are antiparallel ($\phi = 180°$, $\cos\phi = -1$). Conversely, when J_{ex} is negative, the exchange energy is minimised when the magnetic moments are antiparallel. Therefore, in order for ferromagnetism to occur, the exchange integral needs to be positive.

2.3.2 Magnetostatic energy

As previously mentioned, the main purpose of magnetic domains is to minimise the free energy of the material. For a ferromagnetic material with a single domain which is uniformly magnetised along the easy axis, the associated magnetostatic energy is large. This is due to the generation of a demagnetising field by the formation of magnetic free poles at the surface of material, $\boldsymbol{H_d}$. This demagnetising field can be expressed as

$$\boldsymbol{H_d} = -N_d M \tag{2.18}$$

where N_d is the demagnetisation factor which is a tensor function dependent on the sample geometry, and M is the magnetisation that exists within the domain.

The division of the magnetisation into two antiparallel domains as shown in Figure 2.4 effectively halves the magnetostatic energy. This is due to the reduction in the demagnetising field, as a result of the reduced distance between oppositely polarised poles. Further splitting of the structure into four domains reduces the magnetostatic energy to about a quarter of the initial value.

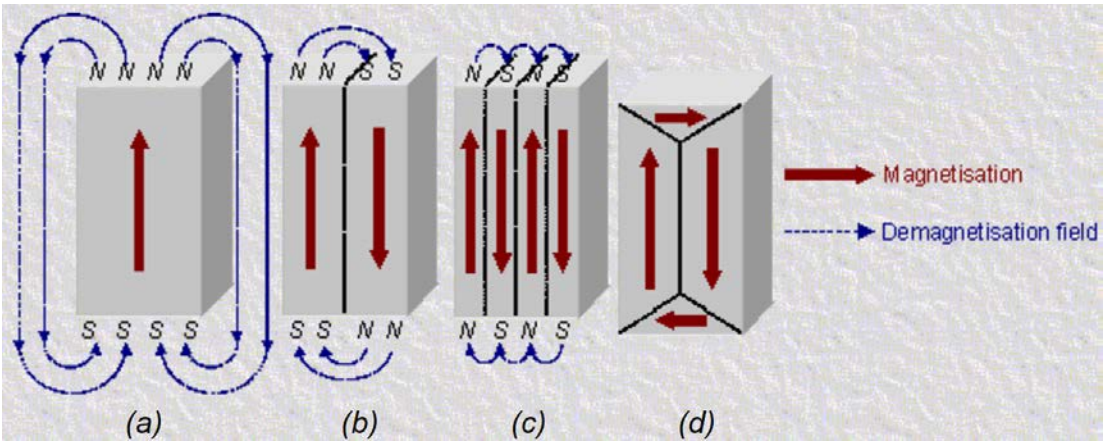

Figure 2.4 Schematic illustration of the division of magnetisation into domains (a) single domain (b) two domains (c) four domains and (d) closure domains [13]

The energy associated with the domain wall formation, which is proportional to the area of the wall, also adds to the overall energy. Hence, domain formation only proceeds provided the resultant reduction in the magnetostatic energy is greater than the energy required to form the domain wall. To reduce the magnetostatic energy, closure domains are formed on the surfaces as shown in Figure 2.4(d) which contain the magnetic flux within the material thereby cancelling out the free poles.

The magnetostatic energy density is given by [1]

$$E_m = -\left(\frac{\mu_0}{2}\right)\boldsymbol{MH_d} = \frac{\mu_0}{2}N_d M^2 \tag{2.19}$$

As E_m relates to self-energy, the factor of $^1/_2$ is introduced since the moments cannot be accounted for twice [1].

2.3.3 Magnetocrystalline anisotropy energy

Magnetisation in directions with an angular offset to the easy axis tend to necessitate larger applied fields in order to achieve saturation, and this is known as the magnetic anisotropy energy [1]. In other words, magnetocrystalline anisotropy occurs when there is a preferred direction of magnetisation. Considering a single cubic crystal, three principal crystallographic directions can be identified by their Miller indices (as shown in Figure 2.5) as:

- <100> consisting of [100], [010] and [001] which are the directions along the cubic edges of the unit cell
- <110> consisting of [110], [101] and [011] which are the directions along the diagonals of the cube faces
- <111> which is the direction along the diagonals of the unit cell

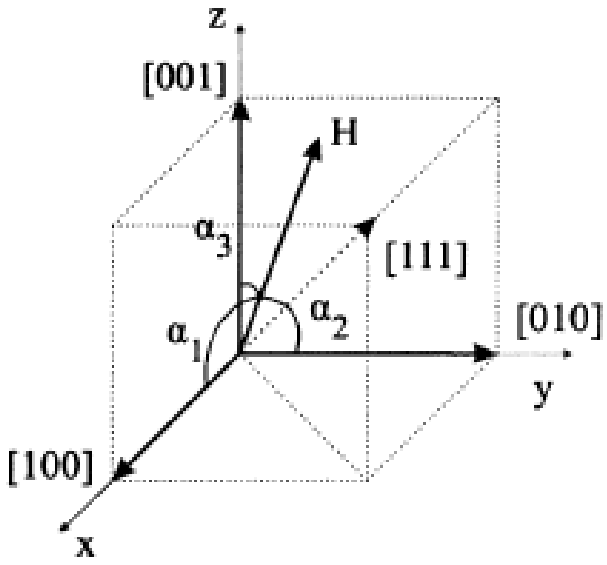

Figure 2.5 The direction cosines between the applied field and the principal crystallographic directions [14].

Magnetic saturation occurs at the lowest field strength when the field is applied along the easy magnetic axis. The <110> and <111> directions are known as the medium and hard magnetic axis respectively, as magnetisation in these directions requires increasingly higher fields. Considering α_1, α_2 and α_3 as the cosines of the angles the magnetisation vector subtends with the cubic orthogonal magnetic axes, the anisotropy energy (J/m^3) is denoted by

$$E_k = K_1(\alpha_1^2\alpha_2^2 + \alpha_2^2\alpha_3^2 + \alpha_3^2\alpha_1^2) + K_2(\alpha_1^2\alpha_2^2\alpha_3^2) \qquad (2.20)$$

where K_1 and K_2 are the first and second order materials anisotropy constants (J/m^3). It can be deduced from the equation that the anisotropy energy is minimal when the magnetic moments are all aligned along one of the easy directions.

2.3.4 Magnetoelastic energy

When a ferromagnetic material is magnetised, it exerts a stress against its surroundings which causes its dimensions to change as long as it is unrestrained [15]. This is referred to as magnetostriction, and it encompasses any effect which involves the collaboration between magnetisation and mechanical stress. It was first established by James Joule

in 1842, when he observed a change in the length of ferromagnetic bars in the direction of magnetisation.

When the magnetic moments are aligned, the initial length *l* of the material increases by a factor of Δl in the magnetisation direction when an external field is applied. This fractional change in length is known as magnetostriction $\boldsymbol{\lambda}$, and can be expressed as

$$\lambda = \frac{\Delta l}{l} \tag{2.21}$$

Magnetostriction is an intrinsic property of the material and can either be negative or positive, depending on whether the material length decreases or increases with an increasing applied field. In most materials, the rotation of the electron spins due to an externally applied field is usually quite small. When these spins lie parallel or antiparallel to the external field, no rotational force is exerted on them. This easy axis is defined as an energetically favourable direction of spontaneous magnetisation [9]. However, if the spins lie at an angle to the direction of the field, they rotate towards the field direction which results in a corresponding increase in the volume of the containing domain. Further increase in the external field causes the domains to align and eventually merge into a single domain (saturation) parallel to the external field direction. The magnetisation of the material reaches saturation when it becomes unaffected by increases in the external field [5].

The interaction between magnetic moments produces forces between the atoms, and this tends to introduce anisotropic strain in the domain structure of the bulk material. There are three mechanisms in which the strain emanates from:

i. **Spontaneous strain:** this is due to the alignment of the magnetic moments into domains when the material is cooled below its Curie temperature. At the onset of ferromagnetism, the material experiences spontaneous magnetisation at the domain level along with spontaneous strain *e* and magnetostriction λ_0 which are related by

$$\lambda_0 = \frac{e}{3} \tag{2.22}$$

Here, even though the magnetic moments are aligned within the individual domains, the domains themselves remain randomly oriented as shown in Figure 2.6(b).

ii. **Induced strain**: this is due to the alignment of the domains parallel to the direction of the externally applied field, as shown in Figure 2.6(c). At saturation, all domains within the material merge and are in line with the external field; the relationship between the spontaneous strain and the saturation magnetostriction λ_S is given by

$$\lambda_S = \frac{2e}{3} \tag{2.23}$$

which is simply the difference in strain between the demagnetised and saturated ferromagnetic states. The saturation magnetostriction in a single cubic crystal domain can be expressed using the Becker-Doring equation as

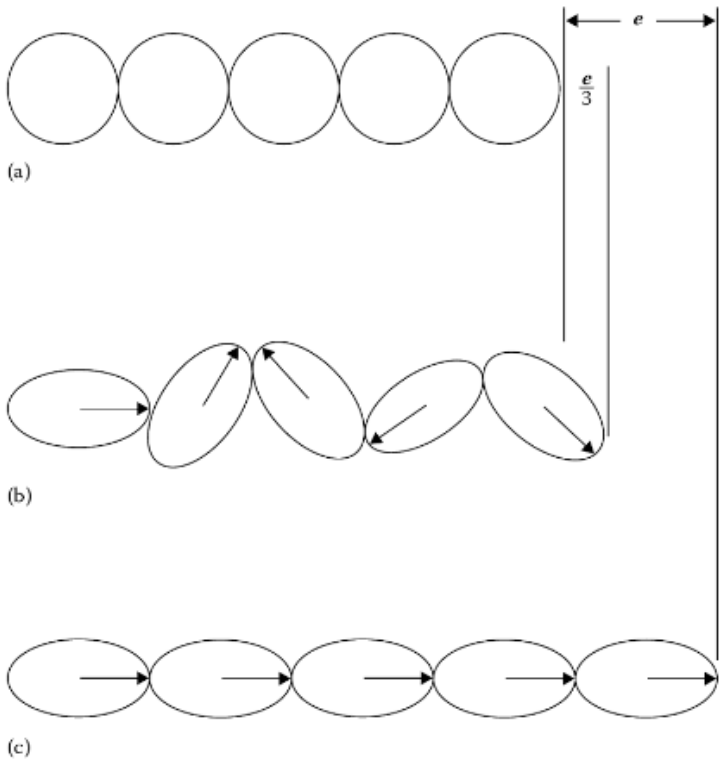

Figure 2.6 Schematic diagram depicting the magnetostriction in (a) the disordered paramagnetic state; (b) the demagnetised ferromagnetic state; and (c) the ferromagnetic state, magnetised to saturation [2].

$$\lambda_S = \frac{3}{2}\lambda_{100}\left(\alpha_1^2\beta_1^2 + \alpha_2^2\beta_2^2 + \alpha_3^2\beta_3^2 - \frac{1}{3}\right) + 3\lambda_{111}(\alpha_1\alpha_2\beta_1\beta_2 + \alpha_2\alpha_3\beta_2\beta_3 + \alpha_3\alpha_1\beta_3\beta_1) \quad (2.24)$$

with β_1, β_2 *and* β_3 being the cosines of the angles subtended by the strain direction with respect to the cubic edges; λ_{100} and λ_{111} being the saturation magnetostriction coefficients measured along the <100> and <111> directions. Saturation magnetisation is usually measured in the same direction as the applied magnetic field, which reduces Equation 2.24 to

$$\lambda_S = \frac{3}{2}\lambda_{100} + 3(\lambda_{111} - \lambda_{100})(\alpha_1^2\alpha_2^2 + \alpha_2^2\alpha_3^2 + \alpha_3^2\alpha_1^2) \quad (2.25)$$

iii. **Villari effect**: this is the inverse of the magnetostrictive effect as discovered by Emilio Villari in 1864, whereby a unidirectional mechanical stress causes a shift in the magnetic susceptibility of a material. This is due to a change in the direction of domain magnetisation, and the magnetoelastic energy which will be affected by the anisotropy and magnetostriction of the material is expressed as

$$E_i = K_1(\alpha_1^2\alpha_2^2 + \alpha_2^2\alpha_3^2 + \alpha_3^2\alpha_1^2) + K_2(\alpha_1^2\alpha_2^2\alpha_3^2) - \frac{3}{2}\lambda_{100}\sigma(\alpha_1^2\gamma_1^2 + \alpha_2^2\gamma_2^2 + \alpha_3^2\gamma_3^2) - 3\lambda_{111}\sigma(\alpha_1\alpha_2\gamma_1\gamma_2 + \alpha_2\alpha_3\gamma_2\gamma_3 + \alpha_3\alpha_1\gamma_3\gamma_1) \quad (2.26)$$

where γ_1, γ_2, and γ_3 are the direction cosines between the applied stress and the cubic edges. For an isotropic material, $\lambda_{100} = \lambda_{111} = \lambda_S$ and the last two terms of Equation 2.26 reduce to

$$E_\lambda = -\frac{3}{2}\lambda_S\sigma\cos^2\theta \quad (2.27)$$

where σ is the applied uniaxial stress, and θ is the angle between the saturation magnetisation and stress directions. It can be deduced from the Equation 2.27 that the magnetoelastic energy is minimised in a positive magnetostrictive material when the magnetisation lies parallel to the applied stress. Conversely, the magnetoelastic energy in negative magnetostrictive materials is minimal when the stress is perpendicular to the alignment of the magnetic moments.

2.3.5 Zeeman energy

This is also referred to as the external field energy, and is the potential interaction energy between the magnetisation vector and an externally applied field [11]. It is defined by the following equation

$$E_H = -\mu_0 H_{ext} M \cos\phi \tag{2.28}$$

where H_{ext} is the externally applied magnetic field, and ϕ is the angle subtended by the field and magnetisation. For a uniformly applied field, the energy is dependent only on the average magnetisation, and is irrespective of the domain structure or material shape [11]. The Zeeman energy in the material is minimised when the directon of magnetisation of the material lies parallel to the external field (i.e. $\cos\phi = 1$).

2.3.6 Domain Wall energy

The exchange energy between two adjacent magnetic moments is given as

$$E_{ex} = -2J_{ex}\boldsymbol{S_i}\boldsymbol{S_j} = -2JS^2\cos\phi \tag{2.29}$$

Using small angle approximation $\left(\cos\phi = 1 - {\phi^2}/{2}\right)$, E_{ex} can be re-written as

$$E_{ex} = -2JS^2 + JS^2\phi^2 \tag{2.30}$$

For a Bloch wall, the 180^o rotation takes place across *N* magnetic moments which makes the average angle between two moments ${\pi}/{N}$. If *a* is the lattice spacing, then each row of magnetic moments populates an area of a^2 on the surface of the wall. Therefore, the Bloch wall exchange energy density is given by [1]

$$E_{ex}^{BW} = JS^2\frac{\pi^2}{Na^2} \tag{2.31}$$

Also, the anisotropy energy density increases with *N* and can be approximated as

$$E_k^{BW} = K_1 Na \tag{2.32}$$

Combining Equations 2.31 and 2.32, the total wall energy becomes

$$E^{BW} = JS^2 \frac{\pi^2}{Na^2} + K_1 Na \tag{2.33}$$

It can be observed from Equation 2.33 that the exchange energy term prefers a large *N*, whilst the anisotropy energy density contrarily favours a smaller *N*. The equilibrium domain wall width is that which minimises the total wall energy, and this can be ascertained by equating the first derivative to zero. This gives

$$\frac{dE^{BW}}{dN} = -JS^2 \frac{\pi^2}{a^2} \frac{1}{N^2} + K_1 a = 0 \tag{2.34}$$

Therefore,

$$N_{eq} = \sqrt{\frac{JS^2\pi^2}{K_1 a^3}} \tag{2.35}$$

The domain wall width δ can be expressed as

$$\delta = N_{eq} a = \pi \sqrt{A/K} \tag{2.36}$$

where *A* is the exchange stiffness constant, which is an estimate of the rigidity of the magnetisation vector as a result of the exchange forces that encourage parallel alignment and is denoted by

$$A = \frac{JS^2}{a} \tag{2.37}$$

2.4 Amorphous magnetic materials

Amorphous ferromagnetic materials are an important class of materials which have been exploited in a diverse range of magnetic applications [16 - 20]. The word "amorphous" was derived from the Greek language, the prefix *a* meaning without, and *morphe* which means form or shape. Therefore, amorphous materials have no defined crystalline structure at the macroscopic level; however, varying degrees of short range (atomic scale) order does exist within the material depending on the type of atomic bonding present. They are usually produced by sputtering or rapid solidification techniques which typically require high cooling rates (between 10^4 to 10^6 C/s), and this facilitates the formation of an order similar to that of the molten alloy.

The amorphous (glassy) state of the material is normally sustained by alloying the metallic elements with glass formers (metalloids) like boron, silicon, carbon and phosphorus. There are various chemical configurations for producing these amorphous alloys, but those of magnetic significance are based either on *3d* transition metals or rare earth metals. The basic configuration for ferromagnetic alloys is $T_{100-x}M_{x,}$ where T depicts one or more metallic components and M represents one or more metalloids with $15 < x < 30$ % approximately [1].

2.4.1 Properties of amorphous materials

The absence of a long-range ordered atomic structure in amorphous metallic alloys as depicted in Figure 2.7 leads to many features which are favourable for assorted applications. At the macroscopic level, magnetostriction is isotropic [21] and the magnetocrystalline anisotropy is nearly zero which makes magnetisation rotation easy. However, residual stresses during the manufacturing process introduce a minor uniaxial anisotropy along the material axis, although this can be suppressed by annealing (heating the material to temperatures between 150^{o}C and 250^{o}C).

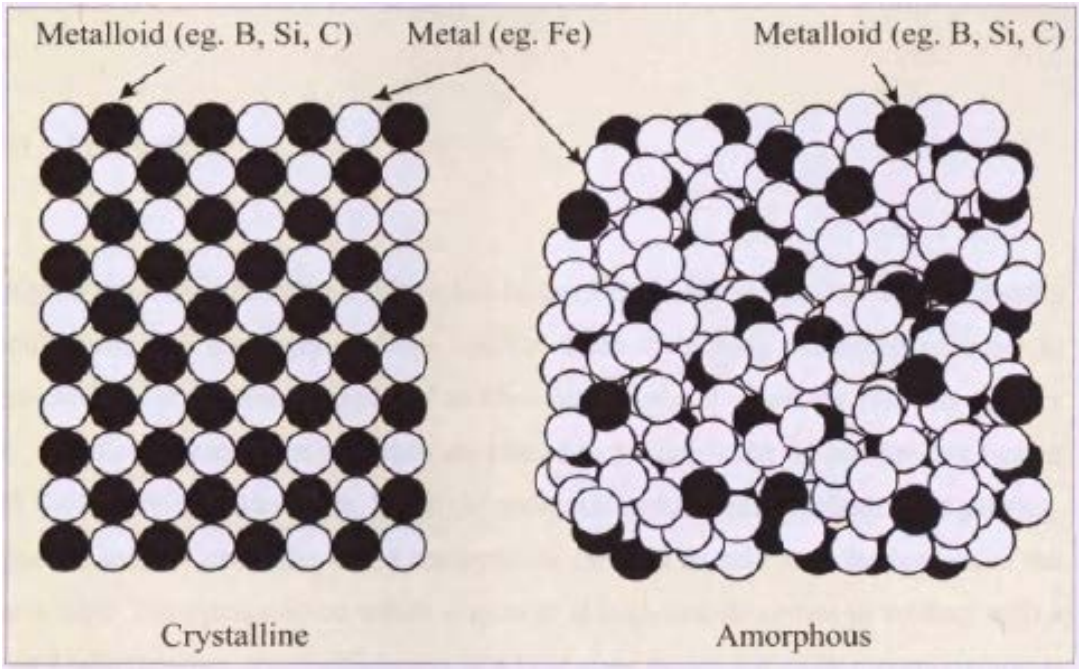

Figure 2.7 Configuration of individual atoms within crystalline and amorphous structures [22]

Electron scattering, which arises from the atomic disarray, produces high electrical resistivity in the material ($\rho \approx 100 - 200\ \mu\Omega.cm$) and this is beneficial in high frequency magnetisation reversal for eliminating eddy currents. Also, amorphous alloys tend to have higher relative permeability in comparison to typical ferromagnetic materials [23] due to the lack of magnetocrystalline anisotropy, and this makes them easier to magnetise.

The mechanical properties of the amorphous material are also enhanced. As they are devoid of a defined crystalline structure through which dislocation motion would be comparatively easy, they possess high values of Young's modulus and tensile strength. This in turn increases their elastic and bending fatigue limits with little plastic deformation, and makes them less susceptible to magnetic deterioration during cyclic loading. In addition, they are homogenous and possess no microstructural discontinuities (for example, grain boundaries) through which impurities can penetrate, hence they are highly resistant to corrosion.

2.4.2 Fabrication of amorphous materials

There are various methods by which amorphous metallic alloys can be produced, in both ribbon and wire forms. These include deposition (vacuum, sputter, electro and chemical) as well as melt spinning, all of which involve rapid cooling rates as this is a necessary condition for attaining an amorphous state. Of all the techniques mentioned, chill block melt spinning (CBMS) is the most widely employed method for mass production of amorphous ribbons in uninterrupted lengths.

In this technique, the constituent materials are deposited into a quartz crucible and then heated until liquefaction. Using pressure from an inert gas (e.g. argon), the liquid metal is then ejected through an aperture at high speed onto the circumferential surface of a water-cooled rotating drum. A pool of liquid forms at the end of the liquid stream, and the ribbon is then drawn out from underneath [24]. A schematic diagram of this process is shown in Figure. 2.8, and an amorphous ribbon sample shown in Figure 2.9.

Experimental studies have been carried out based on sweeping different cast and melt parameters. These include the melt viscosity, melt pool dimensions, volumetric flow

rate, ejection pressure, nozzle diameter, wheel surface velocity, and injection angle. The ribbon geometry has been shown to vary as a function of these parameters [24].

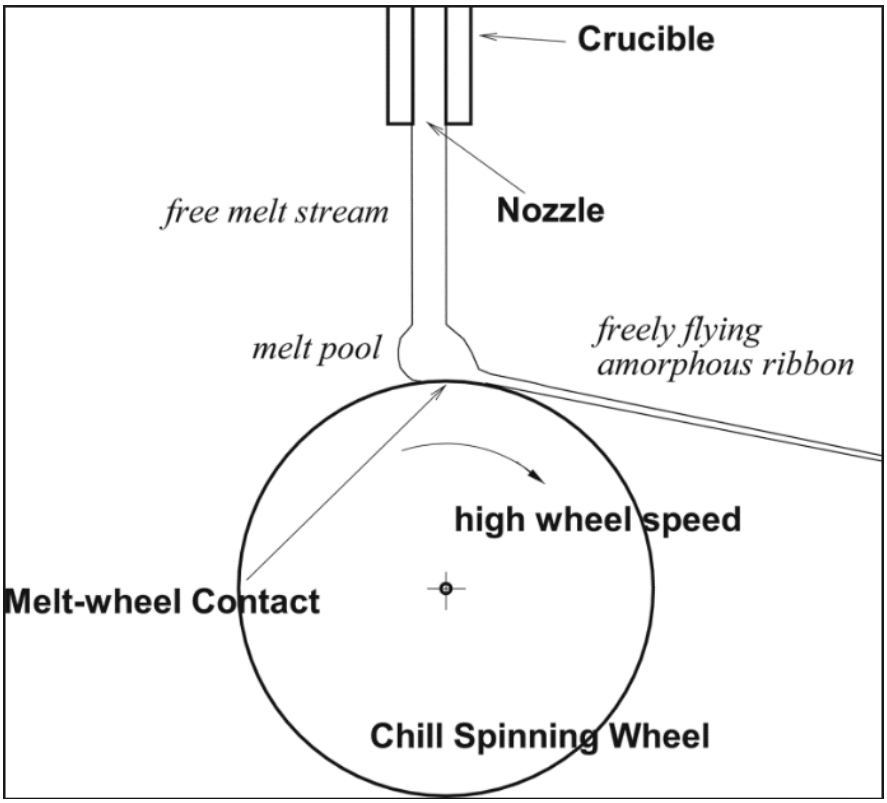

Figure 2.8 Schematic diagram showing Chill Block Melt Spinning process [25]

Figure 2.9 Sample of amorphous ferromagnetic ribbon

References

[1] O'Handley, R. (2000). *Modern magnetic materials*. New York: Wiley.

[2] Jiles, D. (1998). *Introduction to magnetism and magnetic materials*. London:Chapman and Hall.

[3] Bakshi, U. and Bakshi, M. (2008). *Magnetic circuits and transformers*. Pune: Technical Publications, Ch. 3, pp. 2-9.

[4] Horowitz, P. and Hill, W. (1989). *The art of electronics*. Cambridge [England]: Cambridge University Press, Ch. 1, pp. 28-35.

[5] Cullity, B. and Graham, C. (2009). *Introduction to magnetic materials*. Hoboken, N.J.: IEEE/Wiley.

[6] Cullity, B. (1972). *Introduction to magnetic materials*. Reading, Mass.: Addison-Wesley Pub. Co, pp.248-284.

[7] P. Curie, "*Lois expérimentales du magnétisme. Propriétés magnétiques des corps à diverses temperatures*", The Annual Review of Physical Chemistry, vol. 5, pp. 289-405, 1895.

[8] P. Weiss, "*L'hypoth`ese du champ mol´eculaire et la propriet´e ferromagnetique*". Journal de Physique, vol. 6, pp. 661–690, 1907.

[9] Chikazumi, S. (2005). *Physics of ferromagnetism*. Oxford [u.a.]: Oxford Univ. Press, pp.407-428.

[10] Getzlaff, M. (2008). *Fundamentals of magnetism*. Berlin: Springer, pp.117-124.

[11] Hubert, A. and Schäfer, R. (2009). *Magnetic Domains*. 3rd ed. Berlin [etc.]: Springer.

[12] Landau, L. and Lifshitz, E. (1935). On the theory of the dispersion of magnetic permeability in ferromagnetic bodies. *Die Physikalische Zeitschrift der Sowjetunion*, 8, pp.153 - 169.

[13] Gitam.edu (2016). *Contents*. [Online] Available at: http://www.gitam.edu/eresource/Engg_Phys/semester_2/magnetic/domain.htm [Accessed 31 Oct. 2016].

[14] Hon Fai, L. (1995). *Magnetic domains observation in structural steels under stress*. Ph.D. Cardiff University.

[15] Lee, E. (1955). Magnetostriction and Magnetomechanical Effects. *Reports on Progress in Physics*, 18(1), pp.184-229.

[16] Hasegawa, R. (2001). Applications of amorphous magnetic alloys in electronic devices. *Journal of Non-crystalline Solids*, 287(1-3), pp.405-412.

[17] Marin, P. and Hernando, A. (2000). Applications of amorphous and nanocrystalline magnetic materials. *Journal of Magnetism and Magnetic Materials*, 215-216, pp.729-734.

[18] Overshott, K. and Meydan, T. (1984). Unmagnetised amorphous ribbon transducers. *IEEE Transactions on Magnetics*, 20(5), pp.948-950.

[19] Seekircher, J. and Hoffmann, B. (1990). New magnetoelastic force sensor using amorphous alloys. *Sensors and Actuators A: Physical*, 22(1-3), pp.401-405.

[20] Harada, K., Sasada, I., Kawajiri, T. and Inoue, M. (1982). A new torque transducer using stress sensitive amorphous ribbons. *IEEE Transactions on Magnetics*, 18(6), pp.1767-1769.

[21] Göpel, W., Hesse, J., Zemel, J., Boll, R. and Overshott, K. (1989). *Sensors, A comprehensive study, Volume 5, Magnetic sensors*. Weinheim: VCH, p.98.

[22] Katranas, G. (2006). *Design and development of bilayer sensor systems for biomedical and automotive applications*. Ph.D. Cardiff University.

[23] Metglas, Inc. *Magnetic materials*. [online] Available at: https://metglas.com/magnetic-materials/ [Accessed 5 Jan. 2017].

[24] Kukulka, D., Poopisut, A. and Mollendorf, J. (1996). New chill-block melt spinning relations to predict ribbon thickness. *Journal of Thermophysics and Heat Transfer*, 10(3), pp.545-547.

[25] Wang, C. and Mitra, A. (2014). Numerical and Analytical Modeling of Free-Jet Melt Spinning for Fe 75 −Si 10 −B 15 (at. %) Metallic Glasses. *J. Heat Transfer*, 136(7), p.072101.

3. Knee mechanics and arthroplasty

3.1 Synopsis

The purpose of this research is to develop a system for measuring forces in total knee replacements. To put this into context, a good understanding of the joint behaviour is necessary. This chapter details the loading and kinematics the knee is subjected to, along with a summary of the main factor necessitating replacement surgery. The knee prosthesis is also described, as well as the root causes of implant failure. Finally, a detailed description of existing force measurement techniques is presented.

3.2 The Human knee joint

The knee is one of the largest and most complicated joints in the human body [1-3]. It is tricompartmental in nature, connecting the femur (thighbone), tibia (shinbone) and patella (kneecap) [4]. Figure 3.1 depicts the anatomy of a typical human knee joint. The femoral condyles, which are two rounded prominences on the distal end of the femur, articulate with the tibial plateaus through the tibial and lateral menisci. These menisci are crescent-shaped, rubbery fibrocartilages that act as shock absorbers between the femur and tibia, provide lubrication and make the joint more conforming [4, 5]. The patella, which is a sesamoid bone (embedded within a tendon), lies anterior to the knee surface. It articulates with the femur in the trochlear groove and the groove geometry and quadriceps muscles mutually govern its movement.

The cruciate and collateral ligaments bond and stabilise the tibiofemoral joint. The anterior and posterior cruciate ligaments (ACL and PCL) maintain the anterior-posterior sliding constraint in the tibia, with the ACL particularly preventing hyperextension of the knee. Conversely, the medial and lateral collateral ligaments (MCL and LCL) maintain varus-valgus constraint in the coronal plane. A thin layer of hyaline cartilage covers the articulating surfaces of each joint, which provides superior lubrication and safeguards them from damage [6]. Like all other synovial joints, a joint capsule envelopes the bones in the knee joint. This capsule consists of an outer fibrous layer of collagen connected to the knee ligaments, and an inner membrane that secretes lubricating synovial fluid to reduce friction and wear in the joint [7, 8].

Besides these, various critical structures also surround the knee which aid in softening the effects of friction and external stress. Bursae, which are small sacs of synovial fluid, encompass the knee to reduce friction [9, 10]. Articular fats pads composed of adipose tissues also help absorb shock from extrinsic stress and provide improved stability by filling empty spaces created during knee motion [11].

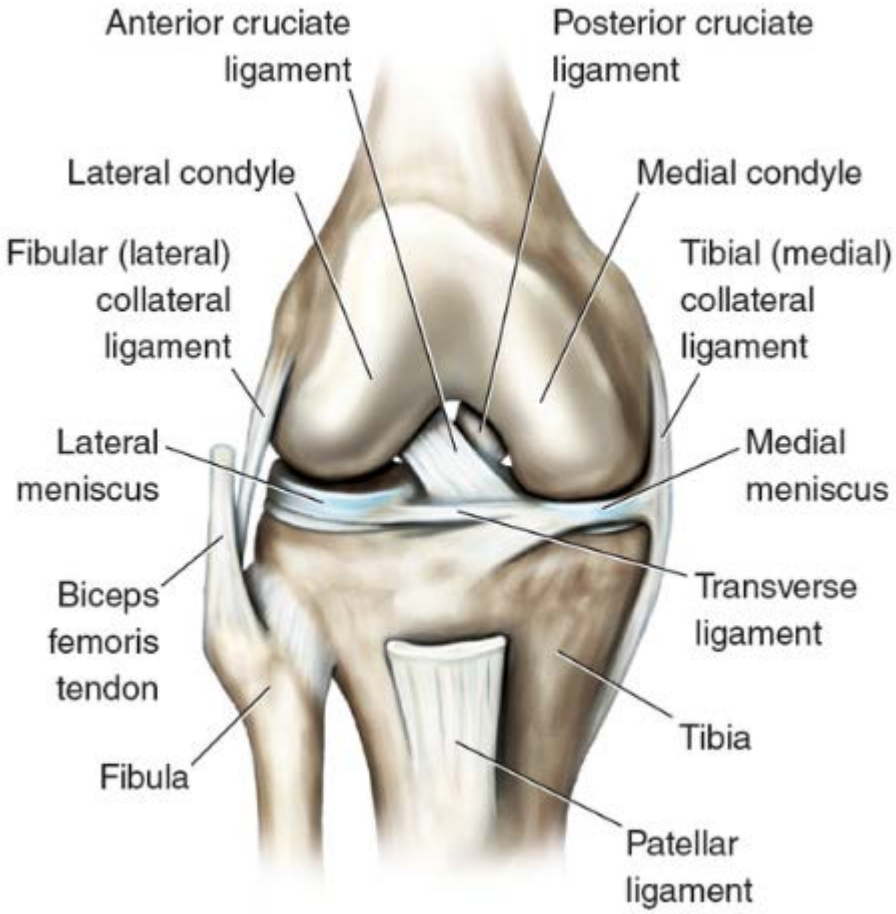

Figure 3.1 Anatomy of the human knee joint [12]

3.2.1 Knee kinematics

The knee joint is trocho-ginglymus in nature, a combination of a hinge and pivot joint that has rolling, sliding and rotational motions [13]. The tibiofemoral joint has six degrees of freedom, comprising three rotational and three translational motions [4, 14], as shown in Figure 3.2. This is because of the flexibility of the cartilages between the articulating surfaces of the bones in the joint. The rotational motions include

flexion-extension, internal-external (axial) and varus-valgus (adduction/abduction). The translations exist in the anterior-posterior and medial-lateral directions which are shown in Figure 3.3, as well as compression and separation of the joint.

The primary motion in the knee joint is flexion and extension. The typical range is from full extension to about 160^{o} fully flexed in the sagittal plane, with a small measure of hyperextension (between 3-5^{o}) also achievable [4]. Axial rotation of the femur is also largest when the knee is flexed at 90^{o} and least when the knee is in full extension due to soft tissue restriction.

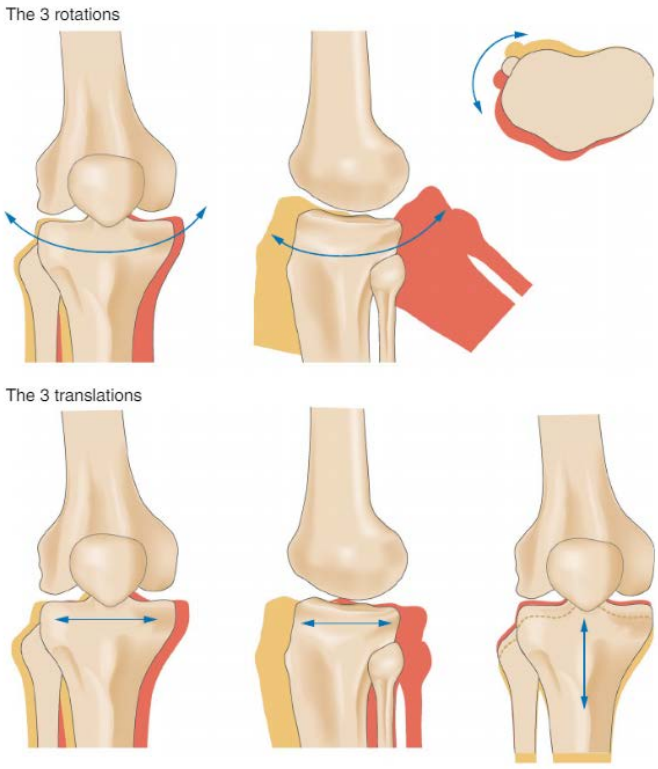

Figure 3.2 Degrees of freedom of the knee joint [15]

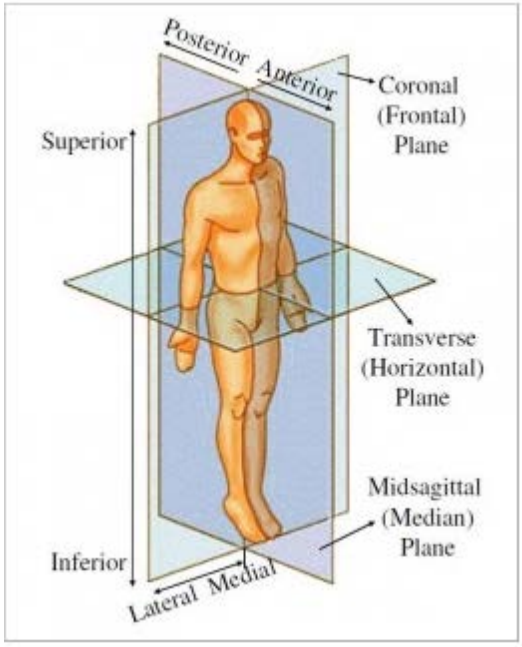

Figure 3.3 Anatomical planes of the human body [16]

3.2.2 Knee loading

The resultant forces and moments acting on the knee joint are dependent on the task embarked upon at any instant. These have previously been ascertained using motion analysis, and results achieved for different tasks such as walking, sitting, standing and even sporting activities [17 - 22].

The quadriceps and hamstrings respectively supply the extension and flexion moments. The maximum axial load in the joint, which is approximately the contact force whilst neglecting soft tissue loading, is commonly expressed as a multiple of the bodyweight. For instance, contact force has been determined to be between three to four times average bodyweight in the normal gait cycle and is the generally accepted standard in total knee replacement designs [23]. Table 3.1 contains typical values obtained from research into load bearing of the knee for different activities.

Table 3.1 Statistics relating to knee joint loading during various activities [17 – 22]

Research	Activity	Peak tibiofemoral force (x Bodyweight)
Kuster et al (1997)	Level Walking Downhill Walking	3.4 (male) 3.9 (female) 7 (male) 8 (female)
Costigan et al (2002)	Stair Climbing	3 - 6 (Mixed Sex)
Christina & Cavanagh (2002)	Stair Decent	1.4 - 1.48 ± 0.20 (mixed sex aged 21-27) 1.43 - 1.50 ± 0.27 (mixed sex aged 71-75)
Nisell and Ericson (1992)	Jogging Running	12 (male) 7.5 (male)
Kutzner et al (2010)	Stair descending Stair ascending Level walking One legged stance Knee bending Standing up Sitting down Two legged stance	3.46 3.16 2.61 2.59 2.53 2.46 2.25 1.07
D'lima et al	Walking, stair climbing, chair rise, squat	2 – 3

3.3 Osteoarthritis

Long-term degeneration of the joints is inevitable in almost all individuals. Osteoarthritis (OA), which is one of the most common forms of arthritis [24, 25], is the continuous deterioration of the articular cartilage due to some amalgamation of mechanical and biochemical wear, as depicted in Figure 3.4. It is a concentrated effect, and is one of the principal causes of the requirement for replacement surgery in knee joints. Since 2003 when orthopaedic data compilation began in the UK, over 96% of primary knee replacement surgeries performed as at the end of 2015 were attributed to osteoarthritis [26].

The gradual degeneration of the cartilage may be due to normal wear and tear brought about by daily activities, injury or disease. OA can also be caused by repetitive stress to articulating surfaces of the joint, or any external trauma that alters its normal functioning. Other factors like age and obesity are also believed to increase the

probability of developing OA [27, 28]. The associated symptoms include joint pain and stiffness, inflammation, deformation, slight swelling, reduced range of motion and creaking of the joint [29, 30].

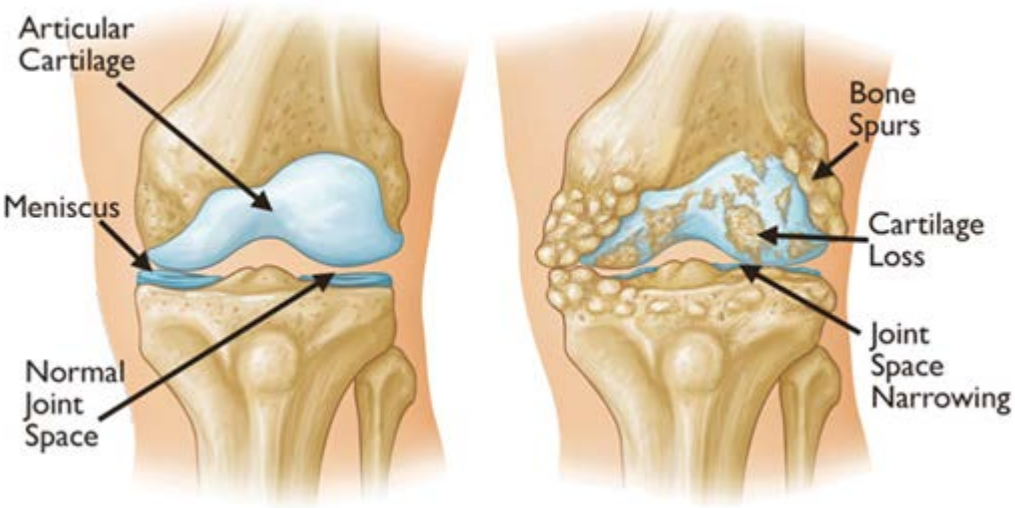

Figure 3.4 Normal joint space between the femur and the tibia (Left). Decreased joint space due to damaged cartilage and bone spurs (Right) [31]

Although there is no complete cure for OA, milder symptoms are still manageable through lifestyle changes. These include weight loss, physiotherapy and medication (analgesics, steroid injections and non-steroidal anti-inflammatory drugs). Additionally, pain relief is achievable by using transcutaneous electrical nerve stimulation (TENS) which sends pulses to the brain and modifies the pain messages received by the brain [32, 33]. However, in more severe cases where quality of life is significantly affected, replacement surgery is usually recommended.

3.4 Brief History of Total Knee Replacement (TKR)

A German surgeon and physician, Themistocles Gluck, is generally regarded as a pioneer in the use of endoprosthetes by conducting the first ever knee replacement in 1890 [34]. He accomplished this feat using a hinged ivory implant and bone cement consisting of colophony, pumice and gypsum. A diagram of the implant materialised

is shown in Figure 3.5. Although his methods proved to be inadequate due to infection caused by the ivory and the weakness of the bone cement to the applied knee forces, most of the fundamental concepts used in contemporary implants had already been visualised by him. These include elemental design of implants, osseointegration (where bone ingrowth solely determines the implant stability), biocompatibility and structural properties of materials, and allotransplantation.

After Gluck's initial design, different scientists made various efforts to both understand and replicate the motions of the knee joint. In the early 1950s, a Swedish scientist named Borje Walldius designed a cobalt chrome alloy roller bearing implant (Figure 3.6a), later modified to include a patellar flange and longer stems for the supporting bone structures [35 – 38]. In that same decade, Shiers developed a hinged prosthesis with an even longer tibial stem (Figure 3.6b) for better alignment and a posterior roller bearing joint [39 – 40]. McKee, an English scientist from Norwich, also developed an implant similar in design to the Walldius hinge (Figure 3.6c); however, screws initially secured the stem to the bone [41]. This was then modified to incorporate a tapered tri-fin blade stem with cemented fixation, the rationale for this being improved load distribution.

In 1969, a group of French surgeons known as Le groupe pour l'utilisation et l'étude des prosthèses articulaires (GUEPAR) introduced their eponymous hinged prosthesis (Figure 3.6d) [42] which was fleetingly popular, but was plagued by undesirable loosening and infection due its inadequate capacity for intricate knee forces. That same year, the Royal National Orthopaedic Hospital group presented the Stanmore hinge (Figure 3.6e), which consisted of titanium stems, cobalt chromium molybdenum (CoCrMo) alloy roller bearing system with a high-density polyethylene (HPDE) insert [43].

Even though hinged knee prostheses proved to be significant in the developmental cycle of TKR, they were not without flaws. Due to insufficient understanding of the leg alignment, the designs did not incorporate valgus stems. The constrained nature of the hinge could not accommodate the complex rotations of the knee joint; hence, loosening and mechanical failure rates were high. In addition, the surgical process of fitting the prosthesis required the excision of a considerable volume of bone, which made the joint difficult to salvage during revision procedures in the event of failure.

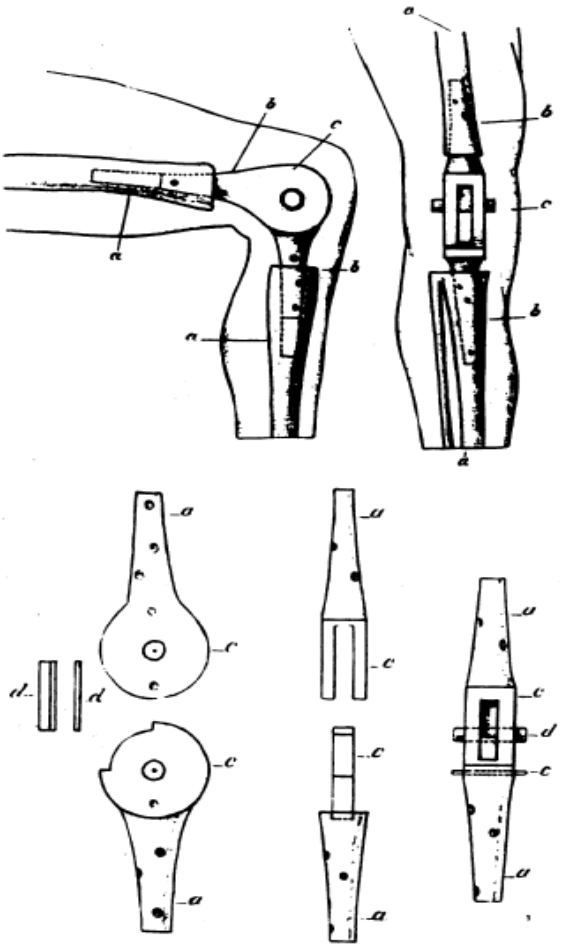

Figure 3.5 Gluck's ivory knee replacement assembled (Top) and its constituent parts (Bottom) [34]

The polycentric knee prosthesis designed by Frank Gunston, a Canadian-born engineer and doctor, was the first to consider the natural knee biomechanics [44]. It comprised two separate semi-circular stainless steel runners secured into slots in the articulating surfaces of the femoral condyles, coupled with two concave HDPE tracks fixed into slots in the tibial plateaus (Figure 3.7). Both components attached to the bones using self-curing polymethylmethacrylate (PMMA) cement. Post-operative results were remarkable, as better physiological stability and movement range were achieved due to the retention of the cruciate and collateral ligaments. In addition, the design allowed the centre of rotation to vary with knee flexion; hence, it was able to replicate the intricate gliding and rocking motions in the joint better. Unfortunately, the narrow femoral components subjected the polyethylene tracks unfavourably high pressure points.

A collaboration between Dr Michael Freeman and Alan Swanson of the Imperial College London Hospital (ICLH) produced the first condylar knee arthroplasty in 1970 [45]. The Freeman-Swanson (later ICLH) knee prosthesis consisted of a cobalt chromium femoral component, and a shallow-grooved HDPE tibial tray initially including two staples for additional stability (Figure 3.8) that were later discarded in subsequent models. This simplified “roller in trough” design had a constant radius of curvature, and maximised the area of the articulating surfaces for polyethylene wear reduction. Removal of both cruciate ligaments was necessary, and the absence of a tibial intramedullary stem increased the risk of infection and rendered the joint less redeemable during revision surgeries. As did it predecessors, the implant also suffered from aseptic loosening which was a major disadvantage.

It is worth noting that considerable research was being carried out in other parts of the world, which also defined the evolution of knee replacements. At the Hospital for Special Surgery (HSS) located in New York, surgeons developed the Unicondylar and Duocondylar prostheses (Figure 3.9), which were similar in design to Gunston’s articulating surfaces substitution. The Duocondylar prosthesis retained the cruciate ligaments and bridged the condylar elements, bringing improved stability. Further evolution brought about the first total condylar prosthesis including a tibial stem (Figure 3.10). This design sacrificed both cruciate ligaments and created equal spaces in both flexion and extension. In addition, it included a patellofemoral flange, a polyethylene patellar button and anatomically shaped condyles.

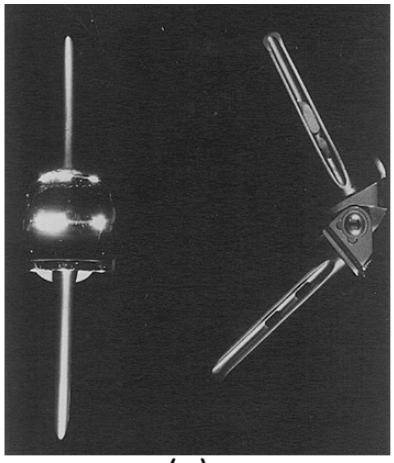

(a)

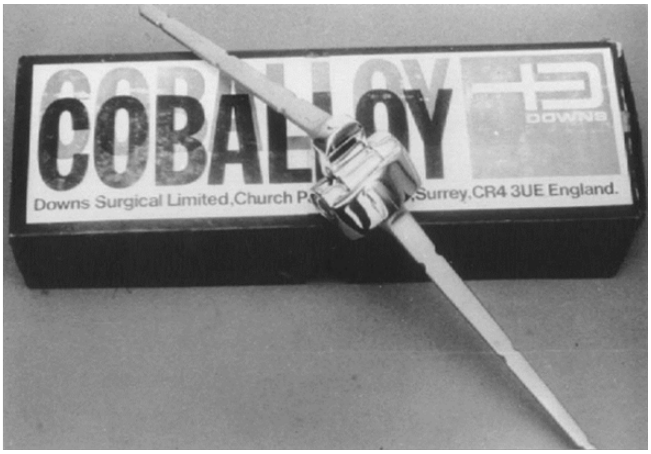

(b)

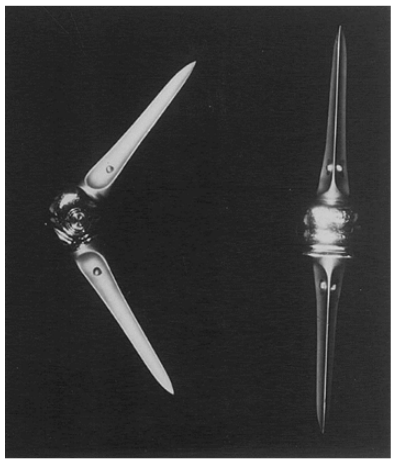

(c)

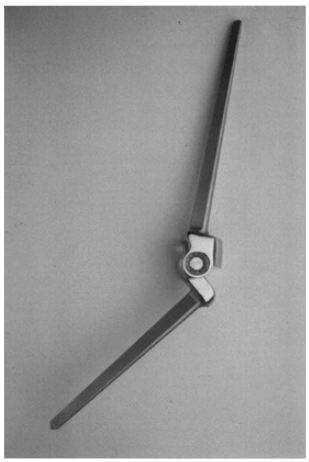

(d)

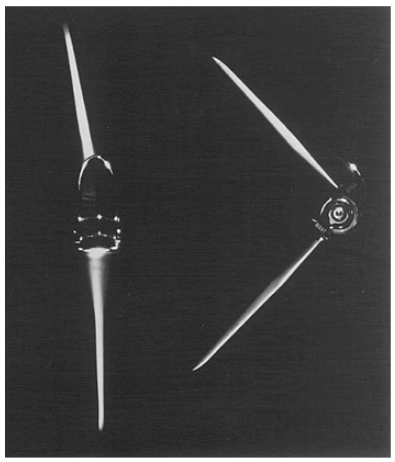

(e)

a. Walldius hinge
b. Shiers hinge
c. McKee hinges (screw fixed and tri-fin cemented)
d. GUEPAR hinge
e. Stanmore hinge

Figure 3.6 Total knee replacement designs [46]

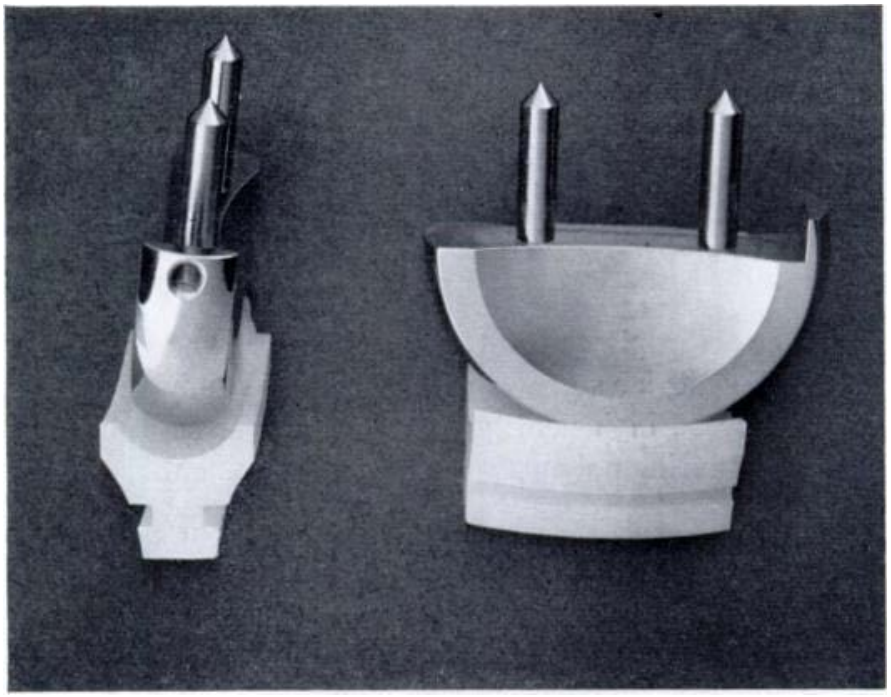

Figure 3.7 Gunston's polycentric knee prosthesis [44]

Figure 3.8 ICLH knee prosthesis [47]

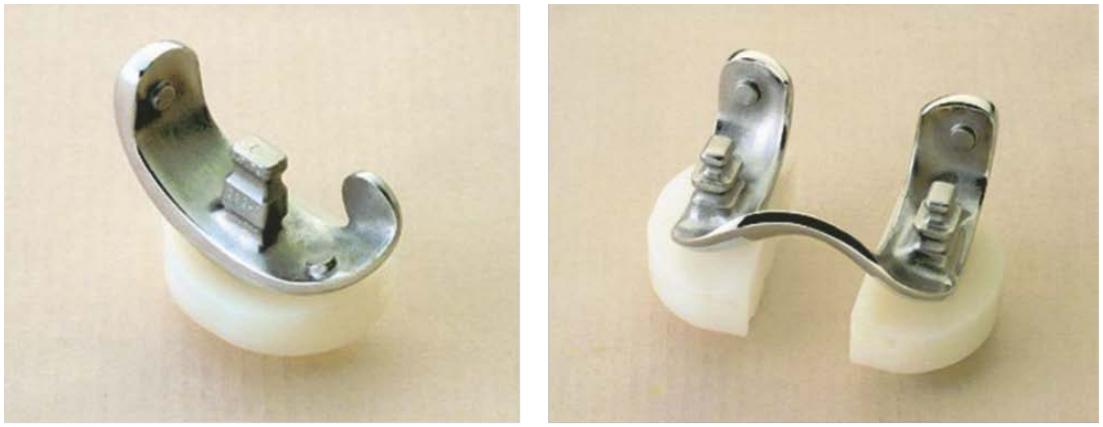

Figure 3.9 (a) Unicondylar and (b) Duocondylar prosthesis [48]

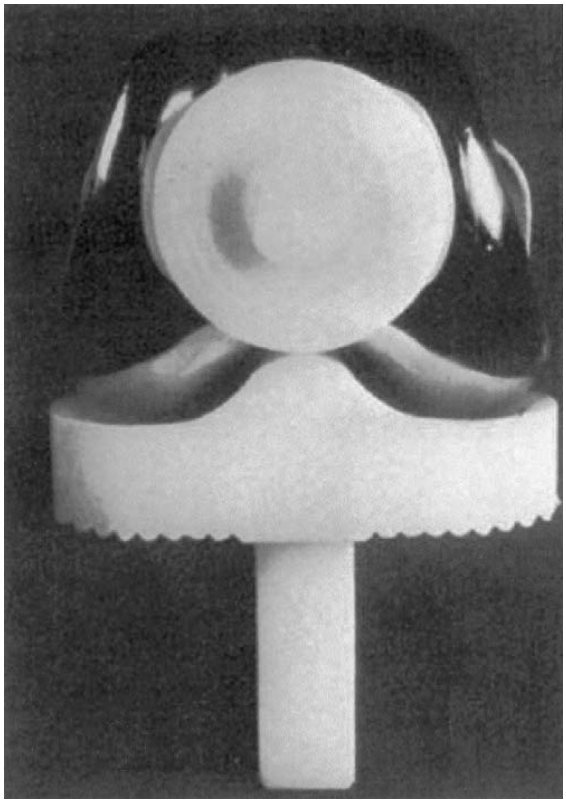

Figure 3.10 Insall's Total Condylar prosthesis [48]

3.5 Components of a TKR implant

Typically, TKR implants consist of four main components, which are

1. **Femoral component**: This metallic component curves around the distal end of the femur and replaces the femoral condyles. Grooves allow the patella glide smoothly against it as the knee flexes and extends.
2. **Patellar component**: This dome-shaped plastic component replicates the kneecap, and glides along the groove in the femoral component.
3. **Tibial insert**: This plastic component provides a cushion between the femoral component and the tibial tray. It is disc shaped
4. **Tibial tray**: This metallic component supports the tibial insert. It usually has a stem through which it is fixed in place by the cancellous bone in the tibia.

The plastic components are usually made from ultra-high molecular weight polyethylene (UHMWPE) which has a low coefficient of friction to enable fluid motion between the articulating surfaces. In addition, UHMWPE is resistant to abrasion, non-toxic and has low moisture absorption, making it suitable for implantable biomedical devices [4, 50].

The metallic parts of the TKR implant are mostly fabricated from cobalt chromium (CoCr) alloys, although titanium is sometimes used when lower strength is required. The percentage composition of CoCr alloy used for orthopaedic implants is defined by the industry standard ASTM F75 [51]: cobalt, chromium (27 – 30%) and molybdenum (5 – 7%). The limits of other consisting elements are also specified such as silicon and manganese (< 1%), iron (< 0.75%), nickel (< 0.5%), carbon (< 0.35%), nitrogen (< 0.25%), tungsten (< 0.2%), aluminium and titanium (< 0.1%), phosphorus (< 0.02%) and boron and sulphur (< 0.01%). These components are depicted in Figure 3.11.

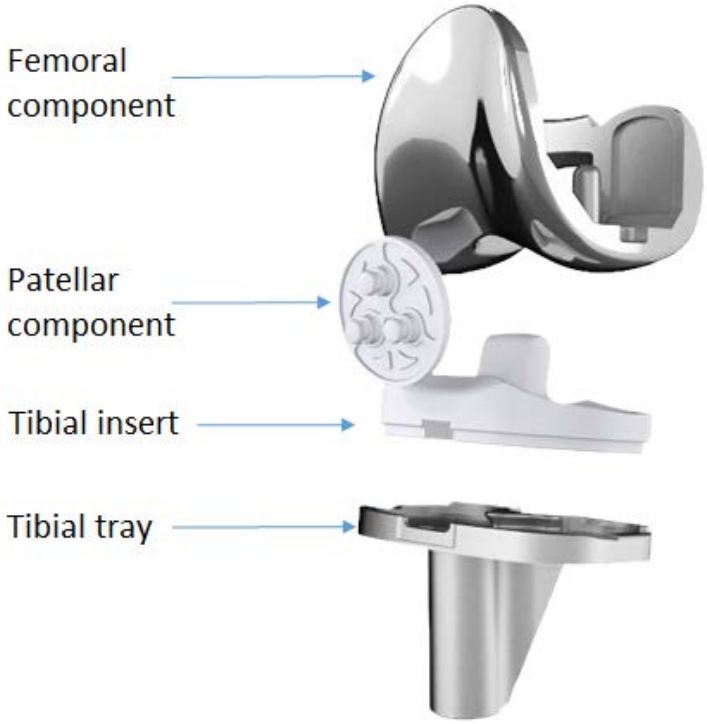

Figure 3.11 Typical TKR components [52]

3.6 TKR implant failure

In the United Kingdom alone, there were 5,856 cases of knee revisions in 2015, which accounts for over 6% of the TKR surgeries performed that year [26]. Some of the more prevalent failure modes have been widely reported for both early (< 2 years post-surgery) and late revisions and a comparison of their occurrence presented in Table 3.2 [53 – 58]. A discussion of the most common modes follows.

3.6.1 UHMWPE wear

This abrasive wear arises due to articulation of the UHMWPE insert with the harder surface of the femoral component. The van der Waals interactions of the molecular chains in UHMWPE are much weaker compared to those that exist within the metallic femoral component, hence some of the UHMWPE material is gradually removed during mutual movement as shown in Figure 3.12. The resulting particles further induce other wear processes like aseptic loosening and infection.

Table 3.2 Prevalent failure modes and their percentage occurrence in TKR revisions

	Overall input to TKR revisions (%)					
	Dalury et al (2013)	Sharkey et al (2002)	Fehring et al (2001)	Sharkey et al (2014)	Schroer et al (2013)	Suarez et al (2008)
PE wear	18.1	25	7	3.5	10	22
Osteolysis	4.5	N/A	N/A	N/A	N/A	N/A
Aseptic loosening	23.1	24.1	16	39.9	31.2	21
Instability	17.7	21	26	7.5	18.7	20
Infection	18	17.5	38	27.4	16.2	22
Arthrofibrosis	9.3	14.6	N/A	4.5	7	N/A
Malpositioning /Malalignment	2.9	11.8	N/A	~3	6.6	N/A
Fractures	1.4	2.8	N/A	4.7	3.2	N/A
Arthritis	1.7	0.9	N/A	N/A	N/A	N/A
Patellofemoral	N/A	6.6	8	~8	4.3	N/A
Other	2.9	N/A	5	N/A	2.7	14

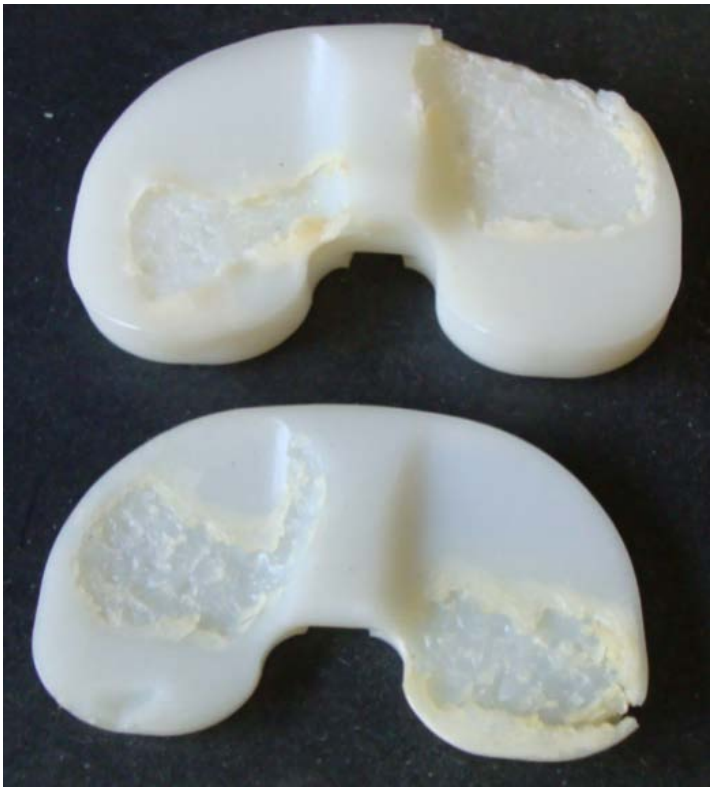

Figure 3.12 Representative image of retrieved tibial components showing extensive wear [59].

3.6.2 Osteolysis and Aseptic loosening

This occurs due to the breakdown of the bond between the implant and the underlying bone, in the absence of an infection. Worn-away particles of UHMWPE, metal and bone cement from the joint are dispensed into the body. This then induces a biological inflammatory response in which macrophages (a type of white blood cell) attempt to digest the debris through a process known as phagocytosis. Enzymes are secreted during this process which contribute to the periprosthetic osteolysis (bone resorption around the joint), leading to failure due to movement of the joint in the ensuing cavities. This is depicted in Figure 3.13 below.

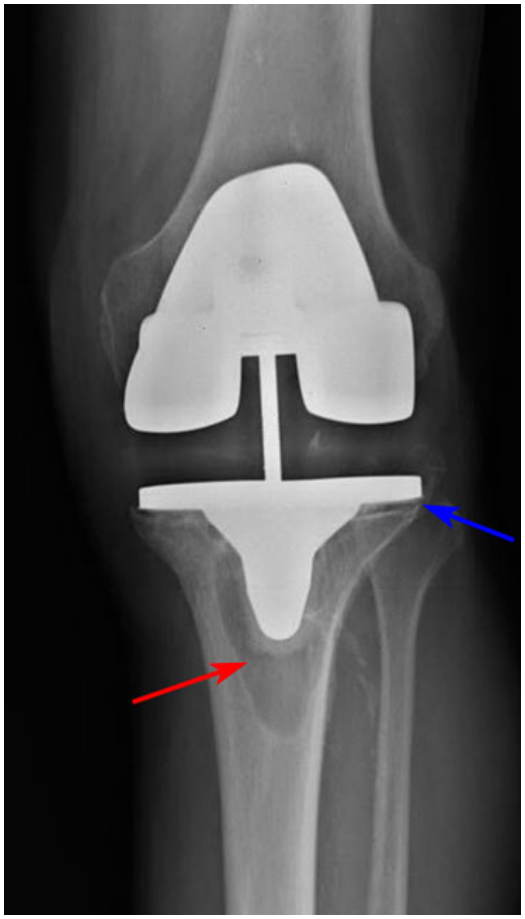

Figure 3.13 Osteolysis (red arrow) around the tibial component, causing it to loosen from the bone (blue arrow) [60].

3.6.3 Instability

Knee prosthesis instability (KPI) is the irregularly occurring disproportionate movement of the articular components leading to clinical failure of the implant [61]. It can be attributed to various factors including malalignment or malpositioning of the components, component loosening, implant breakage, inferior implant design, improper balancing of the flexion-extension space, patella fracture and ligament rupture [62, 63]. In addition, other patient-related factors such as obesity and hip or foot deformities can also bring about instability after TKR.

3.6.4 Infection

Infection is a complication that can occur during and/or after any surgical procedure. The large surface area of the TKR components provides a platform that bacteria may attach to, which then become unreachable by antibiotics. Although bacterial presence during surgery is inevitable, restricting the amount significantly reduces the probability of infection. The administration of oral and intravenous antibiotics also helps reduce post-operative infection. Antibiotics can also be added to bone cement for surgeries involving cemented fixation [64, 65].

The surgical process required for treatment depends on the degree of infection. In early post-operative infection instances, debridement with implant retention can be utilised [66]. For late chronic infection however, two separate revision surgeries are necessary. The first one is to remove the infected components and insert an antibiotic-impregnated cement spacer. Subsequently, a second surgery is performed to remove the spacer and insert a new implant [67 – 69].

3.6.5 Arthrofibrosis

Complexities in TKR surgeries can induce abnormal scarring, due to the formation of excessive fibrous tissue during the healing process. This dense tissue forms within the joint and its surrounding soft tissue spaces, causes the joint to contract and restricts the normal range of motion, as depicted in Figure 3.14. Diagnosis of this reaction is known as arthrofibrosis, or more simply, stiff knee syndrome [70, 71].

Early detection of acute cases is treatable by thorough physical therapy; however, revision surgery is required in more severe instances to dissect the tissue.

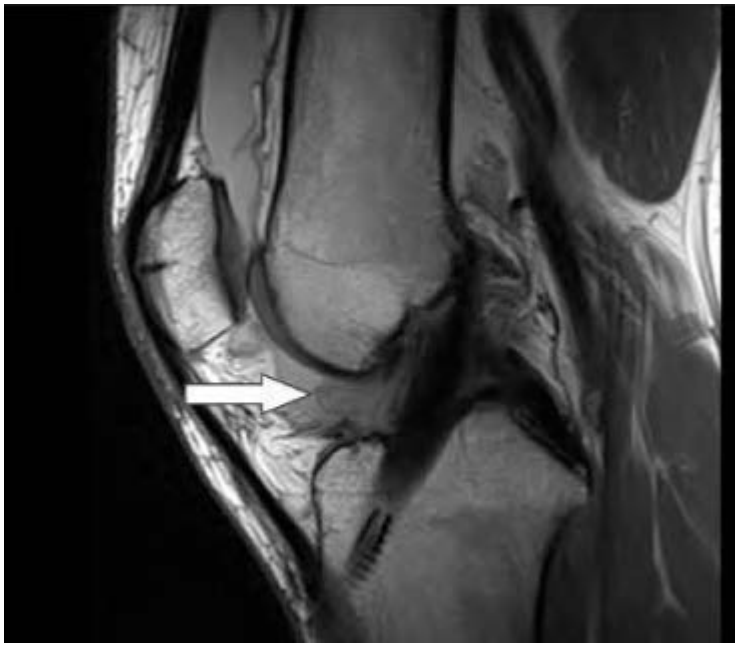

Figure 3.14 MRI image of the right knee showing localised anterior arthrofibrosis (Cyclops lesion) [72]

3.6.6 Malalignment

This is the deviation of the TKR from the neutral axis of the joint, leading to uneven weight bearing in the joint. A line passing through the centres of the femoral head and knee determines the mechanical axis of the femur, while that of the tibia is measured from the centres of the proximal tibial plateau and ankle in normal knees [73 - 75]. This axis is in 3^{o} valgus (outward angulation) from the vertical axis of the body as shown in Figure 3.15(a). A proximal to distal line in the intramedullary canal that bisects the femur defines its anatomical axis, whilst that of the tibia corresponds to its mechanical axis. The tibiofemoral angle subtended by the mechanical and anatomic axes of the femur (Figure 3.15(b)) is usually between 5-7^{o}, although this may vary depending on the hip angle as well as tibial or femoral deformities [73].

Deviation of components results in an alteration of the normal stress distribution, causing the load transferred to the bone to shift either medially or laterally. This in turn may lead to implant instability, loosening of the tibial component and accelerate polyethylene wear [76]. Various techniques exist to achieve neutral alignment, which

is usually between $0 \pm 3°$ relative to the mechanical axis. Computer-aided navigation systems that reduce these errors and help enhance post-operative alignment are in development.

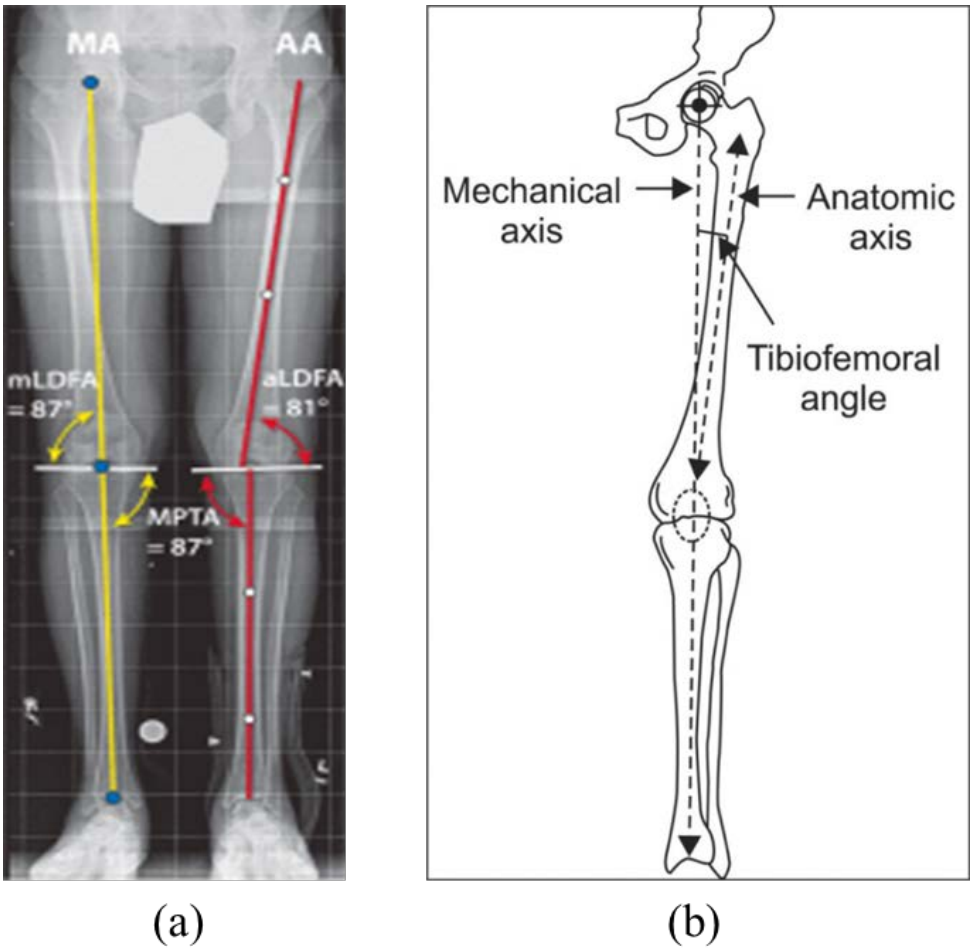

Figure 3.15 (a) Standing radiograph demonstrating the mechanical (MA) and anatomic (AA) axes of the femur and tibia and (b) schematic diagram showing the tibiofemoral angle [73, 77]

3.7 Conventional force measurement techniques in TKR implants

Previous efforts have been made to monitor the forces in knee implants, mostly using non-magnetic approaches. Whilst doing this, simultaneous research has also been carried out on monitoring knee kinematics and the remote powering of active components used in these systems. However, in keeping within the scope of this thesis, this review focuses mainly on the force measurement methods used.

3.7.1 Resistance strain gauges

A strain gauge is a device in which its electrical resistance varies proportionally to the amount of applied strain. This has been primarily utilised in majority of the research carried out on knee force measurements. Here, resistance strain gauges were positioned as sensors within the knee prosthesis in such a way that the strain on the material due to applied tibiofemoral forces caused a change in the electrical resistance of the gauges [78 – 82].

A variety of gauge arrangements have been used to achieve this. One method was to use Finite element analysis (FEA) to determine the strain distribution within the prosthesis, and this was implemented in the design and location of the strain gauges within the polyethylene insert as shown in Figure 3.16. Dry etching was used to fabricate the sensors in a polyamide-metal-polyamide sandwich, in order to maintain their biocompatibility characteristics. To determine the resistance variations, the strain gauges were connected in a Wheatstone bridge configuration with other resistors of known values. The output was amplified, digitised and then fed to an RF transponder for wireless transmission.

The designed insert was subjected to contact forces and all three rotational forces (flexion-extension, abduction-adduction and internal-external rotations) using a mechanical knee joint simulator. To validate the measurement system, a reference force transducer was integrated into the tibial tray and the measured data from both systems compared. A benefit of this measurement system is that the gauges can be configured to measure the total contact forces, as well as the forces on the medial and lateral sides of the insert separately.

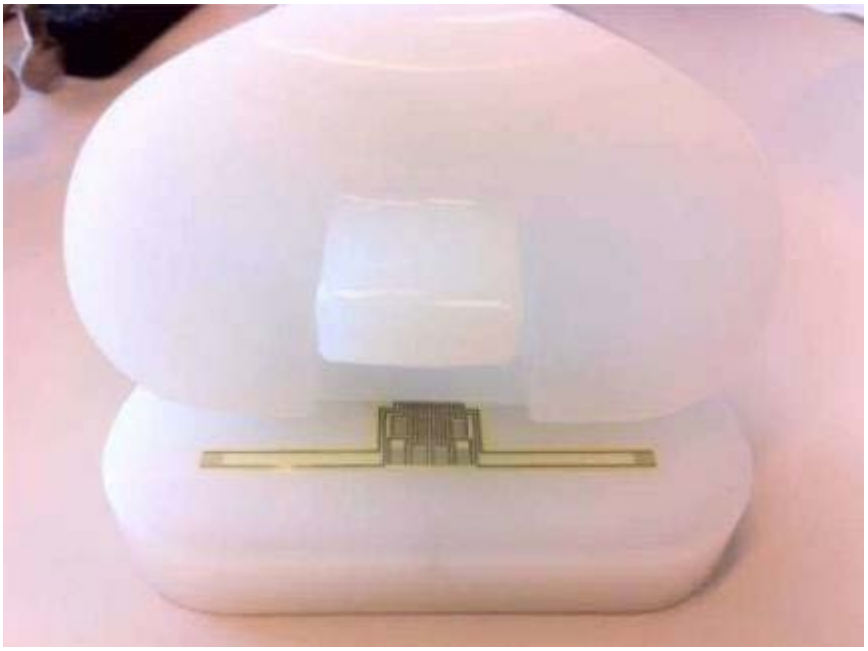

Figure 3.16 Positioning of strain gauges inside the PE insert [78]

Another method used was to locate two strain gauges in the medial and lateral sides of the insert, 15.5 mm away from the centre as shown in Figure 3.17. The gauges were fabricated using the polyimide-metal-polyimide sandwich structure, and were positioned above designed cavities to allow for deformation due to applied forces. Separate Wheatstone bridges were used for the strain gauges, as shown in Figure 3.18. The sensor and electronics were embedded between two 5 mm sections of polyethylene, which was sealed using an epoxy and cured for 16 hours at 45°.

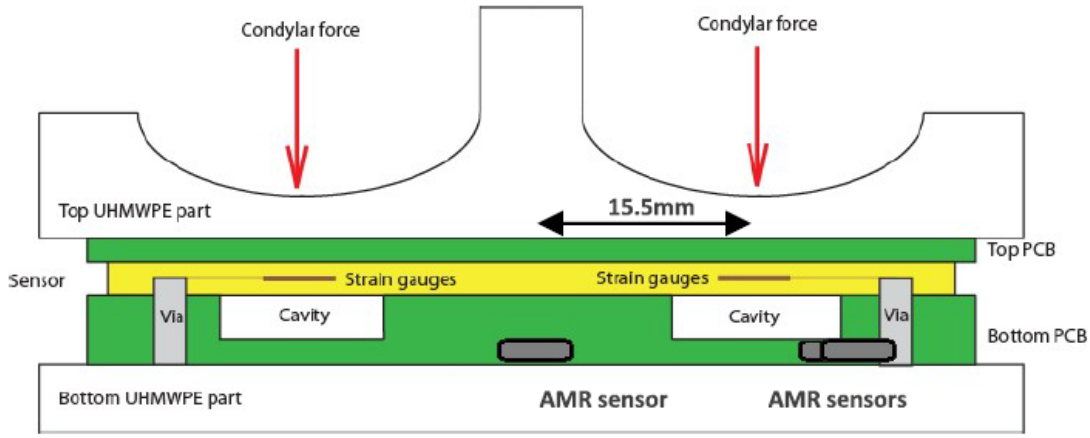

Figure 3.17 Configuration of strain gauges within PE insert [80]

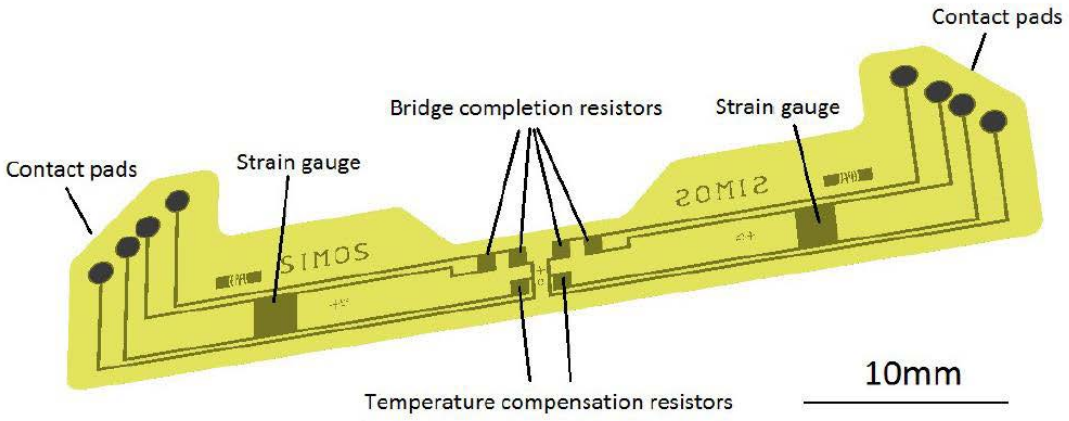

Figure 3.18 Microstructured polymer thin film strain sensor [80]

Loading was applied using a specially designed robotic knee simulator, using data collected from gait analysis by motion capture. To validate the system, a force sensor was integrated below the tibial plate of the knee simulator to provide a reference measurement.

A more advanced method has been developed to measure the forces and moments within the knee using an instrumented tibial tray. In this approach, the tibial plateau consisted of two plates with a small separation gap (about 0.635 mm) which were connected by a hollow, shrink-fit cylindrical stem. The proximal part of the assembly consisted of the unconstrained tibial tray which held the polyethylene insert, and the hollow stem which was fitted with a minimum of six strain gauges to measure the deformation when loaded. The distal part, which is intended to be cemented into the tibia and was kept fixed, consisted of a flat platform and a hollow shoulder which house the additional circuitry necessary for powering and wireless data transmission. A cross section of the instrumented tibial tray is as shown in Figure 3.19.

The tray was subjected to various loads and moments which simulate the forces in the knee, and a calibration matrix was determined which shows the correlation between the applied loads and the signal obtain from the strain gauges.

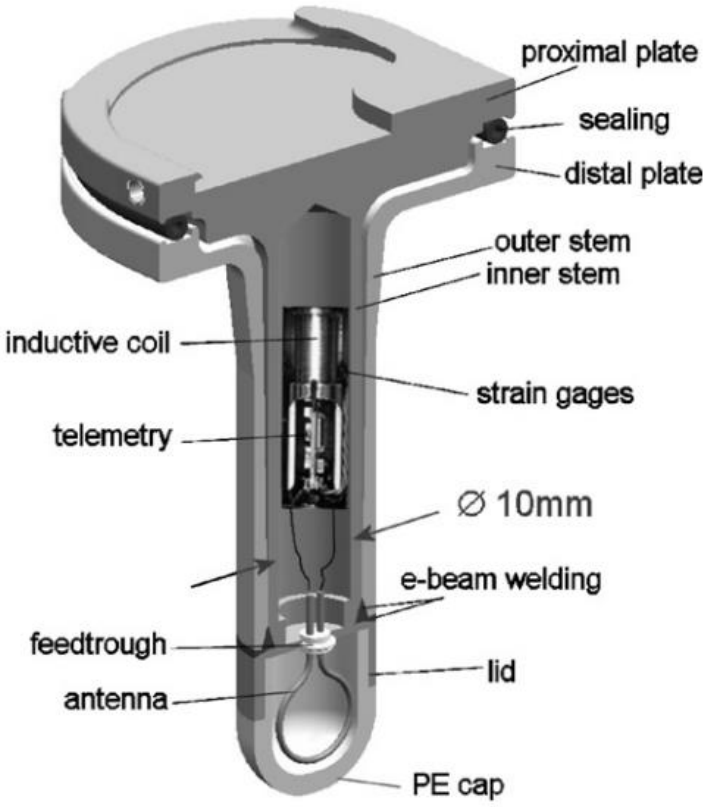

Figure 3.19 Cross section of the instrumented tibial tray for force and moment measurement [82]

3.7.2 Capacitive force sensors

Another approach to measuring the forces in knee replacement systems was to integrate piezoelectric ceramic sensors into the tibial tray whereby the dielectric thickness of the capacitors changed with applied force, thus varying the effective capacitance [83]. A diagram depicting this is shown in Figure 3.20. This variation in capacitance was measured using the RC time constant method which measures the discharge time of the charged capacitor to reach a set threshold (in this case, 25% of the supply voltage). To do this, a resistor with a known value *R* was connected to the electrical circuit and the voltage across the capacitor monitored using a comparator. Figure 3.21 shows a schematic diagram of the time constant measurement circuit. The discharge time was then calculated by

$$T_{discharge} = \tau \ln\left(\frac{V_{CC}}{0.25V_{CC}}\right) = 1.4\tau \tag{3.1}$$

where $\tau = RC$.

Real time low pass filtering was applied to the data obtained to eliminate some small noise present in the measured values.

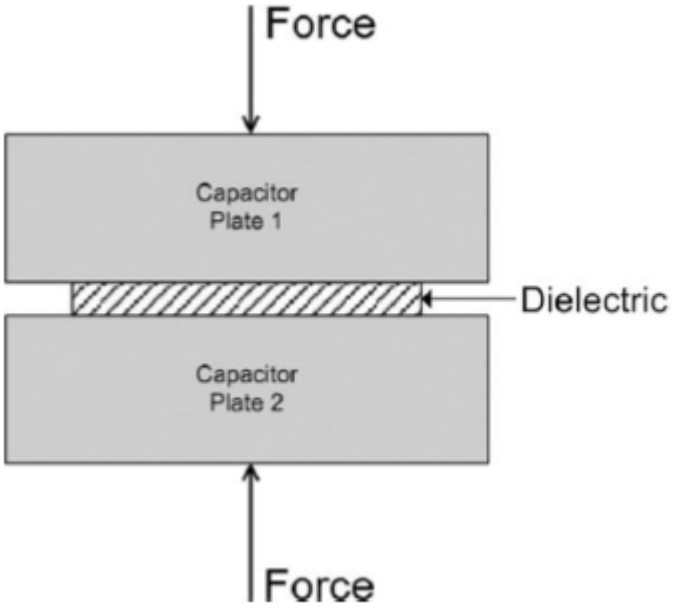

Figure 3.20 Diagram of concept for a capacitive sensor [83]

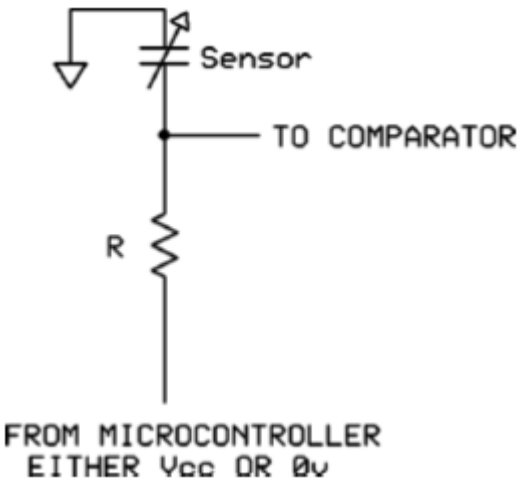

Figure 3.21 Schematic diagram of RC time constant measurement circuit [83]

A linear correlation between the discharge time and the capacitance was verified by carrying out tests using various precision capacitors. Observation of the RC voltage waveform showed that the charge time for the circuit was significantly greater than the calculated time response. This proved that the charge time was sufficient to ensure the sensor was fully charged before measurements were taken.

A linear relationship was established between the measured capacitance and applied force; however, there was a slight variation in the capacitance of each sensor for every level of applied force. After determining that this variation was not due to the load application device, each sensor was then calibrated using previously derived data from load cells and linear scale factors applied. As suggested by the author, the sensors utilised had poor repeatability.

3.7.3 Pressure-sensitive films

In this study, a mobile bearing knee prosthesis consisting of a cobalt chromium alloy femoral component and tibial tray, as well as a UHMWPE tibial insert were designed and prototyped [84]. Fuji Prescale (FP) pressure-sensitive films were used as the measurement transducer, whereby the film displays various densities of red depending on the value of pressure applied locally. Three types of FP films with different pressure ranges were used in this approach: Super Low Pressure (LLW) with a range of 0.5 – 2.5 MPa, Low Pressure (LW) with a range of 2.5 – 10 MPa, and Medium Pressure (MS) with a range of 10 – 50 MPa.

To calibrate the films, 40 x 50 mm strips of each film type were subjected to five different pressure values within the range of each film. Each applied load was measured with a load cell, and the ambient temperature controlled through a thermocouple. Digitised images of the films were obtained, and the mean values of the colour density in the imprinted regions were calculated and assigned to the applied pressure.

Two FP strips were located between each femoral condyle and the insert, and two more between the insert and the tibial tray. Various vertical loads were applied for 60 seconds and at different flexion angles; 2200 N at 15^{o}, 3200 N at 45^{o} and 2800 N at 60^{o}. A diagram of the experimental set up is shown in Figure 3.22.

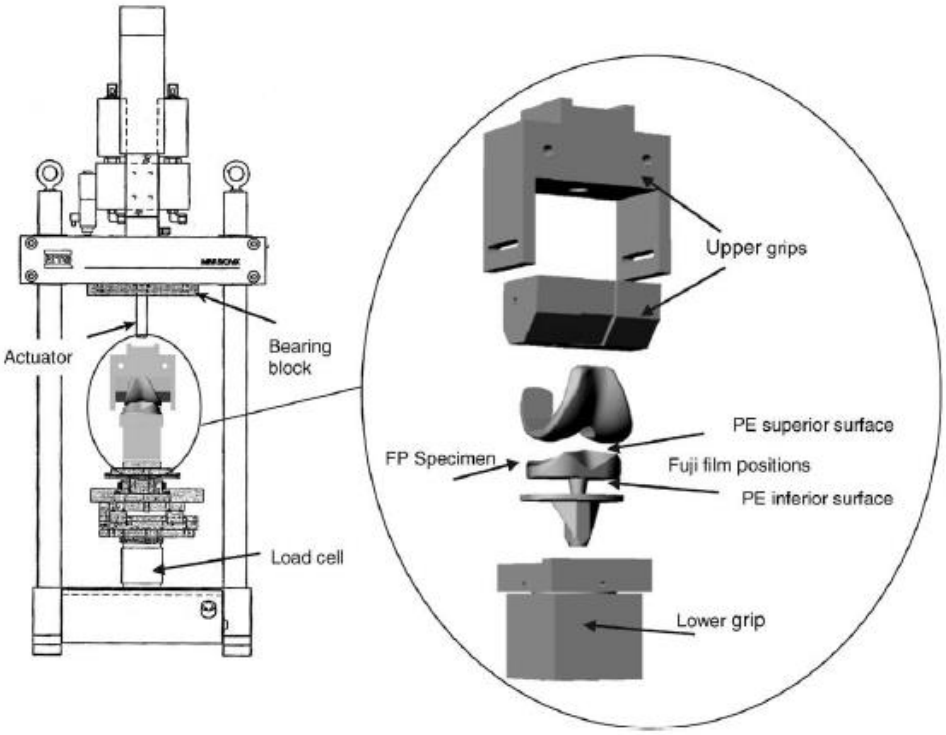

Figure 3.22 Experimental apparatus for contact pressure tests using pressure-sensitive films [84]

The results obtained showed good repeatability, with less than 3% standard deviation in the measurements taken for each flexion angle. In addition, similar values to the measured contact pressures were obtain through FEA modelling of the experimental set up. However, as the author pointed out, the films do not fully conform to the curvature of the insert due and the surface of the films suffer crimping. As a result, multiple smaller strips are required for better adherence but this may also lead to overestimation of the contact pressures due to boundary effects. Also, this method cannot be used for non-invasive monitoring as physical inspection of the colour intensity is necessary.

3.7.4 Magnetoresistive sensors

In this study, a force transducer consisting of three strategically-located magnetoresistors and permanent magnets was proposed [85]. The magnetoresistors were Sn-doped single crystal indium antimonite (InSb) films deposited on to alumina substrates. The magnets used were fabricated from samarium-cobalt alloy (Sm_2Co_{17}), 3 mm in length with a diameter of 4 mm. To direct the magnetic field along a

predetermined path, two Ni-Fe-Mo alloy strips with high relative magnetic permeability were positioned around the transducer – one above the magnet and one below, as shown in Figure 3.23.

An applied force on the femoral component generates a deformation in the tibial insert, which alters the distance between the magnet and the magnetoresistors. Consequently, the magnetic field that is coupled with the sensitive region of the magnetoresistor changes and this effectively results in a fluctuation in the sensor output resistance. A deformation-resistance curve was obtained experimentally by controlling the separation distance between the magnetoresistor and the magnet, whilst taking measurements for the resistance and magnetic field. This was used for sensor characterisation.

The insert was subjected to two dynamic loading conditions, the first being vertical compressive forces ranging from 0 - 3000 N to simulate substantial physical activity like jumping. For the second loading condition comprised a static component of 800 N alongside a sinusoidally-varying component with an amplitude of 200 N. The applied forces and distance variation were measured using a load cell and a linear variable differential transformer (LVDT) respectively, which were both integrated with the loading machine.

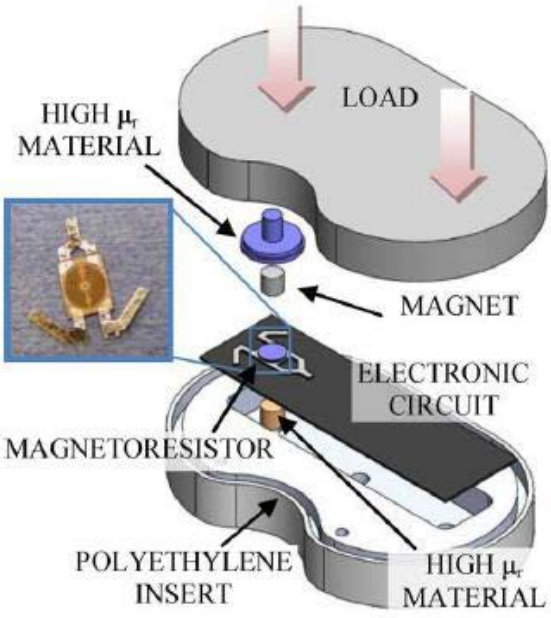

Figure 3.23 Diagram of the tibial insert with embedded magnetoresistive sensor [85]

The results obtained in both scenarios showed an inverse correlation between the applied force and the measured distance, whilst the measured resistance varied directly with the applied force.

3.7.5 Load cells

In this approach, load cells were positioned at the four quadrants (anteromedial, anterolateral, posteromedial and posterolateral) of the tibial tray as shown in Figure 3.24 [86, 87]. Although the dimensions of the tibial tray in the transverse plane were kept standard, the thickness was significantly higher than that found on the prosthesis used. This was done in order to make room for the load cells utilised. The tibial plateau comprised of upper and lower plates, held together by four 2.5 mm square posts which were 0.5 mm in height. Measurements of the force on each cell were taken, and the data obtained used to determine the total force acting on the insert as well as the position of the centre of pressure. These were calculated using the following equations.

$$x = \frac{22.86(F_3 + F_4 - F_1 - F_2)}{\sum_i^4 F_i} \tag{3.2}$$

$$y = \frac{10.34(F_2 + F_3 - F_1 - F_4)}{\sum_i^4 F_i} \tag{3.3}$$

$$F_{Total} = \sum_i^4 F_i \tag{3.4}$$

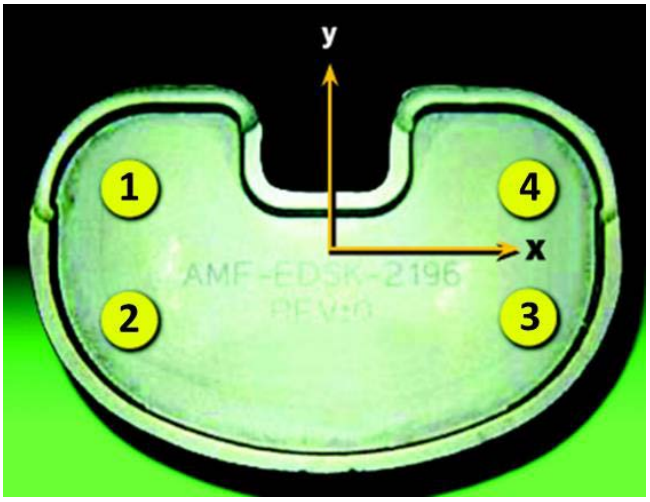

Figure 3.24 Schematic diagram of load cell positioning within the tibial tray [86, 87]

where x, y is the centre of pressure in the x and y directions in mm, and F_i is the force on the ith load cell.

Separate studies have been conducted using this transduction principle. In the initial research, in-vitro loading was performed using an actuator and the sensor output was obtained using strain gauges in full Wheatstone bridge configuration connected to the flexural members [86]. In-vivo measurements have also been taken intraoperatively for fixed flexion angles, and the data collected wirelessly through integrated electronic circuitry [87].

3.8 The need for magnetic measurement of knee forces

The various methods which have been used to measure knee forces and moments in total knee replacements have been outlined in the previous section. Whilst each method has inherent advantages, one common denominator of these methods is the necessity to embed additional electronic circuitry for non-invasive retrieval of measured data. In doing this, the original design of the prosthesis is often significantly modified and this may compromise its structural characteristics. This research aims to tackle this by proposing a new technique which eliminates this need. In the following chapters, the experimental work carried out using the proposed method is detailed, along with the relevant results achieved.

References

[1] Özkaya, N., Nordin, M., Goldsheyder, D. and Leger, D. (2012). *Fundamentals of biomechanics*. 3rd ed. New York [u.a.]: Springer, p.80.

[2] Singh, V. (2015). *General Anatomy*. 2nd ed. New Delhi: Elsevier, p.103.

[3] Schlossberg, L. and Zuidema, G. (1997). *The Johns Hopkins atlas of human functional anatomy*. 1st ed. Baltimore: Johns Hopkins University Press, p.16.

[4] Bartel, D., Davy, D. and Keaveny, T. (2006). *Orthopaedic biomechanics*. 1st ed. Upper Saddle River, N.J.: Pearson/Prentice Hall, pp.314 - 334.

[5] Fox, A., Bedi, A. and Rodeo, S. (2011). The Basic Science of Human Knee Menisci: Structure, Composition, and Function. *Sports Health: A Multidisciplinary Approach*, 4(4), pp.340-351.

[6] Alters, S. (2000). *Biology: Understanding life*. 1st ed. Boston: Jones and Barlette Publishers, p.345.

[7] Abernethy, B., Hanrahan, S., Kippers, V., Mackinnon, L. and Pandy, M. (2005). *The biophysical foundations of human movement*. 2nd ed. Champaign, IL: Human Kinetics, p.22.

[8] Khurana, J. (2009). *Bone pathology*. 2nd ed. Dordrecht: Humana Press, p.55.

[9] Chatra, P. (2012). Bursae around the knee joints. *Indian Journal of Radiology and Imaging*, 22(1), p.27.

[10] Chhabra, A. and Cerniglia, C. (2013). Bursae, Cysts and Cyst-like Lesions About the Knee. *Journal of the American Osteopathic College of Radiology*, 2(4).

[11] Majumdar, S. (2010). *Advances in MRI of the knee for osteoarthritis*. 1st ed. Singapore: World Scientific, p.24.

[12] Behnke, R. (2012). *Kinetic anatomy with web resource*. 3rd ed. Champiagn, IL.: Human Kinetics.

[13] Yen, Y. (2014). Assessment and Treatment of Knee Pain in the Child and Adolescent Athlete. *Pediatric Clinics of North America*, 61(6), pp.1155-1173.

[14] Komdeur, P., Pollo, F. and Jackson, R. (2002). Dynamic knee motion in anterior cruciate impairment: a report and case study. *Proceedings (Baylor University Medical Center)*, 15(3), pp.257 - 259.

[15] Hirschmann, M. and Müller, W. (2015). Complex function of the knee joint: the current understanding of the knee. *Knee Surgery, Sports Traumatology, Arthroscopy*, 23(10), pp.2780-2788.

[16] Wilkie, Y. and Kerr, C. (n.d.). *Human planes*. [image] Available at: http://kneestability.weebly.com/anatomy.html [Accessed 7 Nov. 2016].

[17] Kutzner, I., Heinlein, B., Graichen, F., Bender, A., Rohlmann, A., Halder, A., Beier, A. and Bergmann, G. (2010). Loading of the knee joint during activities of daily living measured in vivo in five subjects. *Journal of Biomechanics*, 43(11), pp.2164-2173.

[18] D'Lima, D., Patil, S., Steklov, N., Chien, S. and Colwell, C. (2007). In vivo knee moments and shear after total knee arthroplasty. *Journal of Biomechanics*, 40, pp. S11-S17.

[19] Nisell, R. and Ericson, M. (1992). Patellar forces during isokinetic knee extension. *Clinical Biomechanics*, 7(2), pp.104-108.

[20] Kuster, M., Wood, G., Stachowiak, G. and Gächter, A. (1997). Joint Load Considerations In Total Knee Replacement. *The Journal of Bone and Joint Surgery*, 79(1), pp.109-113.

[21] Costigan, P., Deluzio, K. and Wyss, U. (2002). Knee and hip kinetics during normal stair climbing. *Gait & Posture*, 16(1), pp.31-37.

[22] Christina, K. and Cavanagh, P. (2002). Ground reaction forces and frictional demands during stair descent: effects of age and illumination. *Gait & Posture*, 15(2), pp.153-158.

[23] British Standards Institute (2014). *BS ISO 14243-3: Implants for surgery – Wear of total knee joint prostheses*. London: British Standards Institute.

[24] Arthritis Foundation. (2016). *Osteoarthritis*. [online] Available at: http://www.arthritis.org/about-arthritis/types/osteoarthritis/ [Accessed 12 Dec. 2016].

[25] National Health Service, UK. *Arthritis - NHS Choices*. [online] Available at: http://www.nhs.uk/Conditions/Arthritis/Pages/Introduction.aspx [Accessed 12 Dec. 2016].

[26] National Joint Registry for England, Wales, Northern Ireland and the Isle of Man, (2016). *13th Annual Report*. [online] Available at: http://www.njrreports.org.uk [Accessed 12 Dec. 2016].

[27] Glyn-Jones, S., Palmer, A., Agricola, R., Price, A., Vincent, T., Weinans, H. and Carr, A. (2015). Osteoarthritis. *The Lancet*, 386(9991), pp.376-387.

[28] Sowers, M. and Karvonen-Gutierrez, C. (2010). The evolving role of obesity in knee osteoarthritis. *Current Opinion in Rheumatology*, 22(5), pp.533-537.

[29] Arthritis Action, UK. *Osteoarthritis*. [online] Available at: https://www.arthritisaction.org.uk/living-with-arthritis/what-is-arthritis/osteoarthritis/ [Accessed 12 Dec. 2016].

[30] National Institute of Arthritis and Musculoskeletal and Skin Diseases. *Handout on Health: Osteoarthritis*. [online] Available at: https://www.niams.nih.gov/health_info/Osteoarthritis/default.asp [Accessed 12 Dec. 2016].

[31] American academy of orthopaedic surgeons. *Osteoarthritis of the knee*. [Image] Available at: http://orthoinfo.aaos.org/topic.cfm?topic=a00212 [Accessed 16 Nov. 2016]

[32] Hosie, G. and Dickson, J. (2000). *Managing osteoarthritis in primary care*. 1st ed. Oxford: Blackwell Science.

[33] Wallace, G., Moulton, S., Higgins, M. and Kapsa, R. (2012). *Organic bionics*. 1st ed. Weinheim: Wiley-VCH, pp.23 - 24.

[34] Eynon-Lewis, N., Ferry, D. and Pearse, M. (1992). Themistocles Gluck: an unrecognised genius. *BMJ*, 305(6868), pp.1534-1536.

[35] Walldius, B. (1953). Arthroplasty of the knee joint employing an acrylic prosthesis. *Acta Orthopaedica Scandinavica*, 23(2), pp.121-131.

[36] Walldius, B. (1957). Arthroplasty of the knee using an endoprosthesis. *Acta Orthopaedica Scandinavica*, 28(sup 24), pp.1-112.

[37] Walldius, B. (1960). Arthroplasty of the knee using an endoprosthesis. *Acta Orthopaedica Scandinavica*, 30(1), pp.137-148.

[38] Walldius B. Arthroplasty of the knee using an endoprosthesis. SICOT 11th Congress, Mexico; pg 447.

[39] Shiers, L. (1954). Arthroplasty of the knee. Preliminary report of a new method. *The Bone and Joint journal*, 36-B (4), pp.553 - 560.

[40] Shiers, L. (1960). Arthroplasty of the knee. Interim report of a new method. *The Bone and Joint journal*, 42-B (1), pp.31 - 39.

[41] Blundell-Jones, C. (1972). Arthroplasty of the knee. *Modern trends in orthopaedics*, 8, p.210.

[42] Alnot, J., Aubriot, J., Deburge, A., Dubousset, J., Kenesi, C., Mazas, F., Patel, A. and Schramm, P. (1971). Arthoplastie totale du genou : le prosthese GUEPAR : description et technique de pose. *Revue de Chirurgie Orthopédique et Réparatrice de l'Appareil Moteur*, (57), pp.575 - 581.

[43] Lettin, A., Deliss, L., Blackburne, J. and Scales, J. (1978). The Stanmore hinge knee arthroplasty. *The Bone and Joint journal*, 60-B (3), pp.327 - 332.

[44] Gunston, F. (1971). Polycentric knee arthroplasty: prosthetic simulation of normal knee movement. *The Bone and Joint journal*, 53-B (2), pp.272 - 277.

[45] Freeman, M. and Swanson, S. (1972). Total prosthetic replacement of the knee. *The bone and Joint journal*, 54-B (1), pp.170-171.

[46] Shetty, A., Tindall, A., Ting, P. and Heatley, F. (2003). The evolution of total knee arthroplasty. Part II: the hinged knee replacement and the semi-constrained knee replacement. *Current Orthopaedics*, 17(5), pp.403-407.

[47] Bonnin, M., Amendola, N., Bellemans, J., MacDonald, S. and Menetrey, J. (2012). *The knee joint: Surgical techniques and strategies*. Paris: Springer, p.700

[48] Shetty, A., Tindall, A., Ting, P. and Heatley, F. (2003). The evolution of total knee arthroplasty. Part III:. *Current Orthopaedics*, 17(6), pp.478-481.

[49] TheOrthoSurgeon.com. *Total knee replacement components*. [image] Available at: http://theorthosurgeon.com/joomla/index.php/knee-replacement [Accessed 18 Nov. 2016].

[50] Tong, J., Ma, Y., Arnell, R. and Ren, L. (2006). Free abrasive wear behavior of UHMWPE composites filled with wollastonite fibers. *Composites Part A: Applied Science and Manufacturing*, 37(1), pp.38-45.

[51] ASTM Standard F75. (2012). Specification for Cobalt-28 Chromium-6 Molybdenum Alloy Castings and Casting Alloy for Surgical Implants (UNS R30075). *ASTM International*. [online] Available at: https://www.astm.org/cgi-bin/resolver.cgi?F75 [Accessed 10 Feb. 2016].

[52] Dartmouth-Hitchcock. *Total knee replacement components*. [image] Available at: http://www.dartmouth-hitchcock.org/ortho/knee_pain_treatments.html [Accessed 4 Jan. 2017].

[53] Dalury, D., Pomeroy, D., Gorab, R. and Adams, M. (2013). Why are Total Knee Arthroplasties Being Revised? *The Journal of Arthroplasty*, 28(8), pp.120-121.

[54] Sharkey, P., Hozack, W., Rothman, R., Shastri, S. and Jacoby, S. (2002). Why Are Total Knee Arthroplasties Failing Today? *Clinical Orthopaedics and Related Research*, 404, pp.7-13.

[55] Fehring, T., Odum, S., Griffin, W., Mason, J. and Nadaud, M. (2001). Early Failures in Total Knee Arthroplasty. *Clinical Orthopaedics and Related Research*, 392, pp.315-318.

[56] Sharkey, P., Lichstein, P., Shen, C., Tokarski, A. and Parvizi, J. (2014). Why Are Total Knee Arthroplasties Failing Today—Has Anything Changed After 10 Years? *The Journal of Arthroplasty*, 29(9), pp.1774-1778.

[57] Schroer, W., Berend, K., Lombardi, A., Barnes, C., Bolognesi, M., Berend, M., Ritter, M. and Nunley, R. (2013). Why Are Total Knees Failing Today?

Etiology of Total Knee Revision in 2010 and 2011. *The Journal of Arthroplasty*, 28(8), pp.116-119.

[58] Suarez, J., Griffin, W., Springer, B., Fehring, T., Mason, J. and Odum, S. (2008). Why Do Revision Knee Arthroplasties Fail? *The Journal of Arthroplasty*, 23(6), pp.99-103.

[59] Musib, M. (2012). Response to Ultra-High Molecular Weight Polyethylene Particles. *American Journal of Biomedical Engineering*, [online] 1(1), pp.7-12. Available at: http://article.sapub.org/10.5923.j.ajbe.20110101.02.html#Ref [Accessed 28 Nov. 2016].

[60] American academy of orthopaedic surgeons. *Osteolysis and implant loosening*. [image] Available at: http://orthoinfo.aaos.org/topic.cfm?topic=A00712 [Accessed 28 Nov. 2016].

[61] Rodriguez-Merchan, E. (2011). Instability Following Total Knee Arthroplasty. *HSS Journal*, 7(3), pp.273-278.

[62] Vince, K., Abdeen, A. and Sugimori, T. (2006). The Unstable Total Knee Arthroplasty. *The Journal of Arthroplasty*, 21(4), pp.44-49.

[63] Chang, M., Lim, H., Lee, N. and Moon, Y. (2014). Diagnosis, Causes and Treatments of Instability Following Total Knee Arthroplasty. *Knee Surgery & Related Research*, 26(2), pp.61-67.

[64] Masri, B., Duncan, C. and Beauchamp, C. (1998). Long-term elution of antibiotics from bone-cement. *The Journal of Arthroplasty*, 13(3), pp.331-338.

[65] Hsieh, P., Tai, C., Lee, P. and Chang, Y. (2009). Liquid Gentamicin and Vancomycin in Bone Cement. *The Journal of Arthroplasty*, 24(1), pp.125-130.

[66] Kalore, N. (2011). Diagnosis and Management of Infected Total Knee Arthroplasty §. *The Open Orthopaedics Journal*, 5(1), pp.86-91.

[67] Insall, J., Thompson, F. and Brause, B. (1983). Two-stage reimplantation for the salvage of infected total knee arthroplasty. *The Journal of Bone & Joint Surgery*, 65(8), pp.1087-1098.

[68] Nazarian, D., Jesus, D., McGuigan, F. and Booth, R. (2003). A two-stage approach to primary knee arthroplasty in the infected arthritic knee. *The Journal of Arthroplasty*, 18, pp.16-21.

[69] Pitto, R. and Spika, I. (2004). Antibiotic-loaded bone cement spacers in two-stage management of infected total knee arthroplasty. *International Orthopaedics*, 28(3), pp.129-133.

[70] Hegazy, A. and Elsoufy, M. (2011). Arthroscopic Arthrolysis for Arthrofibrosis of the Knee after Total Knee Replacement. *HSS Journal*, 7(2), pp.130-133.

[71] Jerosch, J. and Aldawoudy, A. (2006). Arthroscopic treatment of patients with moderate arthrofibrosis after total knee replacement. *Knee Surgery, Sports Traumatology, Arthroscopy*, 15(1), pp.71-77.

[72] Minné, C., Velleman, M. and Suleman, F. (2012). MRI findings of cyclops lesions of the knee. *SA orthopaedic journal*, [online] 11(2), pp.56 - 60. Available at: http://www.scielo.org.za/pdf/saoj/v11n2/11.pdf [Accessed 28 Nov. 2016].

[73] Cherian, J., Kapadia, B., Banerjee, S., Jauregui, J., Issa, K. and Mont, M. (2014). Mechanical, Anatomical, and Kinematic Axis in TKA: Concepts and Practical Applications. *Current Reviews in Musculoskeletal Medicine*, 7(2), pp.89-95.

[74] Donaldson, J., Joyner, J. and Tudor, F. (2015). Current Controversies of Alignment in Total Knee Replacements. *The Open Orthopaedics Journal*, 9(1), pp.489-494.

[75] Cooke, T., Sled, E. and Scudamore, R. (2007). Frontal plane knee alignment: A call for standardised measurement. *The Journal of Rheumatology*, 34(9), pp.1796 - 1801.

[76] Perillo-Marcone, A. and Taylor, M. (2006). Effect of Varus/Valgus Malalignment on Bone Strains in the Proximal Tibia after TKR: An Explicit Finite Element Study. *Journal of Biomechanical Engineering*, 129(1), p.1.

[77] Lee, D. and Byun, S. (2012). High Tibial Osteotomy. *Knee Surgery & Related Research*, [online] 24(2), pp.61-69. Available at: http://www.jksrr.org/journal/view.html?doi=10.5792/ksrr.2012.24.2.61 [Accessed 30 Nov. 2016]

[78] Arami, A., Simoncini, M., Atasoy, O., Ali, S., Hasenkamp, W., Bertsch, A., Meurville, E., Tanner, S., Renaud, P., Dehollain, C., Farine, P., Jolles, B., Aminian, K. and Ryser, P. (2013). Instrumented Knee Prosthesis for Force and Kinematics Measurements. *IEEE Transactions on Automation Science and Engineering*, 10(3), pp.615-624.

[79] Hasenkamp, W., Thevenaz, N., Villard, J., Bertsch, A., Arami, A., Aminian, K., Terrier, A. and Renaud, P. (2013). Design and test of a MEMS strain-sensing device for monitoring artificial knee implants. *Biomedical Microdevices*, 15(5), pp.831-839.

[80] Arami, A., Aminian, K., Forchelet, D. and Renaud, P. (2014). Implantable and wearable measurement system for smart knee prosthesis. *2014 IEEE Biomedical Circuits and Systems Conference (BioCAS) Proceedings*.

[81] Kirking, B., Krevolin, J., Townsend, C., Colwell, C. and D'Lima, D. (2006). A multiaxial force-sensing implantable tibial prosthesis. *Journal of Biomechanics*, 39(9), pp.1744-1751.

[82] Heinlein, B., Graichen, F., Bender, A., Rohlmann, A. and Bergmann, G. (2007). Design, calibration and pre-clinical testing of an instrumented tibial tray. *Journal of Biomechanics*, 40, pp. S4-S10.

[83] Holmberg, J., Alexander, L., Rajamani, R. and Bechtold, J. (2013). Battery-Less Wireless Instrumented Knee Implant. *Journal of Medical Devices*, 7(1), p.011006.

[84] Villa, T., Migliavacca, F., Gastaldi, D., Colombo, M. and Pietrabissa, R. (2004). Contact stresses and fatigue life in a knee prosthesis: comparison between in vitro measurements and computational simulations. *Journal of Biomechanics*, 37(1), pp.45-53.

[85] Crescini, D., Sardini, E. and Serpelloni, M. (2011). Design and test of an autonomous sensor for force measurements in human knee implants. *Sensors and Actuators A: Physical*, 166(1), pp.1-8.

[86] Kaufman, K., Kovacevic, N., Irby, S. and Colwell, C. (1996). Instrumented implant for measuring tibiofemoral forces. *Journal of Biomechanics*, 29(5), pp.667-671.

[87] Morris, B., D'Lima, D., Slamin, J., Kovacevic, N., Arms, S., Townsend, C. and Colwell, C. (2001). e-Knee: Evolution of the Electronic Knee Prosthesis. *The Journal of Bone and Joint Surgery-American Volume*, 83, pp.62-66.

4. Permeability changes in embedded amorphous ribbons

4.1 Synopsis

The wearing mechanism of the ultra-high molecular weight polyethylene (UHMWPE) bearing surfaces in orthopaedic surgical implants is presently difficult to track; hence, implant failure only becomes apparent when the patient experiences some discomfort. In exploring the integration of wireless stress sensors into UHMWPE, this chapter describes the first step in achieving the monitoring of knee implant stresses using magnetostrictive amorphous ribbons.

The objective of this set of experiments is to establish that changes in the permeability of the amorphous ribbons due to stress are still detectable after embedding in UHMWPE. This is particularly important due to the non-biocompatibility of the amorphous ribbons; hence, they are only usable within the body if completely encapsulated. The contents of this chapter have been peer reviewed and published in the IEEE Transactions on Magnetics [1].

4.2 Background theory

For a small pick-up coil in a uniform magnetic field, the voltage generated is as a result of electromagnetic induction. In this instance, the magnetic flux passing through the coil is the product of the area of the coil and the magnetic field component normal to the coil plane. Denoting the angle between the magnetic field vector and the normal to the coil by $\boldsymbol{\alpha}$, the flux through the pick-up coil is defined as [2, 3]

$$\Phi = AB\cos\alpha \tag{4.1}$$

As described in Chapter 2 (Equation 2.9), the emf induced in a solenoidal coil is proportional to the time rate of change of the magnetic flux density (dB/dt) and can be written as

$$v = -N\frac{d\Phi}{dt} = -NA\cos\alpha\frac{dB}{dt} \tag{4.2}$$

where *N* is the number of turns in the search coil. The source magnetic field generated by a sinusoidal current can be written as

$$B = B_0 \sin \omega t \tag{4.3}$$

Where ω is the angular frequency of the alternating current and B_0 is the amplitude of the magnetic field. Merging both equations, we obtain

$$v = -\omega NAB_0 \cos \alpha \cos \omega t \tag{4.4}$$

From the above equation, it is evident that the induced voltage is proportional to the frequency, amplitude of the magnetic field and the cosine of the angle between the field and the normal to the pick-up coil. This induced voltage is maximised when $\alpha = 0 \; or \; \pi$ (i.e. $\cos \alpha = \pm 1$). Comparing Equation 4.4 with the general form of a sinusoidal wave, the amplitude of the induced voltage becomes

$$v_{peak} = -\omega NAB_0 = -2\pi f NAB_0 \tag{4.5}$$

where *f* is the frequency in Hertz.

4.3 Experimental method

4.3.1 Test plate preparation

As-cast highly magnetostrictive Metglas 2605SC ($Fe_{81}Si_{13.5}B_{3.5}C_2$) amorphous ribbon produced by Allied Signal was selected for use due to its high stress sensitivity and magnetomechanical coupling factor. Some magnetic and mechanical properties of the material are tabulated in Table 4.1.

Table 4.1 Metglas 2605SC properties (as cast)

Maximum relative permeability	45000
Saturation magnetostriction (ppm)	27
Tensile strength (GPa)	1 – 2
Elastic modulus (GPa)	100 - 110
Curie temperature (^oC)	395

The ribbons were 25 μm thick, and cut down into strips measuring 5 mm by 25 mm using a scalpel. This was done to minimise the opposing demagnetising field generated within the ribbon sample by magnetic poles formed at it ends when subjected to an applied field. Assuming the ribbon sample used is uniform, homogenous and shaped like a rectangular prism, the origin of a Cartesian coordinate system can be located at its centre along with the associated dimensions as shown in Figure 4.1. If the applied field acts in the *z*-direction, the opposing field is proportional to the sample magnetisation by a demagnetisation factor D_z, which can be calculated theoretically by [4]

$$\begin{aligned}\pi D_z = {} & \frac{b^2-c^2}{2bc}\ln\left(\frac{\sqrt{a^2+b^2+c^2}-a}{\sqrt{a^2+b^2+c^2}+a}\right) \\ & + \frac{a^2-c^2}{2ac}\ln\left(\frac{\sqrt{a^2+b^2+c^2}-b}{\sqrt{a^2+b^2+c^2}+b}\right) + \frac{b}{2c}\ln\left(\frac{\sqrt{a^2+b^2}+a}{\sqrt{a^2+b^2}-a}\right) \\ & + \frac{a}{2c}\ln\left(\frac{\sqrt{a^2+b^2}+b}{\sqrt{a^2+b^2}-b}\right) + \frac{c}{2a}\ln\left(\frac{\sqrt{b^2+c^2}-b}{\sqrt{b^2+c^2}+b}\right) \\ & + \frac{c}{2b}\ln\left(\frac{\sqrt{a^2+c^2}-a}{\sqrt{a^2+c^2}+a}\right) + 2\tan^{-1}\left(\frac{ab}{c\sqrt{a^2+b^2+c^2}}\right) + \frac{a^3+b^3-2c^3}{3abc} \\ & + \frac{a^2+b^2-2c^2}{3abc}\sqrt{a^2+b^2+c^2} + \frac{c}{ab}\left(\sqrt{a^2+c^2}+\sqrt{b^2+c^2}\right) \\ & - \frac{(a^2+b^2)^{3/2}+(b^2+c^2)^{3/2}+(c^2+a^2)^{3/2}}{3abc}\end{aligned} \tag{4.6}$$

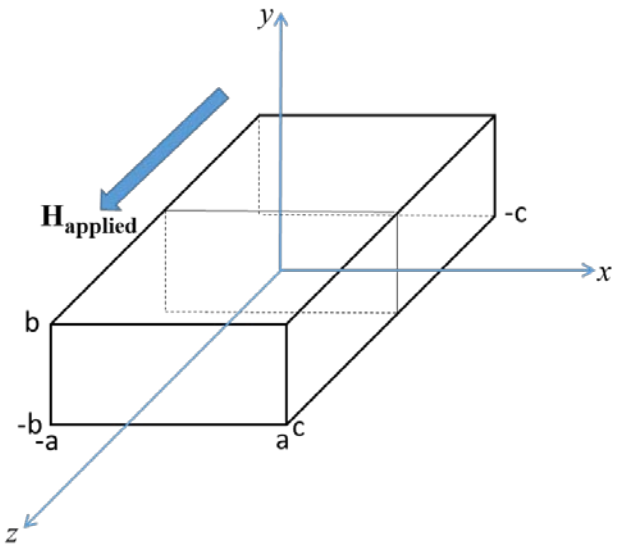

Figure 4.1 The coordinate system used in the demagnetising factor calculations, with the origin located at the prism centre

Where *a* is half of the sample width, *b* is half of the sample thickness and *c* is half of the sample length. This resulted in a demagnetisation factor of approximately 0.002.

Test plates in the form of 10 mm thick discs were produced by compression moulding using three manufacturing approaches for the integration of the amorphous ribbons. This moulding process was done by depositing a pre-determined amount of UHMWPE powder (charge) into the bottom half of the metal, and then applying a constant pressure with the top half to ensure the powder makes contact with all surfaces of the mould whilst maintaining a steady temperature of 140^{o}C for 30 minutes to allow for proper curing [5]. The justification for selecting this curing temperature is the melting point of UHMWPE, which is between 130 – 140 ^{o}C [6 - 8]. The mould was then allowed to cool gradually to room temperature, thus allowing for complete plasticisation. A schematic diagram representing this is Figure 4.2.

The first manufacturing approach consisted of depositing the amorphous ribbon on top of a layer of virgin UHMWPE powder, which was then covered with another layer of powder and moulded (Sample A). It was assumed that this would ensure the best possible adhesion between the UHMWPE and the amorphous ribbon, consequently improving stress transfer. However, this approach also makes it difficult to repeatedly position the ribbon accurately within the plates. The second approach involved sandwiching the amorphous ribbon between two pre-moulded UHMWPE plates, thus facilitating a more accurate positioning before moulding (Sample B). However, this approach raised concerns regarding the adhesion between the UHMWPE and the ribbon, as well as between the two pre-solidified UHMWPE plates. Finally, a third approach was considered as a compromise between the previous two, in which the amorphous ribbon was deposited on top of a pre-moulded PE plate and then covered with a layer of virgin powder, before the embedding moulding process (Sample C). A diagram of the resultant embedded plates is depicted in Figure 4.3.

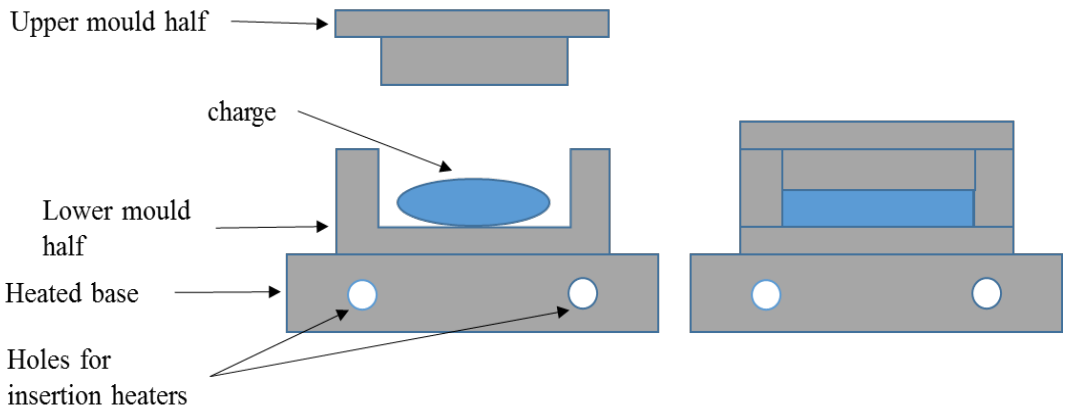

Figure 4.2 Compression moulding process for test plate fabrication

4.3.2 Measurement technique

The discs produced were subjected to longitudinal tensile stresses in the presence of an applied AC magnetic field of magnitude 50 A/m generated using a 364-turn, 0.58 m long solenoid fed by a power amplifier. Direct loading of the discs with fixed masses using a pulley system introduced the stresses, and the resulting voltage changes measured using identical compensated search coils of 100 turns each, with a 2 cm radius and 1 cm length. The field coil was wound around the centre of the disc in the direction of the ribbon length, and the compensating coil located beside it within the same field intensity. The coils were coupled differentially, such that the direction of current in each coil opposes the other as shown in Figure 4.4. This forms a gradiometer coil sensor, subtracting the effect of the applied field and only measuring the voltage induced by the flux changes in the amorphous ribbons. A simplified block diagram of the measurement system is shown in Figure 4.5, with device under test (DUT) signifying the prepared samples.

The transducers were sinusoidally magnetised at frequencies of 100 Hz, 500 Hz and 1 kHz respectively, and the search coil voltages measured using an *Agilent* 34401A digital multimeter. For each measurement, the output was sampled 100 times and the mean value recorded.

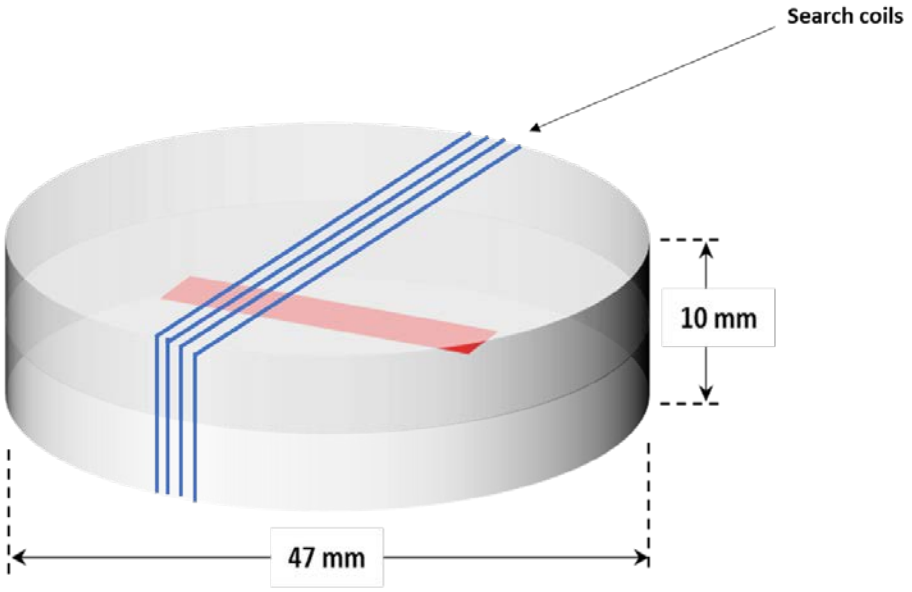

Figure 4.3 Diagram of embedded test plates showing dimensions and position of amorphous ribbons (including search coil orientation)

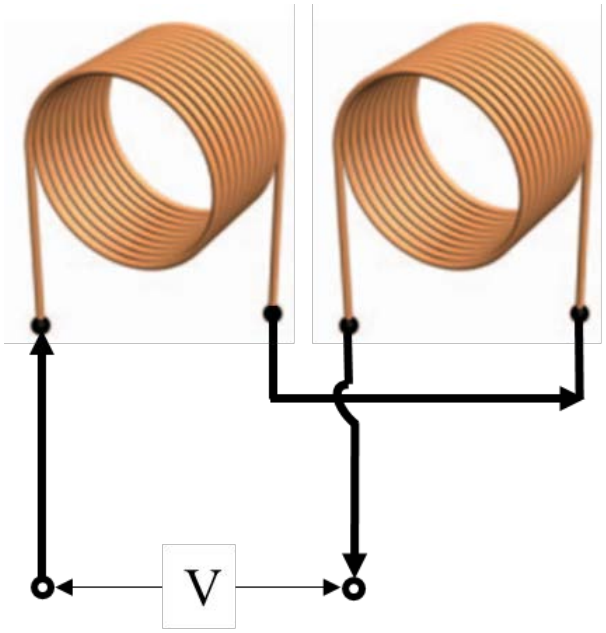

Figure 4.4 Topology of compensated search coils with the direction of current indicated

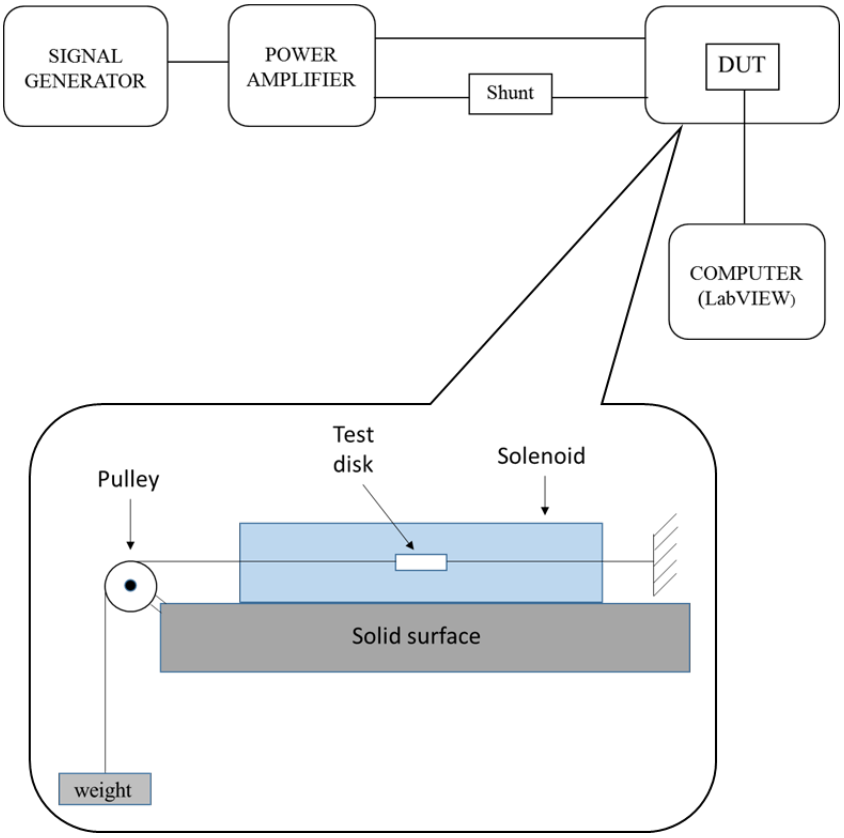

Figure 4.5 Block diagram of the measurement system

4.4 Results and explanation

The first set of measurements was to establish that the magnetic characteristics of the amorphous ribbon (not shown here) could be measured after the embedding process. This was done by estimating the frequency dependent sensitivity of the samples whilst keeping the peak amplitude of the magnetic flux constant. Figure 4.6 shows the full load output voltages obtained for the disc-disc sample (Sample B) expressed as a normalised percentage for better comparison. It was observed that the sensitivity increased with frequency, as indicated by a greater drop in the output voltages (denoted by an increased slope). Figure 4.7 shows a comparison of the samples' sensitivities normalised as a percentage of the full load output voltage, at a frequency of 1 kHz. As can be seen from the plots, sample A showed the greatest sensitivity to the applied stress. This can be attributed to the better adhesion between the amorphous ribbon and the UHMWPE when embedding is performed using virgin powder only; hence, more stress would appear to be transferred to the ribbon.

Sample A (being the most favourable) was further subjected to various tensile loading conditions using the same pulley system but in steps of 25 N and at a uniform applied magnetic field of 1.1kA/m. The normalised output measured is as shown in Figure 4.8.

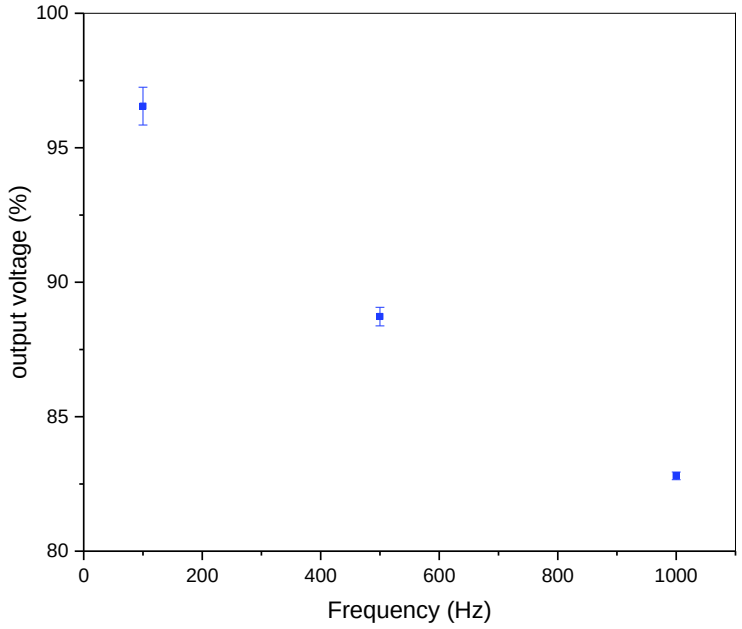

Figure 4.6 Frequency dependent sensitivity of sample B (constant peak magnetic flux density)

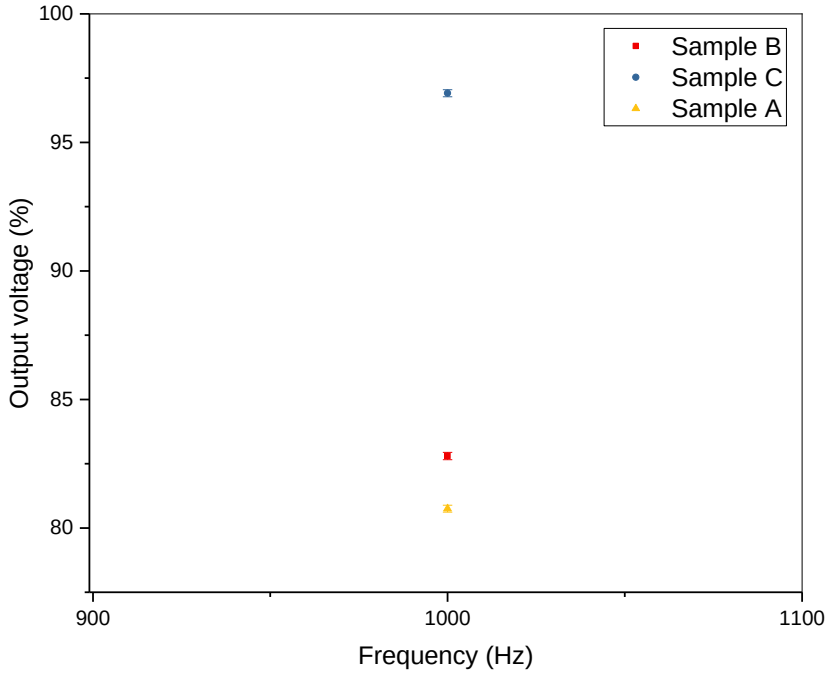

Figure 4.7 Sensitivity of all three samples (uniform magnetic flux density)

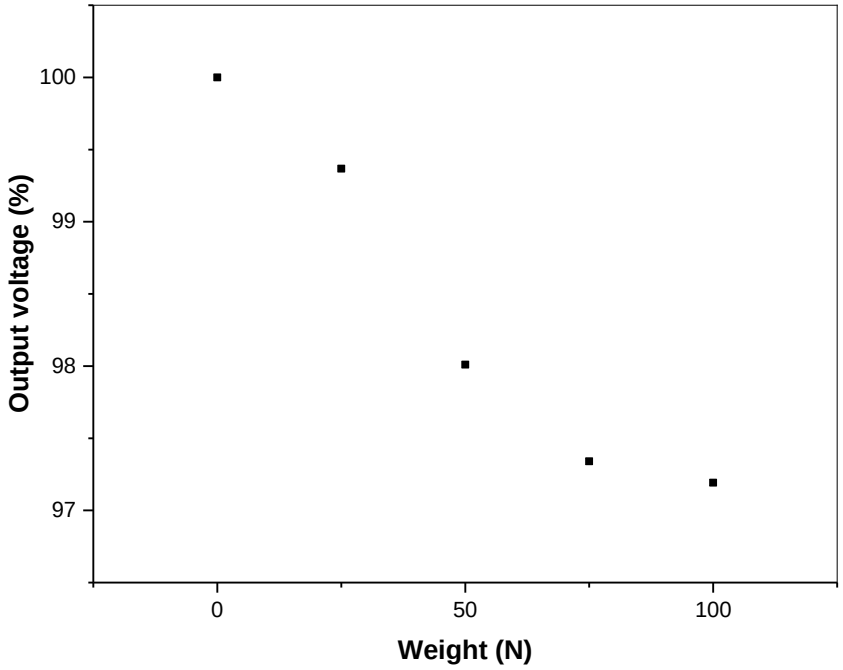

Figure 4.8 Normalised output voltage of sample A for different loading conditions at 1 kHz

The application of higher tensile stresses produced greater strain on the sample and consequently a steady drop in the output voltage, thereby confirming the established relationship between the two quantities. This is due to the change in shape of the magnetic hysteresis curve of the ferromagnetic material due to the applied tensile stress.

This relationship can be further improved by annealing the amorphous ribbon, thereby eliminating internal casting stresses which may oppose those applied. It should also be noted that the direction of the applied magnetic field was parallel to that of the stress; however, the magnetostrictive effect is maximum when the domains are oriented perpendicular to the easy axis. In this case, the application of a magnetic field parallel to the easy axis produces 90^{o} domain rotations, thereby maximising the magnetostrictive effect.

4.5 Summary

The objective of the work contained in this chapter was to verify that the magnetic properties of the amorphous ribbon could still be measured after being encapsulated in UHMWPE. The results obtained confirm this, and show a correlation between the applied strain in the ribbon and the output voltage measured across adjacent search coils. This is a direct consequence of the changes in the magnetic permeability of the ribbon, as described by the Villari effect.

References

[1] Okhiria D., Giebaly D., Meydan T., Bigot S. and Theobald P. (2015). In Vivo monitoring of orthopaedic implant wear using amorphous ribbons. *IEEE Transactions on Magnetics*, 51(1), pp 1-3.

[2] O'Handley, R. (2000). *Modern magnetic materials*. New York: Wiley.

[3] Jiles, D. (1998). *Introduction to magnetism and magnetic materials*. London:Chapman and Hall.

[4] Aharoni, A. (1998). Demagnetizing factors for rectangular ferromagnetic prisms. *Journal of Applied Physics*, 83(6), pp.3432-3434.

[5] Vasile, C. and Pascu, M. (2005). *Practical guide to polyethylene*. 1st ed. Shrewsbury: RAPRA Technology, p.128.

[6] Sterling Plastics Inc. - Blaine MN plastics distributor. *UHMW (ULTRA-HIGH MOLECULAR WEIGHT POLYETHYLENE)*. [online] Available at: http://sterlingplasticsinc.com/materials/uhmw-ultra-high-molecular-weight-polyethylene/ [Accessed 8 January 2014].

[7] Techmould. *Machining UHMWPE - Techmould*. [online] Available at: http://techmould.co.uk/machining-uhmwpe/ [Accessed 8 May 2017].

[8] Ducheyne, P., Healy, K., Grainger, D., Hutmacher, D. and Kirkpatrick, C. (2011). *Comprehensive biomaterials*. 1st ed. Amsterdam: Elsevier, p.40.

Non-invasive measurement of knee implant forces

5.1 Synopsis

As demonstrated in the previous chapter, the variation in flux density can be observed using an induction coil placed near or around the magnetic material. Assuming a uniform flux density distribution in the region enclosed by the coils, and from the inductance approximation, it follows that the inductance of the coil varies proportionally with the change in permeability. The presence of the ferromagnetic material increases the flux density for a specified current value, and this alters the inductance of the coil. These variations in inductance can be measured using a parallel tuned circuit with known capacitance, where the magnitude of the resultant impedance is maximal at the resonant frequency. The contents of this chapter have been peer reviewed and published in the IEEE Transactions on Magnetics [1].

5.2 Background theory

5.2.1 Magnetic field in Helmholtz coils

The magnetic field generated by an electric current passing through a wire is described by the Biot-Savart law as

$$\vec{\boldsymbol{B}} = \frac{\mu_0}{4\pi} \oint \frac{I d\boldsymbol{l} \times \hat{\boldsymbol{r}}}{r^2} \tag{5.1}$$

Consider the field generated by a single current loop at a point P located on its axis, as depicted in Figure 5.1. The differential current element situated at $\vec{\boldsymbol{r}}'$ can be expressed as

$$\begin{aligned} I\overrightarrow{d\boldsymbol{l}} = I\left(\overrightarrow{d\boldsymbol{r}'}/d\phi\right)d\phi &= I\left[\frac{d(R(\cos\phi\,\hat{\boldsymbol{\imath}} + \sin\phi\,\hat{\boldsymbol{\jmath}}))}{d\phi}\right]d\phi \\ &= IRd\phi(-\sin\phi\,\hat{\boldsymbol{\imath}} + \cos\phi\,\hat{\boldsymbol{\jmath}}) \end{aligned} \tag{5.2}$$

The position vector of the point P located at a distance *z* from the centre of the loop is denoted by $\vec{\boldsymbol{r}}_p = z\hat{\boldsymbol{k}}$. Therefore, the relative position vector is expressed as

$$\vec{\boldsymbol{r}} = \vec{\boldsymbol{r}}_p - \vec{\boldsymbol{r}}' = -R\cos\phi\,\hat{\boldsymbol{\imath}} - R\sin\phi\,\hat{\boldsymbol{\jmath}} + z\hat{\boldsymbol{k}} \tag{5.3}$$

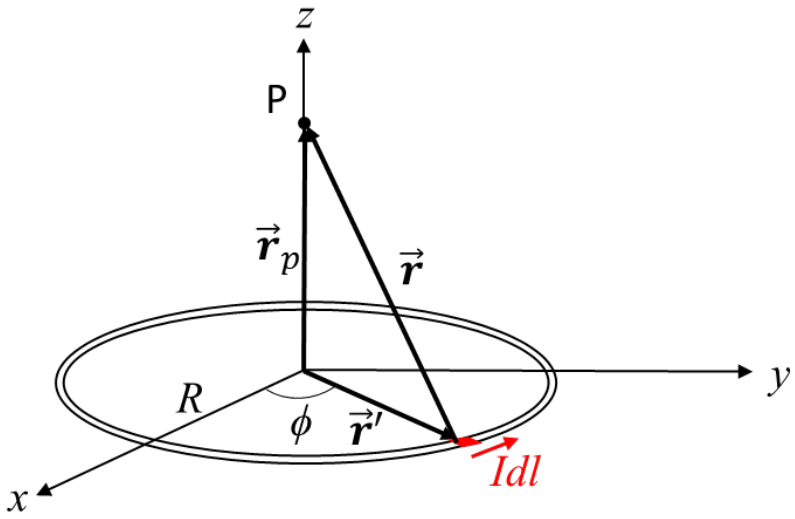

Figure 5.1 Magnetic field in a current-carrying circular loop

Thus,

$$r = |\vec{\boldsymbol{r}}| = \sqrt{(-R\cos\phi)^2 + (-R\sin\phi)^2 + z^2} = \sqrt{R^2 + z^2} \tag{5.4}$$

Therefore, the unit vector from *Id**l*** to point P can be written as

$$\hat{\boldsymbol{r}} = \frac{\vec{\boldsymbol{r}}}{r} = \frac{-R\cos\phi\,\hat{\boldsymbol{\imath}} - R\sin\phi\,\hat{\boldsymbol{\jmath}} + z\hat{\boldsymbol{k}}}{r} \tag{5.5}$$

Computing the cross product, $d\boldsymbol{l} \times \hat{\boldsymbol{r}}$ is simplified as

$$\begin{aligned} d\boldsymbol{l} \times \hat{\boldsymbol{r}} &= \frac{1}{r}\left[Rd\phi(-\sin\phi\,\hat{\boldsymbol{\imath}} + \cos\phi\,\hat{\boldsymbol{\jmath}})\right. \\ &\qquad \left. \times \left(-R\cos\phi\,\hat{\boldsymbol{\imath}} - R\sin\phi\,\hat{\boldsymbol{\jmath}} + z\hat{\boldsymbol{k}}\right)\right] \\ &= \frac{Rd\phi}{r}\left(z\cos\phi\,\hat{\boldsymbol{\imath}} + z\sin\phi\,\hat{\boldsymbol{\jmath}} + R\hat{\boldsymbol{k}}\right) \end{aligned} \tag{5.6}$$

Applying the Biot-Savart law around the loop, the field at point P is

$$\vec{\boldsymbol{B}} = \frac{\mu_0 IR}{4\pi}\int_0^{2\pi} \frac{z\cos\phi\,\hat{\boldsymbol{\imath}} + z\sin\phi\,\hat{\boldsymbol{\jmath}} + R\hat{\boldsymbol{k}}}{\left(\sqrt{R^2 + z^2}\right)^3} d\phi \tag{5.7}$$

The *x* and *y* components vanish since the integral of the functions over the limits is equal to zero. This leaves on a *z*-component denoted by

$$B_z = \frac{\mu_0 I R^2}{4\pi} \int_0^{2\pi} \frac{d\phi}{\left(\sqrt{R^2 + z^2}\right)^3} = \frac{\mu_0 I R^2}{2\left(\sqrt{R^2 + z^2}\right)^3} \tag{5.8}$$

In the case of a coil with a finite number of turns *N*, the field is

$$B_z = \frac{\mu_0 N I R^2}{2\left(\sqrt{R^2 + z^2}\right)^3} \tag{5.9}$$

For a system consisting of two coils serially connected, the field generated at a point located between them becomes

$$B_z = \frac{\mu_0 N I R^2}{2}\left(\frac{1}{\left(\sqrt{R^2 + z^2}\right)^3} + \frac{1}{\left(\sqrt{R^2 + (d - z)^2}\right)^3}\right) \tag{5.10}$$

where *d* is the separation between the two coils.

A Helmholtz coil configuration is composed of two identical magnetic coils positioned symmetrically along a mutual axis, and the separation between them equivalent to the radius of one coil. The magnetic field generated in the domain between the coils is near-uniform.

For a Helmholtz coil geometry, $d = R$. Thus, the field induced at a point midway between the coils (i.e. $z = {}^{R}/_{2}$) is given by

$$B_z = \frac{\mu_0 N I R^2}{2}\left(\frac{1}{\left(\sqrt{R^2 + \left(\frac{R}{2}\right)^2}\right)^3} + \frac{1}{\left(\sqrt{R^2 + \left(R - \left(\frac{R}{2}\right)\right)^2}\right)^3}\right)$$

$$= \left(\frac{2}{\sqrt{5}}\right)^3 \frac{\mu_0 N I}{R} \tag{5.11}$$

5.2.2 LC circuit resonance

Consider an ideal LC (tuned) circuit which consists of an inductor and a capacitor connected in parallel, as shown in Figure 5.2. If the capacitor is in a fully charged state, current will flow through the inductor and induce a magnetic field around it, thereby reducing the capacitor voltage until it is completely discharged. Due to the fact that inductors oppose current changes, the current flow continues and the capacitor begins to recharge with a voltage opposite in polarity to the initial charge. This goes on until the current flow is depleted and the capacitor is once again at full charge. The cycle repeats itself, with the inductor current flowing in the opposite direction.

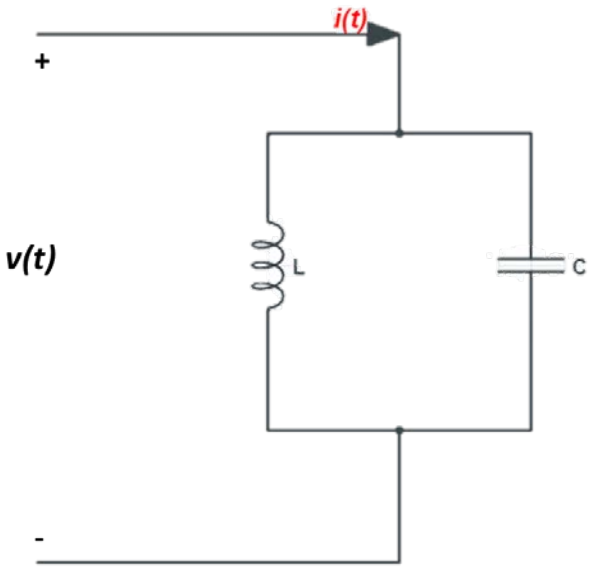

Figure 5.2 Ideal parallel LC circuit

The energy oscillation between the inductor and capacitor at the natural frequency steadily reduces the amplitude due to power losses as a result of the circuit resistance. If the circuit is driven by an external supply, resonance is achieved when the magnitude of the reactances of both components equal each other i.e.

$$|X_L| = |X_C| \tag{5.12}$$

$$\omega L = \frac{1}{\omega C} \tag{5.13}$$

Solving, we obtain

$$\omega_0 = \frac{1}{\sqrt{LC}} \tag{5.14}$$

Where L is the inductance in Henries, C is the capacitance in Farads and ω_0 is the natural resonant frequency in radians per second. In most instances, the resistance R of the inductor windings is taken into account and the equivalent circuit is shown in Figure 5.3. The resistance of this circuit is given by

$$Z_{Total} = \frac{1}{\frac{1}{R + X_L} + \frac{1}{X_C}} \tag{5.15}$$

A phasor diagram of the reactances is shown in Figure 5.4. Assuming $R << X_L$, the circuit impedance at resonance becomes

$$Z_{Total} = \frac{1}{\frac{1}{|X_L| \angle 90°} + \frac{1}{|X_C| \angle -90°}} \tag{5.16}$$

which approaches infinity. Thus, the circuit impedance is at its highest and entirely resistive (known as dynamic resistance) which makes the current minimal.

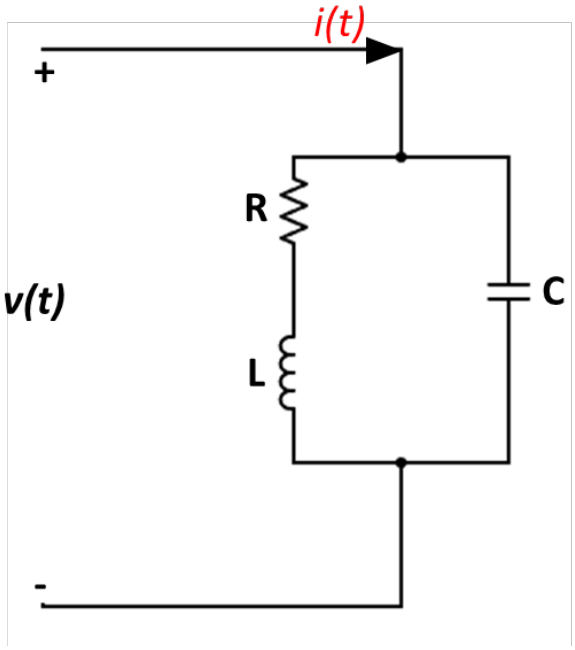

Figure 5.3 Parallel RLC circuit

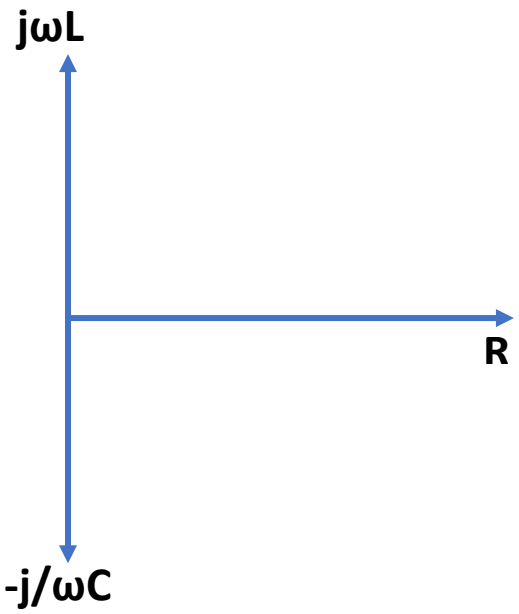

Figure 5.4 Phasor diagram of component reactances

Combining the impedances in the parallel branches,

$$Z_{Total} = (R + jX_L) \| (jX_C) = \frac{(R + jX_L)(jX_C)}{R + j(X_L + X_C)} = \frac{jRX_C - X_L X_C}{R + j(X_L + X_C)} \tag{5.17}$$

Rationalising the denominator, we obtain

$$Z_{Total} = \frac{RX_C^2 + j(R^2 X_C + X_C X_L^2 + X_L X_C^2)}{R^2 + (X_L + X_C)^2} \tag{5.18}$$

Since the impedance is purely resistive at resonance, it has no imaginary part. Therefore,

$$R^2 X_C + X_C X_L^2 + X_L X_C^2 = 0 \tag{5.19}$$

Dividing through by X_C,

$$X_L^2 = -X_L X_C - R^2$$

$$\omega^2 L^2 = \frac{L}{C} - R^2$$

$$\omega_0 = \sqrt{\frac{1}{LC} - \left(\frac{R}{L}\right)^2} \tag{5.20}$$

It can be seen that specific values of R, L and C can only resonate at a single frequency. However, the resonant frequency can be altered by varying one component value whilst keeping the others constant.

5.3 Experimental method

5.3.1 Test plate preparation

The Metglas 2605SC ribbon utilised previously in Chapter 4 was cut into rectangular strips measuring 48 mm by 7 mm, and a total of four strips (to increase the material volume and amplify the inductance changes) were stacked and glued together with an epoxy resin to obtain a solid core (with a demagnetising factor of approximately 0.003). The resulting amorphous sample was sandwiched between two 5 mm thick circular UHMWPE discs machined from solid blocks and measuring 50 mm in diameter. To allow for deflection of the ribbons when stressed, a 2 mm deep rectangular trench measuring 40 mm by 8 mm was bored centrally on the inner surface of the bottom disc. This was to ensure the induction of sufficient strain in the ribbons.

The low coefficient of friction of UHMWPE makes bonding difficult but this problem was circumvented by treating the surfaces with a polyolefin primer prior to bonding with a cyanoacrylate based adhesive. A profile of the resulting insert design is shown in Figure 5.5, where it can be noted that only a 40 mm section of ribbon actually experiences deflection due to strain. To simulate the femoral condyles, a model was fabricated from polypropylene (which has a higher compressive strength than UHMWPE at about 40 MPa) with spherical articulating surfaces of radius 20mm. This radius was selected in order to achieve initial contact stresses which fall within the reported range after TKR (about 30 – 60 MPa) [2, 3].

5.3.2 Measurement technique

The inserts were subjected to axial compressive loads varying from 100 N to 5000 N, using a *Zwick Roell Z050* materials testing machine, in the presence of an AC magnetic field generated by a pair of Helmholtz coils measuring 22cm in diameter and with 1470 turns each. The coils were fed by a *Krohn-Hite model 7500* wideband power

amplifier and were connected in parallel with a 0.01 µF capacitor to form a tuned (LC) circuit. The resonant frequency, the voltage across the tuned circuit as well as the line current through the circuit for each value of applied load were measured and recorded. Voltage and current (through the shunt) measurements were automated using two *Agilent 34401A* digital multimeters controlled using *LabVIEW* software. A diagram of the electrical circuit is shown in Figure 5.6, whilst the actual measurement apparatus used is shown in Figure 5.7. For each value of applied stress, five measurements were taken and the mean value recorded and analysed.

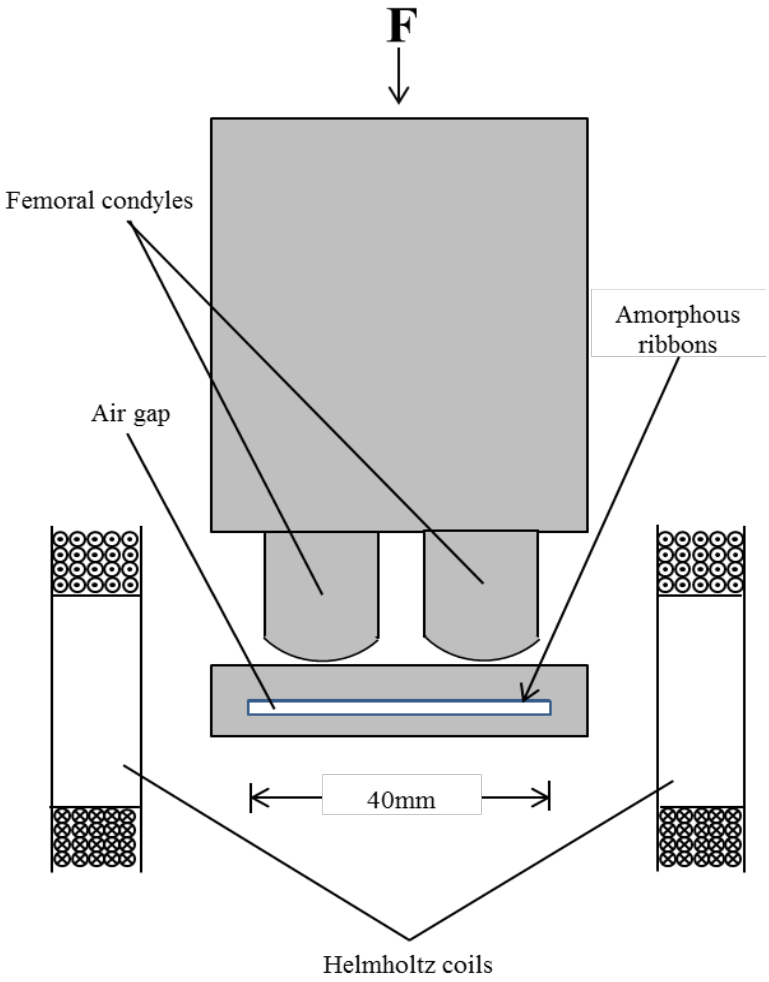

Figure 5.5 Cross-sectional view showing position of polypropylene condyles and UHMWPE insert within the Helmholtz coils

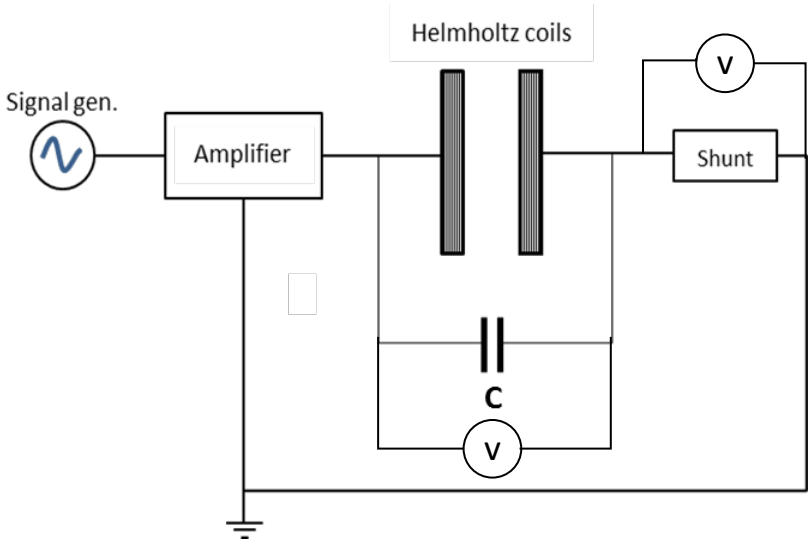

Figure 5.6 Schematic diagram of electrical measurement circuit.

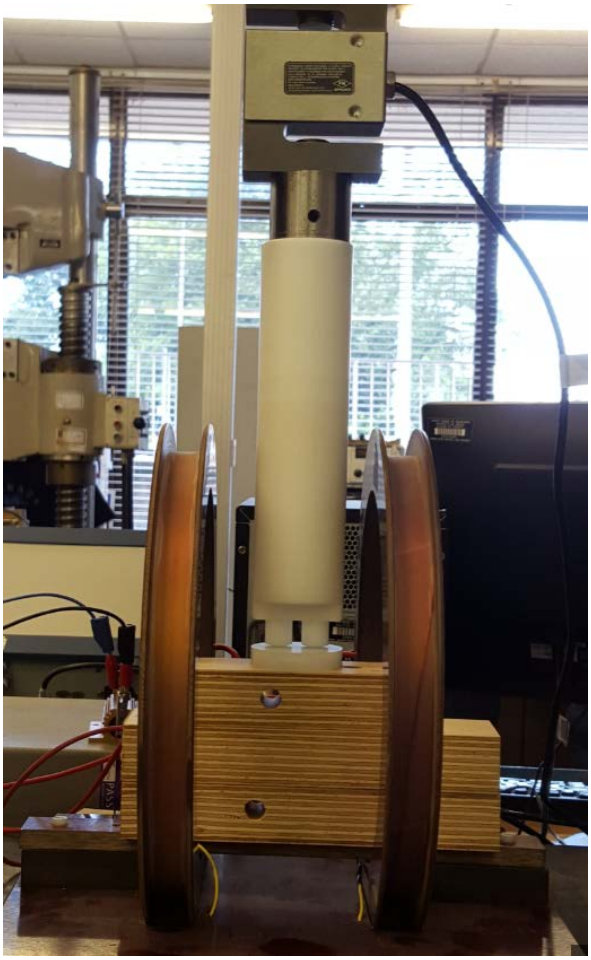

Figure 5.7 Actual measurement apparatus showing position of polypropylene condyles and UHMWPE insert within the Helmholtz coils

5.4 Results and explanation

A frequency sweep of the unloaded tuned circuit indicated that it resonated at 1.82 kHz as shown in Figure 5.8. At parallel resonance, the total circuit impedance is maximum which minimises the current by Ohms law. As mentioned earlier, the imaginary part of the circuit impedance tends to zero at resonance. Thus, from Equation 5.16, we obtain

$$Z_{Total} = \frac{X_c^2}{R}$$

Since the associated strains are small and both articulating surfaces are non-conforming, the value of applied stress was approximated using the Hertzian theory of non-adhesive elastic contact between a sphere and half-space [4]. The radius of the contact area between each condyle and the surface of the insert is given by

$$a = \sqrt[3]{\frac{3FR}{4E^*}}$$

where *F* is the applied force per condyle in Newtons. In this case, the effective radius (*R*) is the radius of the condyles since the insert is flat. The reduced modulus, *E**, can be defined as

$$E^* = \left(\frac{1 - v_1^2}{E_1} + \frac{1 - v_2^2}{E_2}\right)^{-1}$$

with $E_{1,2}$ and $v_{1,2}$ being the elastic moduli and Poisson's ratios for the condyles and insert respectively. The maximum contact pressure on the insert is given by

$$p_0 = \frac{3F}{2\pi a^2}$$

The forces were applied centrally to the fabricated condyles, hence, the force on each condyle was assumed to be equal to half of the total applied. The elastic moduli of polypropylene and UHMWPE were taken as 1.5 and 0.7 GPa respectively, whilst the Poisson's ratio for both materials was set as 0.45. The corresponding contact pressure values at the surface of the insert for the applied forces are presented in Table I. From the measured voltage and current values, the magnitude of the LC circuit impedances at different frequencies were calculated using Ohm's law and plotted as shown in Figure 5.9. The application of varying stress values causes changes in the permeability

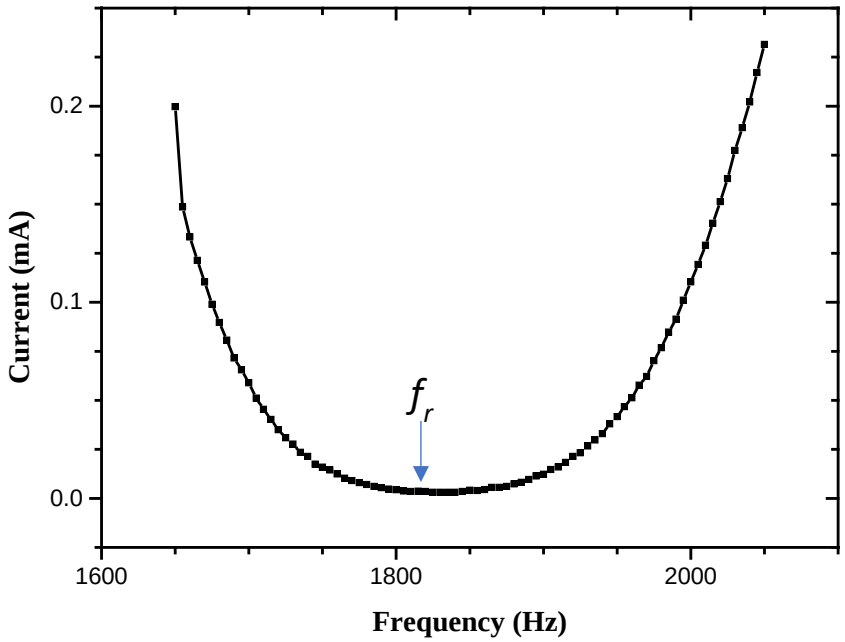

Figure 5.8 Frequency sweep of tank circuit showing unloaded resonant frequency.

Table 5.1 Calculated contact pressure for various values of applied force

Total applied force (Newtons)	Radius of contact area circle per condyle (mm)	Max. contact pressure per condyle (MPa)
100	1.08	20.54
200	1.36	25.88
300	1.55	29.62
400	1.71	32.60
500	1.84	35.12
1000	2.32	44.25
2000	2.93	55.75
3000	3.35	63.82
4000	3.69	70.24
5000	3.97	75.66

of the amorphous ribbons, which in turn varies the inductance of the surrounding Helmholtz coils. This inductance variation produces a proportionate change in the total impedance of the coil, as well as a shift in the circuit resonant frequency. As the insert wears out due to abrasion, the load bearing surface gets thinner; hence the deflection in the ribbons due to similar axial loading is more. This introduces more strain which further leads to a proportional change in initial permeability. It was observed that increasing the contact pressure whilst keeping the frequency constant resulted in a steady decay in the measured LC circuit impedance. For better comparison, normalised values of the measured impedance and corresponding contact pressure at different frequencies are plotted as shown in Figure 5.10.

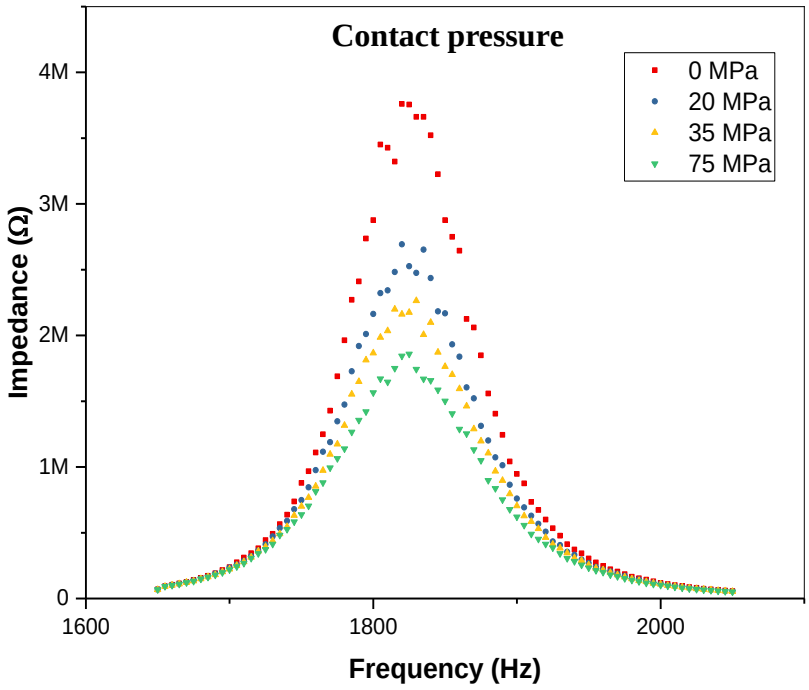

Figure 5.9 Measured impedance spectrum for various values of contact pressure

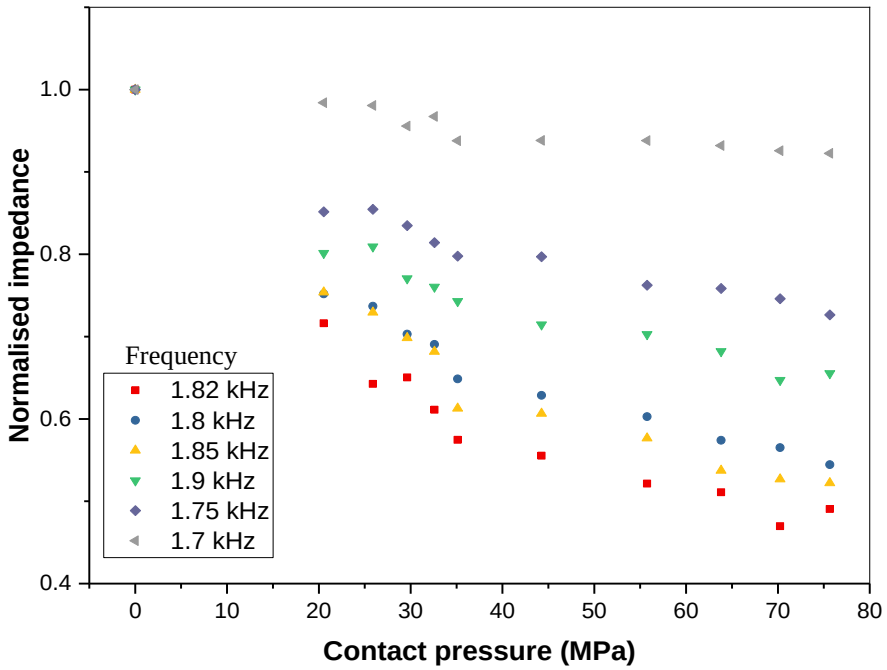

Figure 5.10 Normalised impedance versus contact pressure at various frequencies (adjusted $R^2 > 0.9$)

The variation remained approximately linear for contact pressure up to about 40 MPa before tapering off and the sensitivity was highest at resonance (evidenced by the steepest slope in the impedance-contact pressure curves in Figure 5.10) but this declined sharply as the frequency deviated from this value. Although the magnitude of the impedance varied considerably with applied pressure (over the range of about 2 MΩ), the changes in the actual inductance were quite small (a 2 mH variation compared to the measured coil inductance of 780 mH). A consequence of this was that the resonant frequency appeared fairly constant over the range measured. This may be overcome by using coils with lower inductance, such that small inductance changes will produce a significant and measurable shift in the resonant frequency. Also, using more sensitive meters with higher resolution will enable easier detection of resonance changes down to a few Hertz. Greater sensitivity may be realised by increasing the dimensions of the amorphous ribbons utilised, and eliminating random intrinsic stresses to obtain a uniaxial domain structure.

The repeatability has been assessed in terms of the standard deviation of the measured quantities at each frequency. The maximum standard deviation was about 0.08 and

this occurred when the insert was initially stressed. As the contact pressure increased to about 29 MPa, the standard deviation dropped to less than 0.04 and increasing the contact pressure beyond that dropped the deviation even further. Similarly, the maximum value of the normalised error of the impedance at the point of initial stress was 0.1 (at the resonant frequency) but this dropped steadily with increased loading to 0.06. This reported uncertainty is based on a standard uncertainty multiplied by a coverage factor k = 1, which provides a confidence level of approximately 68%.

Additional research can be carried out to determine optimal positioning of the amorphous ribbons within the insert for maximum stress transfer. The data obtained establishes that the set-up is suitable for measuring the peak contact pressure due to the combined axial forces which the insert is subjected to, up to about 70 MPa, which falls within the reported stresses after total knee replacement.

5.5 Summary

The objective of the work contained in this chapter was to relate the induced strain in the amorphous ribbons to inductance variation in adjacent Helmholtz coils, which can then be measured by resonant frequency tracking. The obtained results show a decrease in coil impedance with increased stress; however, there was minimal change in the measured resonant frequency due to the high inherent inductance of the utilised coils. In addition, it was established that the measured sensitivity peaked at the resonant frequency.

References

[1] D. Okhiria, T. Meydan, and P.I. Williams (2016). Non-Invasive Measurement of Stress Levels in Knee Implants Using a Magnetic-Based Detection Method. *IEEE Transactions on Magnetics*, 52(5), pp.1-4.

[2] J. Szivek, P. Anderson and J. Benjamin, 'Average and peak contact stress distribution evaluation of total knee arthroplasties', The Journal of Arthroplasty, vol. 11, no. 8, pp. 952-963, 1996.

[3] M. Kuster, G. Wood, G. Stachowiak and A. Gachter, 'Joint load considerations in total knee replacement', The Bone and Joint Journal, vol. 79-, no. 1, pp. 109-113, 1997.

[4] K. L. Johnson, *Contact mechanics*. Cambridge [Cambridgeshire]: Cambridge University Press, 1985, pp 90 – 93.

6. Finite Element Modelling of knee implant stresses

6.1 Synopsis

The wear and damage of the polyethylene insert remains a dominant cause of revision surgeries, and this wear is generally attributed to the existing contact stresses. These stresses frequently surpass the yield strength of UHMWPE due to the reduced contact area of the articulating surfaces after total knee replacement. Research on the contact stresses have previously been estimated using mathematical models or measured with pressure sensors subjected to predicted knee forces. A Finite Element Model (FEM) of the components utilised in this research was created in order to have a better comprehension of the associated contact stresses and strains the designed tibial insert is subjected to.

6.2 Analytical approach

6.2.1 Implant geometry and design

A Finite Element Model (FEM) of the knee system was designed using COMSOL Multiphysics version 5.0, which is a commercially available software. The femoral component and the polyethylene insert were both modelled as detailed below.

i. Femoral component

The femoral component was modelled as a rigid indenter, with its dimensions taken from the natural knee. This was done to ensure universality of the study; hence the model can be adapted to suit various implant designs.

To achieve this, a 3-dimensional surface scan of an adult femur was imported into a CAD software and extruded to form a solid body. A 20 mm partition was then created to define the CoCrMo region of the component which was used as the indenter, as shown in Figure 6.1.

ii. Tibial insert

The peripheral dimensions of the tibial insert are as shown in Figure 6.2. Its design was split into two parts. The bottom part was 5 mm thick, with two 2 mm deep rectangular trenches measuring 30 mm by 10 mm located on its inner surface. The trenches were positioned 4 mm apart, thus providing a fulcrum for improved stress deformation.

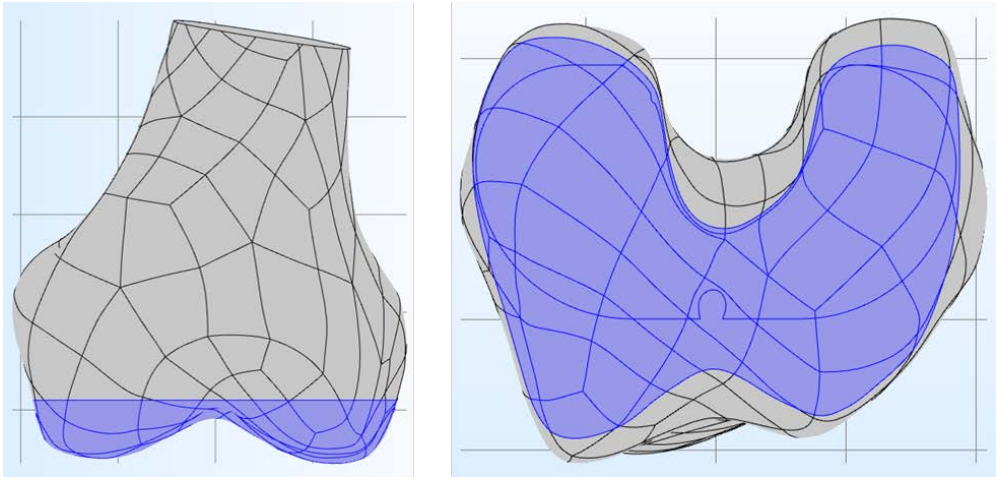

Figure 6.1 Femoral component indenter, with the CoCrMo region highlighted

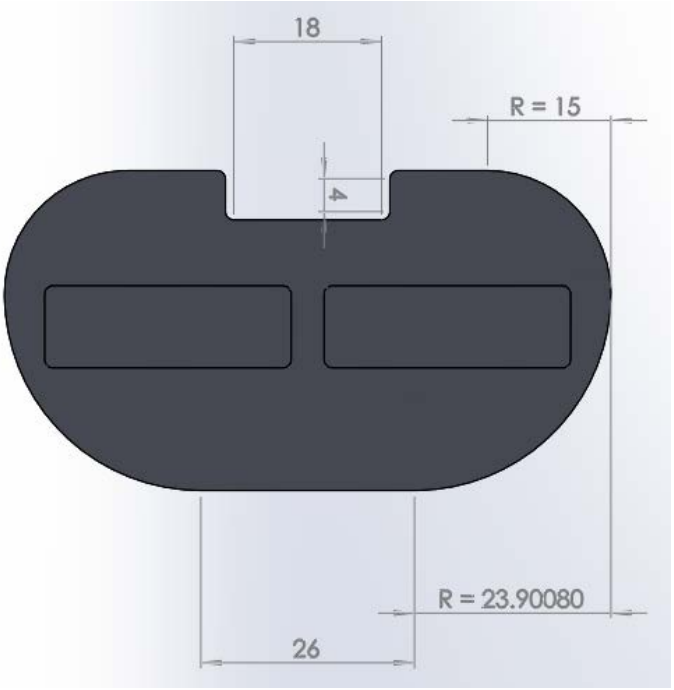

Figure 6.2 Peripheral dimensions of the modelled tibial insert (all dimensions in *mm*)

The concave articulating surfaces of the top part were designed to have 100% conformity with the femoral component in order to maximise the contact area. A larger contact area between the articulating surfaces serves to minimise the contact pressure which could potentially lower wear rates, although previous research indicates that reducing tibiofemoral condylar conformity helps to prolong implant lifespan [1 – 3]. However, for the purposes of this research, a fully conforming design was used in order to provide a higher contact surface area such that low contact pressure values are still detectable. To achieve this, the thickness of the top part of the insert was initially extruded to 12 mm and the articulating surface of the femoral component subtracted. Two different thicknesses were specified, with the distance between the lowest contact point on the articulating surface and the base of the top part varied by 1 mm. The components were then assembled to form a single part using the mates function available in SolidWorks CAD software, as depicted in Figure 6.3.

6.2.2 Material properties of UHMWPE and CoCrMo alloy

The entities described above were imported into the COMSOL software, and an assembly was formed in order to create a contact pair between the articulating surfaces as shown in Figure 6.4. The properties detailed in Table 6.1 were defined for the different materials which constitute each domain. To obtain the Young's modulus of UHMWPE, tensile tests were carried out using standardised methods as specified in ASTM D638 which deals with the properties of plastics [4].

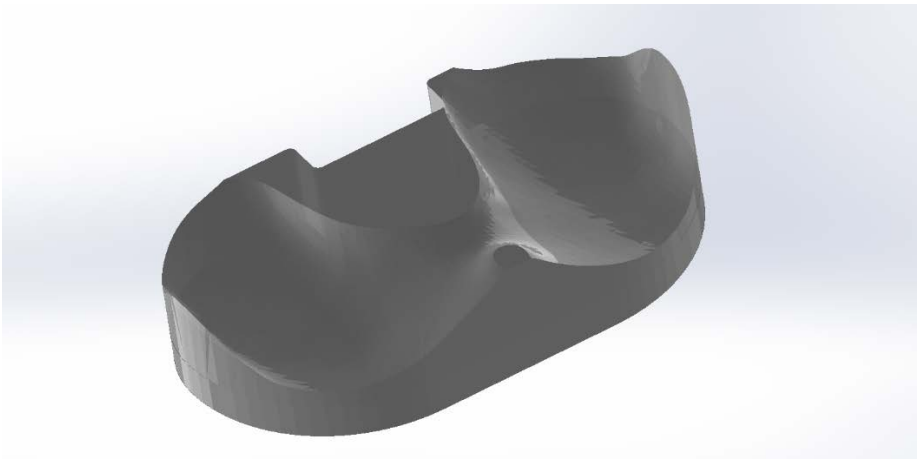

Figure 6.3 Designed tibial insert with both components mated

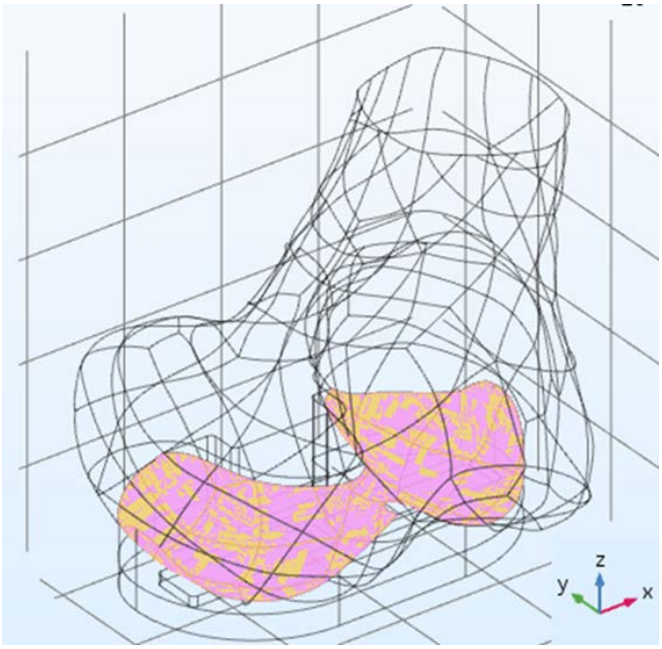

Figure 6.4 Femoral and tibial components assembled with highlighted contact surfaces

Five sets of measurements were taken and averaged, and the specimens used with their dimensions are shown in Figure 6.5. The resulting engineering stress-strain curve was then converted into a true stress-strain curve, the relationship between both quantities given as

$$\sigma_t = \sigma_e(1 + \varepsilon_e) \tag{6.1}$$

$$\varepsilon_t = \ln(1 + \varepsilon_e) \tag{6.2}$$

where σ_t and ε_t are the true stress and strain values respectively, with σ_e and ε_e being the engineering equivalents.

Table 6.1 UHMWPE and CoCrMo properties used in modelling [5 – 8]

	UHMWPE	**CoCrMo**
Density (g/cm^3)	0.93	8.3
Young's modulus (GPa)	From stress-strain data	200
Poisson's ratio	0.45	0.29

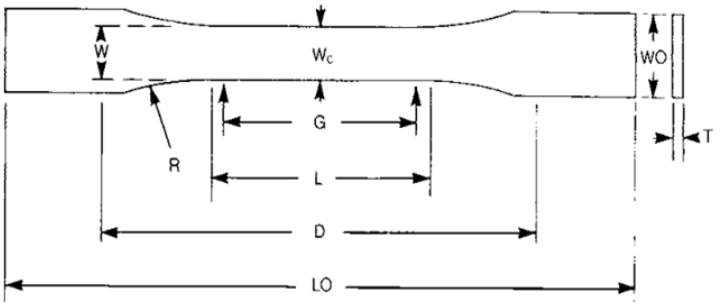

Dimensions (see drawings)	7 (0.28) Type I
W—Width of narrow section[E,F]	13 (0.50)
L—Length of narrow section	57 (2.25)
WO—Width overall, min[G]	19 (0.75)
WO—Width overall, min[G]	...
LO—Length overall, min[H]	165 (6.5)
G—Gage length[I]	50 (2.00)
G—Gage length[I]	...
D—Distance between grips	115 (4.5)
R—Radius of fillet	76 (3.00)
RO—Outer radius (Type IV)	...

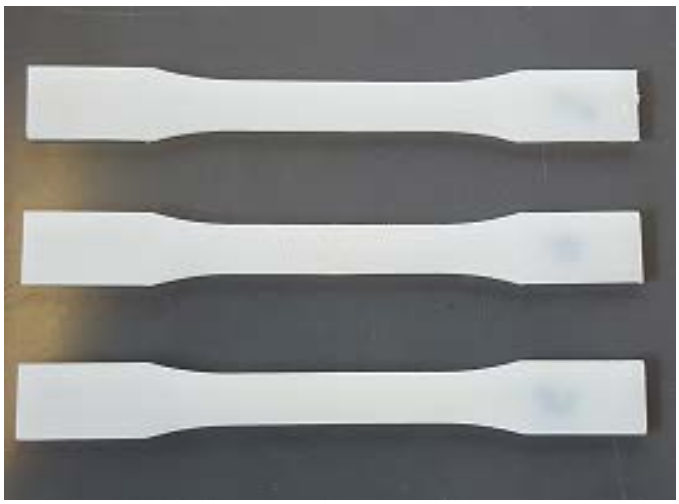

Figure 6.5 UHMWPE specimens (type I) utilised in tensile testing

The depletion of UHMWPE in tibial inserts has already been associated with the yield stress. Even though polyethylene has previously been modelled as elastic-perfectly plastic material (i.e. the strain increases at the yield point without further increase in stress), its true stress strain relationship shows some strain hardening. The yield criteria are often specified using Von Mises stresses whereby the material exhibits purely elastic properties up to the yield point, and strain hardening beyond this limit.

Thus, the UHMWPE insert was modelled as a non-linear elastoplastic material, and the values obtained from the true stress-strain curve were integrated using the Ramberg-Osgood relationship [9] given by

$$\varepsilon_a = \frac{\sigma_a}{E} + \varepsilon_{ref}\left(\frac{\sigma_a}{\sigma_{ref}}\right)^n \tag{6.3}$$

where E is the initial elastic modulus, n is the strain hardening exponent, ε_{ref} is the reference strain at the offset yield strength (usually 2% in plastics) [10 – 11] and σ_{ref} is the stress at the reference strain. These parameters were derived graphically from the true stress-strain curve as shown in Figure 6.6, while the strain hardening exponent was obtained by

$$n = \frac{\ln 20}{\ln \frac{\sigma_{ref}}{\sigma_p}} \tag{6.4}$$

With σ_p being the proportionality limit, which is the region of the stress strain curve where Hooke's law applies. σ_p and E were determined to be 9 MPa and 370 MPa respectively, thus, $n = 4.669\ and\ \sigma_{ref} = 17.1\ MPa$.

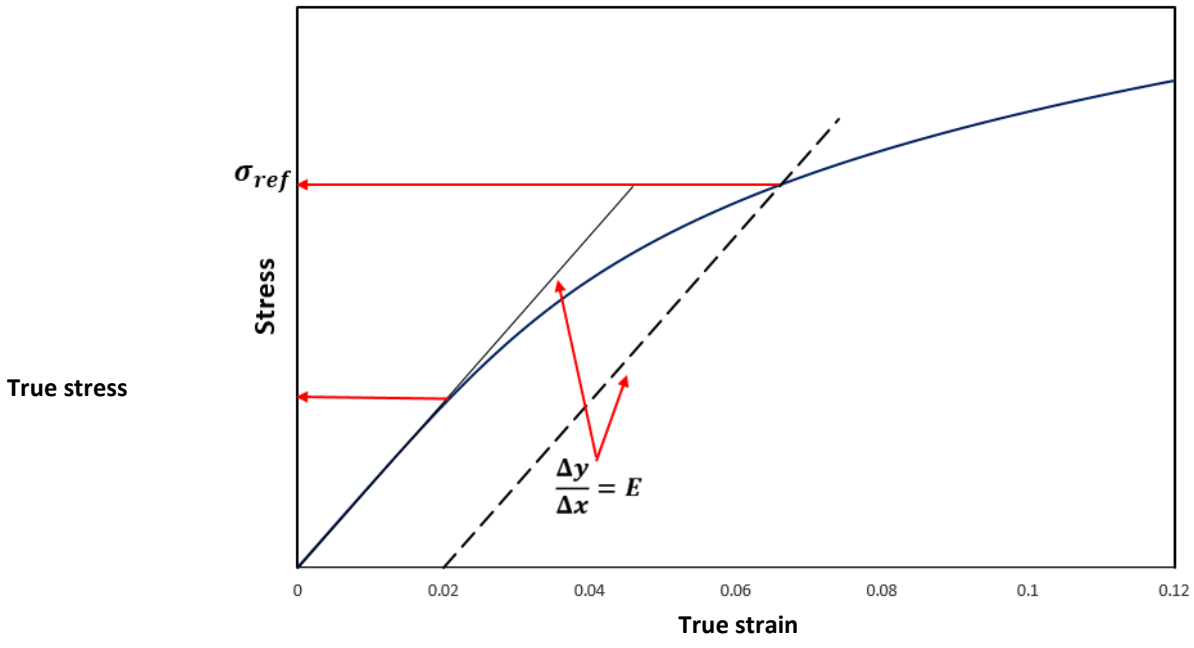

Figure 6.6 Graphical determination of Ramberg-Osgood parameters

6.2.3 Loads, constraints and meshing

This current study deals with axial pressure as previous research shows that it accounts for over 95% of the loads during the stance phase of measured activities. Hence, the load on the femoral indenter was simulated with a downward acting body load (denoted as a negative value in the *z*-direction) up to 3000 N. A fixed boundary condition was applied to the base of the insert, and no displacement in the *x* and *y* directions were permitted.

Tetrahedral elements were used in the entire geometry meshing due to the complex topology of the model to ensure convergence. An adaptive refinement using the L2-norm (least squares) error estimation was then applied for mesh optimisation.

6.3 Results and explanation

The main objective of this FEM study was to investigate the stresses the designed tibial insert is subjected to. The true stress-strain curve obtained from the tensile tests is plotted in Figure 6.7, alongside that derived from the Ramberg-Osgood equation for comparison. For each value of force applied, the contact pressure on the articulating surface of the tibial insert as well as the strain of the sensor surface were obtained. The reference surfaces where these values were calculated are highlighted in Figure 6.8. It should be noted that the contact surface area differed in each insert, as tabulated in Table 6.2.

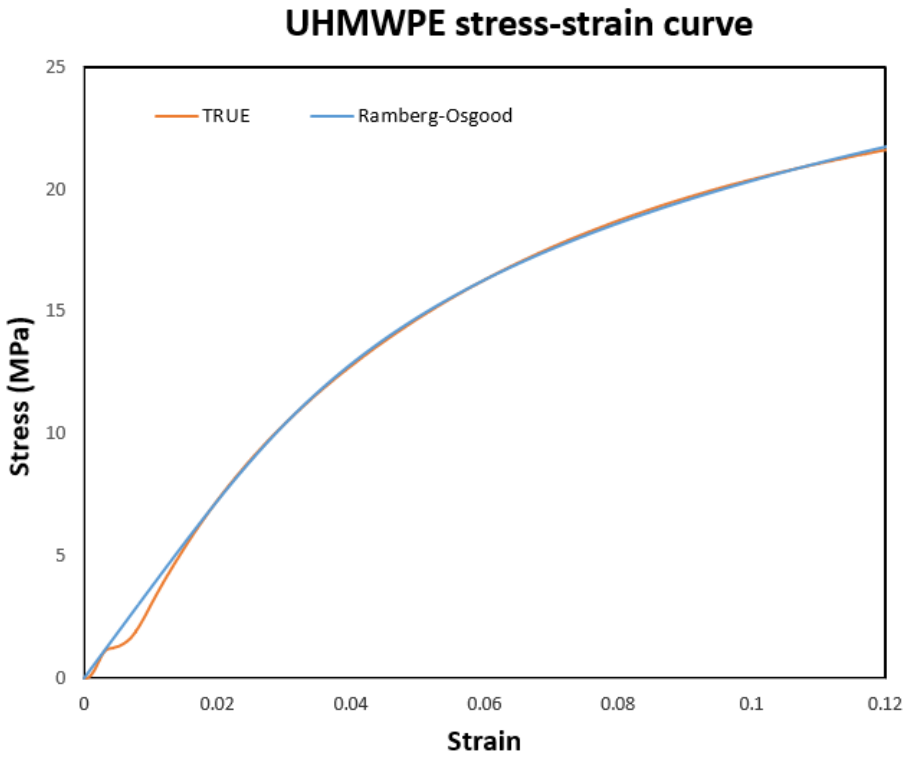

Figure 6.7 Graphical comparison between experimental true and Ramberg-Osgood stress-strain curve used in simulation

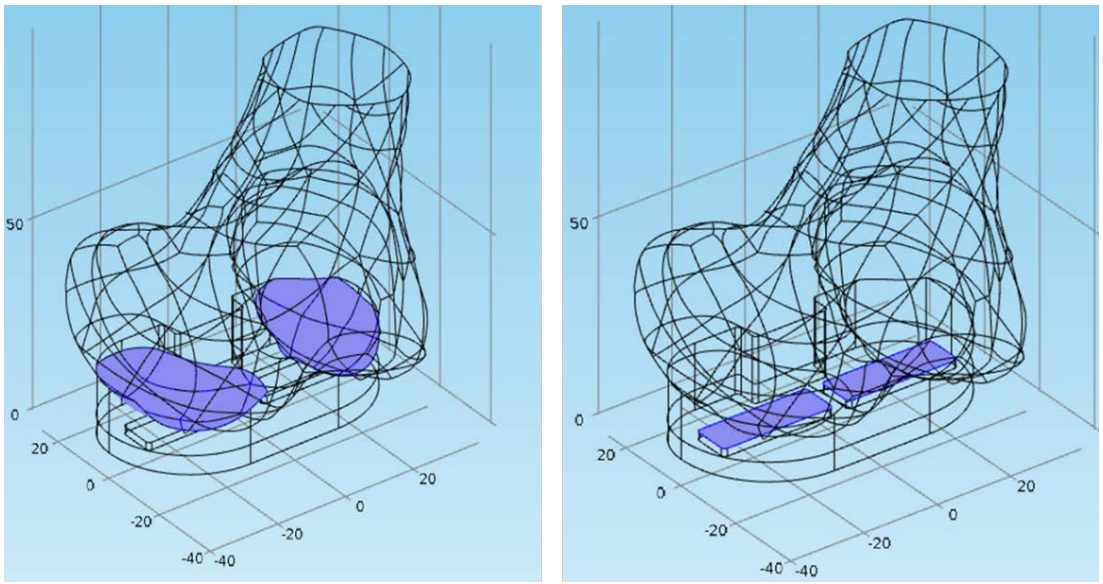

Figure 6.8 Surfaces for contact pressure and sensor strain calculations

Table 6.2 Tibiofemoral contact surface area for each insert

Insert	Contact area (mm^2)
1	2238.6
2	2476.8

Figure 6.9 shows a plot of the articulating tibiofemoral surface contact pressure against the applied force for each insert where expectedly, a direct and almost linear variation exists between the two quantities. For each value of applied force, the contact pressure was observed to decrease as the surface area increased in the inserts. This validates the model and supports the hypothesis that wear rates are lowered with larger contact areas, since sliding (abrasive) wear has been linked to contact stress. The contact pressure in the thicker insert (insert 1) varied up to 1.5 MPa, and this dropped down to 1.35 MPa in the thinner insert (insert 2) for the same value of applied force.

As previously mentioned in Section 2.3.4, the magnetoelastic energy in a ferromagnetic material is related to the induced anisotropic strain in its domain structure. This strain is due to the alignment of the domains parallel to the direction of the externally applied field, which in this instance is the *x*-direction of the coordinate system employed in the model. A plot of the uniaxial longitudinal strain at the sensor surface against the applied force is as shown in Figure 6.10.

Although the articulating surface contact pressure was lower in insert 2, the strain at the sensor surface was largest in this insert. This is attributable to the reduced polyethylene thickness between the articulating and sensor surfaces. The strain obtained was about 0.290 ppm/N in insert 2, as compared to 0.259 ppm/N in insert 1.

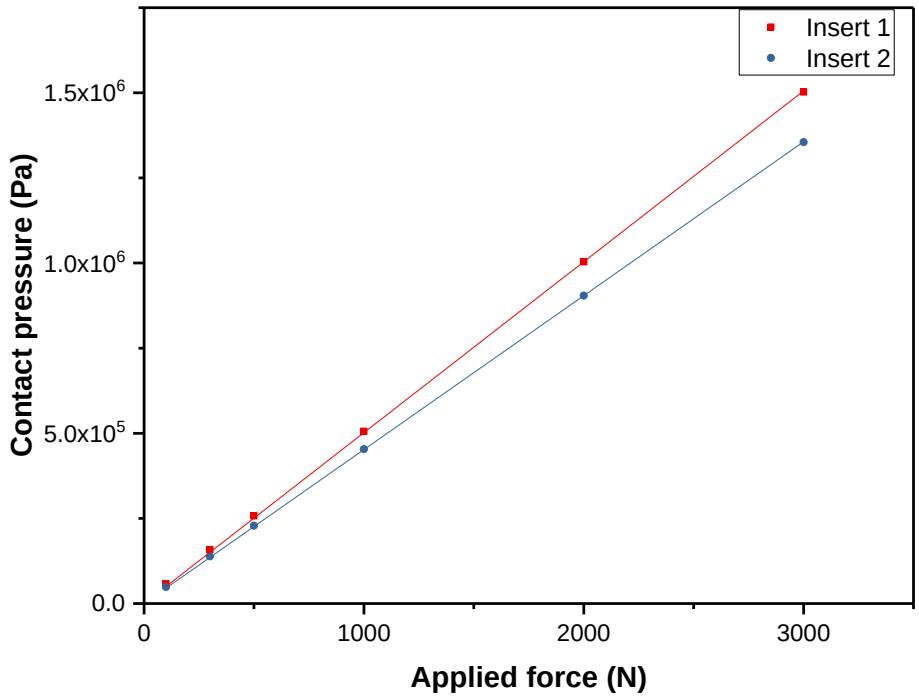

Figure 6.9 Applied force against tibiofemoral surface contact pressure (adjusted $R^2 > 0.9$**)**

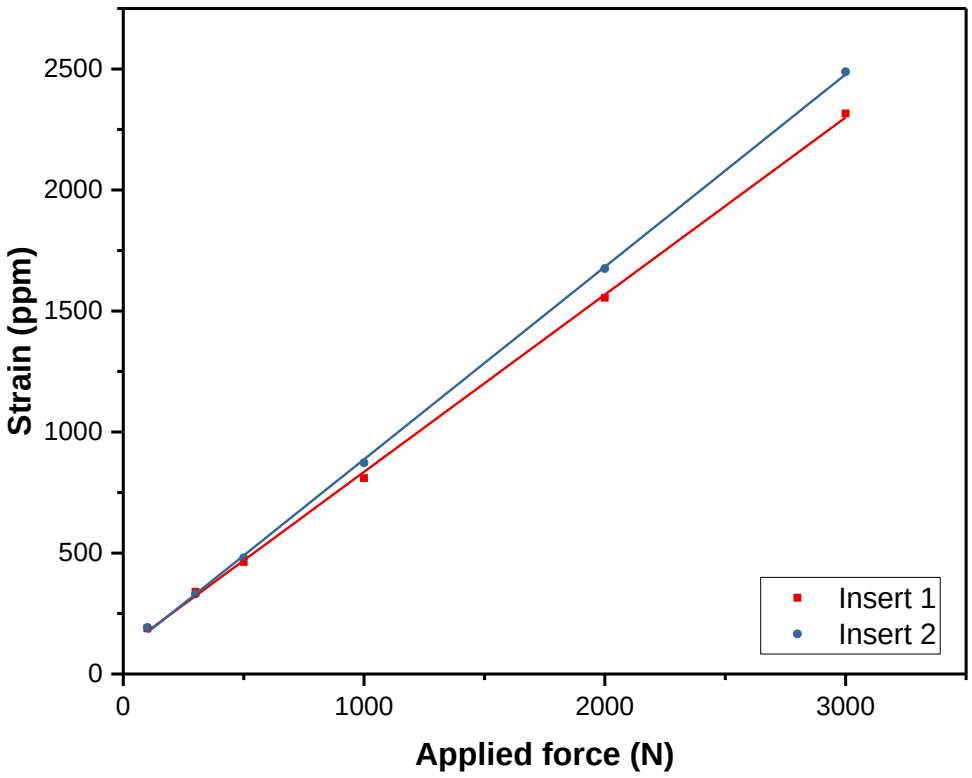

Figure 6.10 Applied force against uniaxial (*x*-direction) strain (adjusted $R^2 > 0.9$**)**

The stresses in knee implants are usually reported in terms of the peak contact pressure the tibial insert is subjected to at the tibiofemoral surface, and these have been plotted in Figure 6.11. The peak contact pressure in both inserts ranged between 6 – 15 MPa.

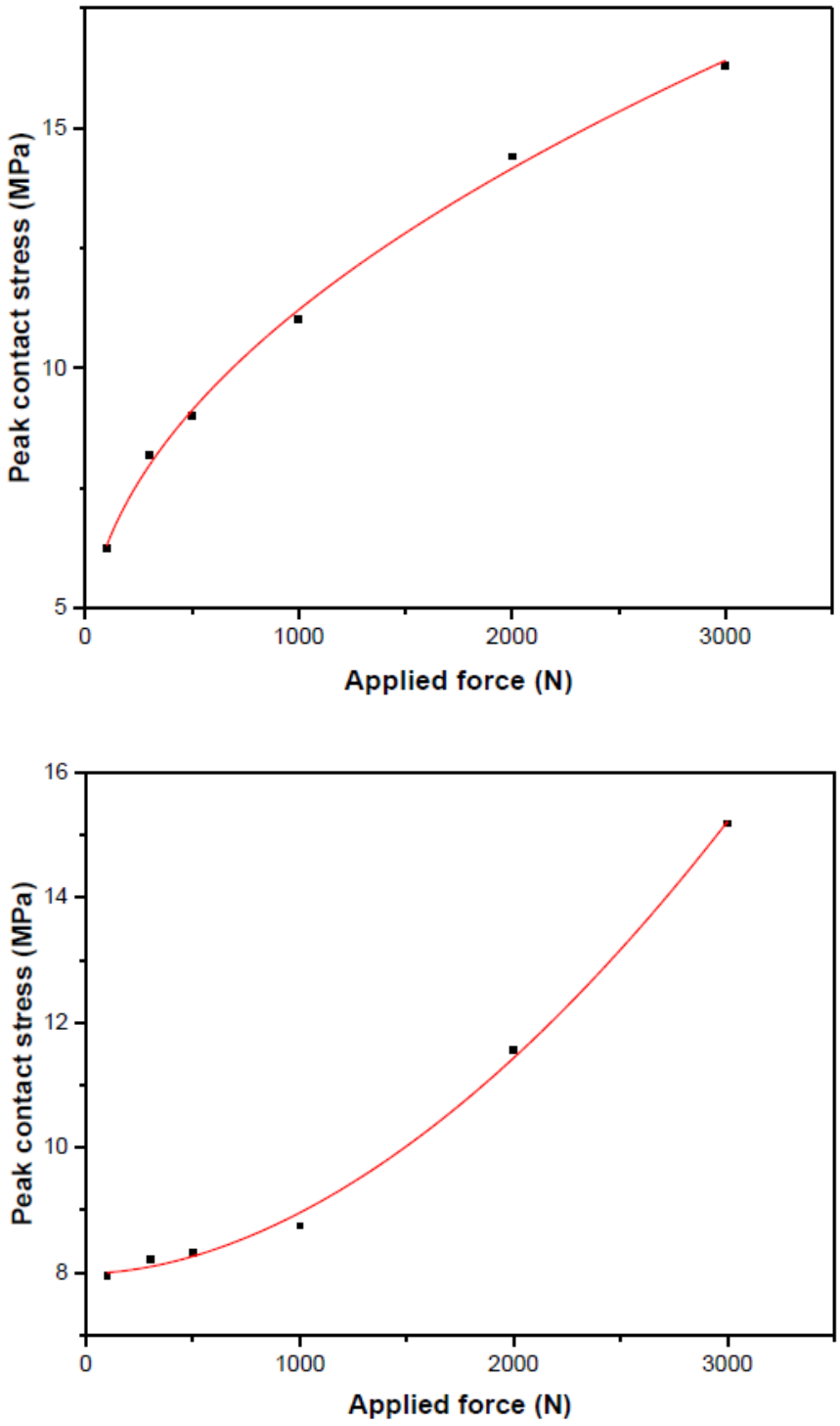

Figure 6.11 Modelled peak contact stresses at various loads (Top: insert 1, bottom: insert 2)

6.4 Summary

This chapter aimed at modelling the stresses and strains the designed insert is subject to, in order to create a picture of what occurs within it. The contact pressure at the insert surface, as well as the strain at the sensor surface, varied directly with the applied force as expected while the strain at the sensor surface varied inversely with the polyethylene thickness.

References

[1] Abdelgaied, A., Brockett, C., Liu, F., Jennings, L., Jin, Z. and Fisher, J. (2014). The effect of insert conformity and material on total knee replacement wear. *Proceedings of the Institution of Mechanical Engineers, Part H: Journal of Engineering in Medicine*, 228(1), pp.98-106.

[2] Fregly, B., Marquez-Barrientos, C., Banks, S. and DesJardins, J. (2010). Increased Conformity Offers Diminishing Returns for Reducing Total Knee Replacement Wear. Journal of Biomechanical Engineering, 132(2), p.021007.

[3] Walker, P. and Hsieh, H. (1977). Conformity in condylar replacement knee prostheses. The Bone and Joint Journal, 59-B (2), pp.222-228.

[4] ASTM D638-14 (2014). Standard Test Method for Tensile Properties of Plastics.

[5] Direct Plastics. UHMWPE Sheet - Direct Plastics Limited. [online] Available at: https://www.directplastics.co.uk/uhmwpe-sheet [Accessed 15 Jan. 2016].

[6] Goodfellow. Polyethylene - U.H.M.W. Material information. [online] Available at: http://www.goodfellow.com/E/Polyethylene-UHMW.html [Accessed 15 Jan. 2016].

[7] 3T RPD Ltd. Material Specification - Cobalt Chrome Alloy Co28Cr6Mo. [online] Available at: http://www.3trpd.co.uk/wp-content/uploads/2013/03/cobalt-chrome-alloy-co28-cr6mo-2012.pdf [Accessed 15 Jun. 2016].

[8] American Elements. Cobalt Chromium Molybdenum Alloy. [online] Available at: http://www.americanelements.com/cobalt-chromium-molybdenum-alloy [Accessed 15 Jan. 2016].

[9] Ramberg, W., & Osgood, W. R. (1943). Description of stress–strain curves by three parameters. *Technical Note No. 902*, National Advisory Committee for Aeronautics, Washington DC.

[10] NDT Resource Center. Tensile Properties. [online] Available at: https://www.nde-ed.org/EducationResources/CommunityCollege/Materials/Mechanical/Tensile.htm [Accessed 19 Jan. 2016]

[11] Instron. Yield Strength. [online] Available at: http://www.instron.co.uk/en-gb/our-company/library/glossary/y/yield-strength [Accessed 19 Jan. 2016].

7. Force measurements using resonant frequency tracking

7.1 Synopsis

Previously, it was established that the inductance of the Helmholtz coils can be varied due to changes in the permeability of the amorphous ribbon situated at its centre. One way of better visualising this variation is by forming a tuned LC circuit and tracking its resonant frequency. This was achieved by using low inductance coils, such that changes in the coil inductance produced sufficiently measurable variations in the circuit resonant frequency.

7.2 Experimental method

7.2.1 Helmholtz coil design

The method and equipment used were mostly the same as those in the Chapter 5, with a few changes made. From Equation 2.14, the inductance of a solenoidal coil is given by

$$L = \frac{\mu N^2 A}{l}$$

It is evident from the equation above that the inductance value can be lowered by reducing both the number of turns in the coil and the coil diameter. For this procedure, single-layer Helmholtz coils with a 15cm diameter and 100 turns each were fabricated using 0.4 mm diameter copper wire on 3D printed polylactide (PLA) reels and utilised, as shown in Figure 7.1. The diameter of the coils was selected in order to minimise the inductance, but still be largely sufficient to fit around an average adult knee. To ensure the selection of a suitable operating range for the sensor, the self-resonant frequency of the fabricated coil was determined by sweeping the input frequency and measuring the impedance across the coil, using an *Agilent 4294A* precision impedance analyzer. The self-resonant frequency of the coil, which relates to the maximum impedance, was established to be about 165 kHz as presented in Figure 7.2.

Figure 7.1 Fabricated Helmholtz coils

7.2.2 Femoral component fabrication

The femoral component was modelled on the geometry of the natural knee condyles, using a 3D scan of an adult knee. To better simulate the knee replacement prosthesis, a femoral component was manufactured from medical grade CoCrMo (ASTM F75) by direct metal laser sintering (DMLS). This additive manufacturing technique fuses

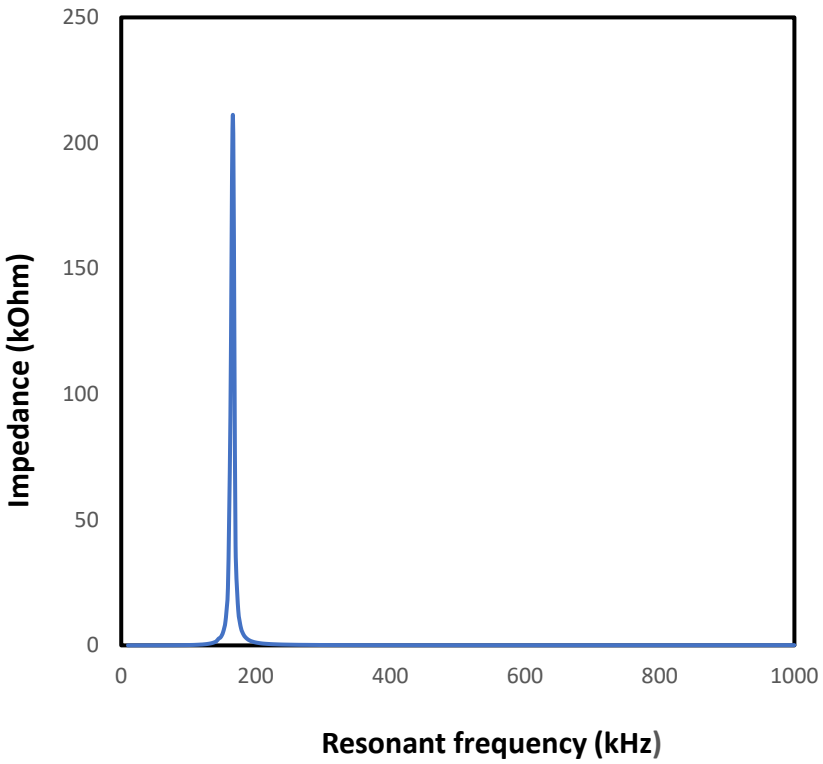

Figure 7.2 Frequency sweep of fabricated Helmholtz coils showing self-resonant frequency

fine metallic powders by aiming a high powered ytterbium fibre laser at specific points predefined by a computer aided design (CAD) model to produce a solid three-dimensional structure [1, 2]. The designed model is shown in Figure 7.3.

Figure 7.3 Design of 3D printed CoCrMo component

To do this, a thin layer of metal powder is deposited on the pre-heated building platform in the print chamber. Since the temperature of the platform is below the melting point of the powder, no fusion occurs. The laser is then aimed at regions defined in the CAD model, heating them above the melting point and solidifying a cross-sectional portion of the model. The building platform is then lowered, an additional powder layer deposited and the process repeated until the complete part is sintered. This process is depicted in Figure 7.4.

The CoCrMo component produced was mounted on to a femur fabricated from polyamide (PA) by selective laser sintering (SLS). This procedure is similar to DMLS; however, SLS produces parts with a lower resolution as compared to DMLS which uses powders with smaller diameter. Also, whilst DMLS is primarily used for metallic parts, SLS can be applied to a variety of materials like plastics, ceramics and glass. The resulting indenter is shown in Figure 7.5.

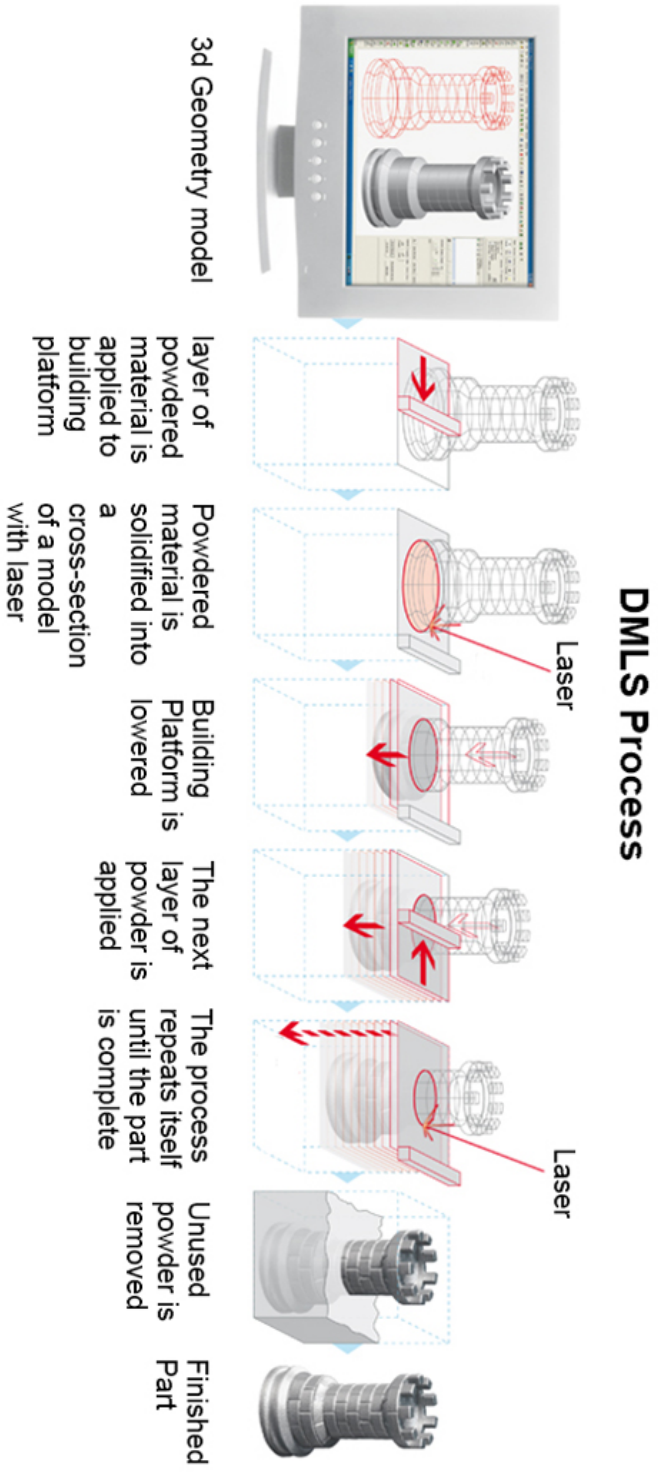

Figure 7.4 Direct metal laser sintering process [3]

Figure 7.5 Side, front and articulating surface of the fabricated CoCr component mounted on a polyamide femur

7.2.3 Tibial insert fabrication

The insert parts described in Section 6.2.1(ii) were machined out of solid UHMWPE blocks and fabricated as two parts bonded with an adhesive, as described in Section 5.3. Four Metglas 2605SC amorphous ribbon strips measuring 70 mm by 8 mm were stacked and bonded together with an epoxy resin to form the magnetic transducer. This was then secured onto the inner surface of the upper part of the insert first by treating the surface with a polyolefin primer, and then bonding with a cyanoacrylate based adhesive. After allowing the bond to set, both parts of the insert were then fused together using the same primer and adhesive. This process was repeated for all the inserts produced, whilst ensuring that the amorphous ribbon transducer was secured at the same position in each insert. Figure 7.6 shows the resultant inserts, and two of each one were fabricated.

The inserts were located at the centre of the Helmholtz coils as shown in Figure 7.7, and were subjected to increasing static axial compressive loads varying from 100 N to 3000 N in the presence of an AC magnetic field using the same *Zwick Roell* Z050 materials testing machine and circuitry as before (see Figure 5.4). Automated measurements of the resonant frequency, voltage across the tuned circuit as well as the line current through the circuit for each value of applied load were recorded using two *Agilent* 34401A digital multimeters controlled by LabVIEW software.

Figure 7.6 Fabricated UHMWPE inserts with amorphous ribbon embedded (Top: insert 1, bottom: insert 2)

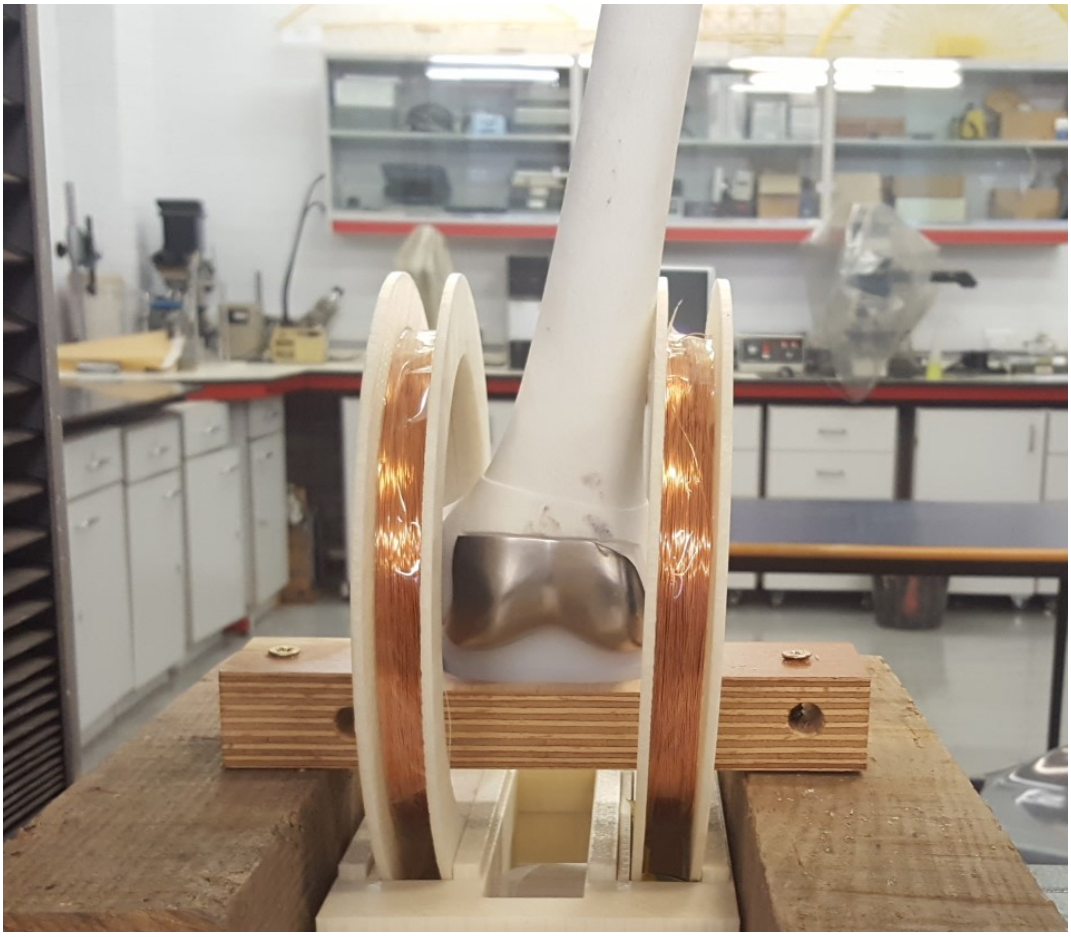

Figure 7.7 Experimental assembly showing position of tibial insert and femoral component within the Helmholtz coils.

7.3 Results and explanation

A plot of the impedance of the tuned circuit against its operating frequency is shown in Figure 7.8. The internal resistance of the circuit provides damping, which makes its differential equation comparable to that of a mass on a damped spring. Thus, a Lorentzian curve fitting was applied to the measured data and the resonant frequency of about 20.6 kHz was obtained.

Figures 7.9 and 7.10 show the resonant frequency measured for various values of applied force in each insert. It was observed that increasing the applied force resulted in a constant decrease in the measured resonant frequency. This is better visualised in Figure 7.11, which shows a steady leftward shift in the impedance curves as the applied force is increased. In addition to this, the peak value of the measured impedance curve decreases as the applied force is increased. Both observations are apparently a result of changing values of the coil inductance, brought about by the variations in the permeability of the amorphous ribbon located at the coil centre.

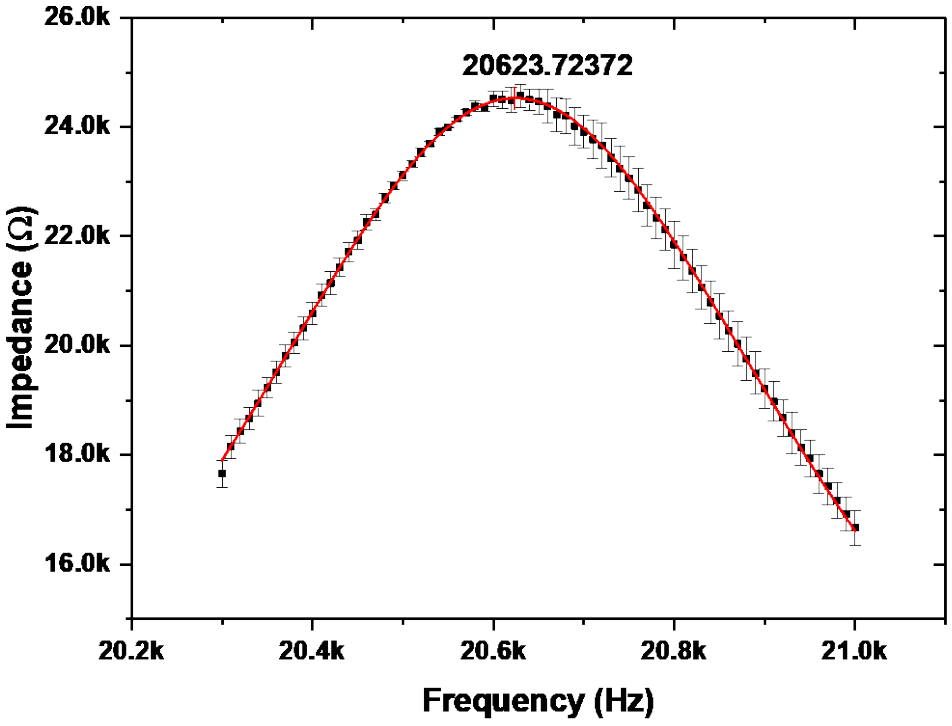

Figure 7.8 Frequency sweep of tuned circuit showing resonant frequency

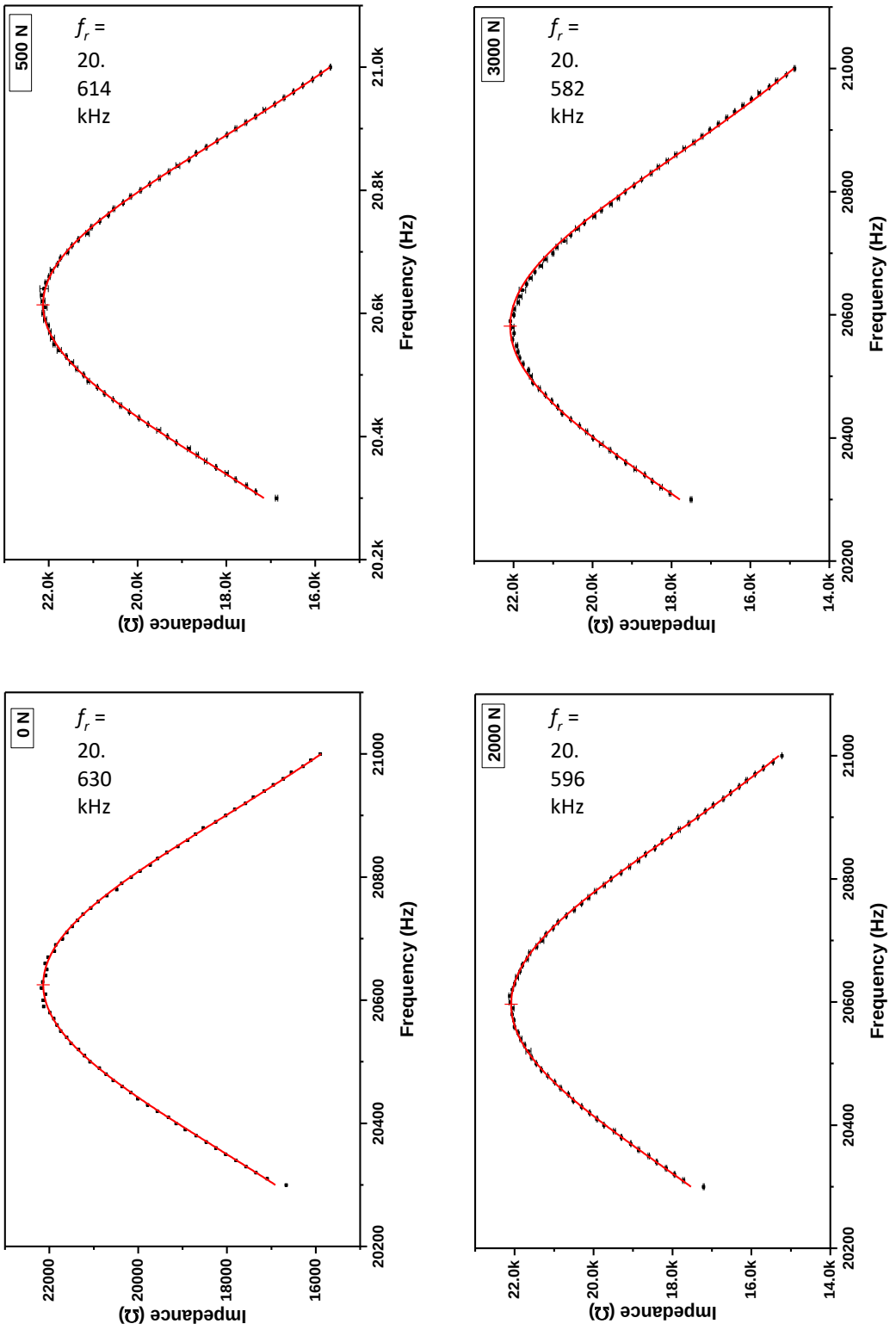

Figure 7.9 Cross section of measured impedance curves for various applied force values in insert 1

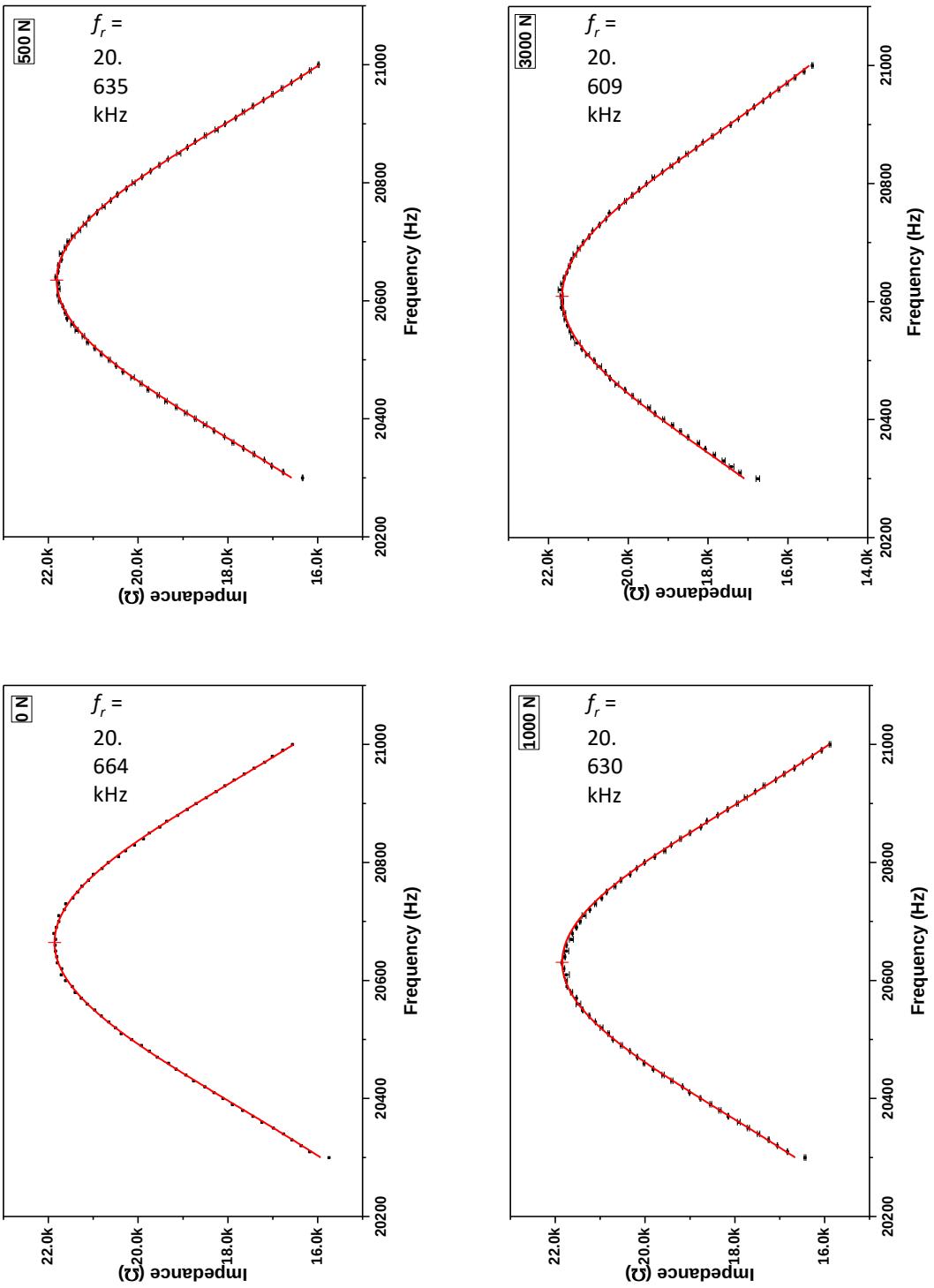

Figure 7.10 Cross section of measured impedance curves for various applied force values in insert 2

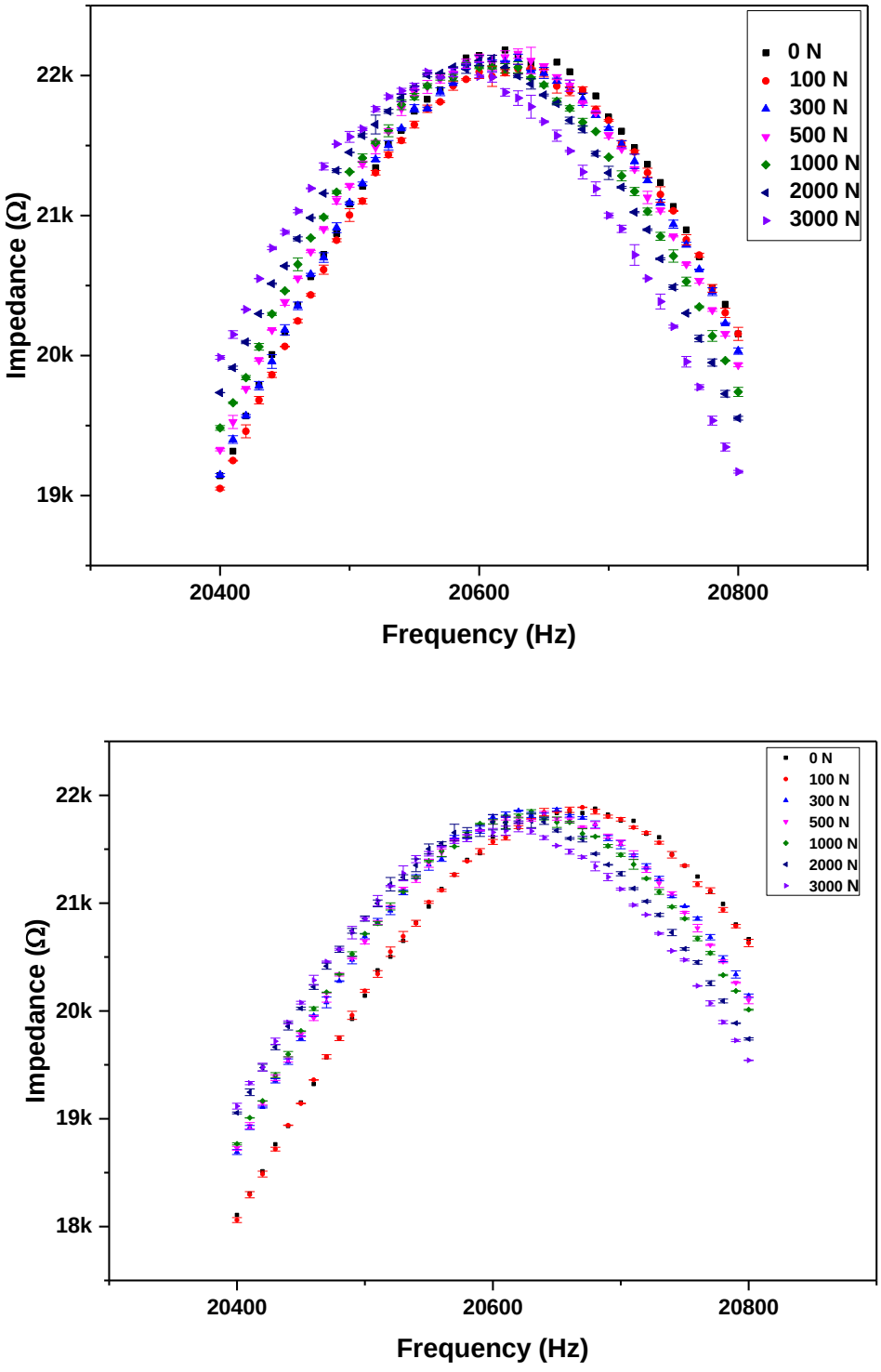

Figure 7.11 Impedance curves showing steady shift in resonant frequency with applied force (top: insert 1, bottom: insert 2)

Recall from Equation 5.18 that

$$\omega_0 = \sqrt{\frac{1}{LC} - \left(\frac{R}{L}\right)^2}$$

Rearranging, we obtain

$$\omega_0^2 L^2 C - L + R^2 C = 0 \tag{7.1}$$

This is easily recognised as a quadratic equation with L being the unknown variable, $\omega^2 C$ the quadratic coefficient, -1 the linear coefficient and $R^2 C$ a constant. The solution is given by

$$L = \frac{-1 \pm \sqrt{1 - 4\omega_0^2 R^2 C^2}}{2\omega_0^2 C} \tag{7.2}$$

From the measurements taken to obtain the self-resonant frequency of the fabricated Helmholtz coils, at 20.6 kHz

$$R \cong 18.3\ \Omega$$

A plot of the inductance changes against applied force values is shown in Figure 7.12, where the relationship between both quantities is depicted. The measured coil resistance has been assumed to remain fairly constant within the frequency range. Initial stressing of the insert causes a large gain in the measured inductance, which then tapers off as the loading is further increased.

Another mechanism which can be used in tracking the applied force is the Q (quality) factor of the inductor coil, which is a dimensionless parameter related to the damping. It is ratio of the inductive reactance of the inductor to its series resistance, and can be evaluated at any frequency. At resonance, this becomes

$$Q_{Helmholtz} = \frac{\omega_0 L}{R} \tag{7.13}$$

The Q-factor varies directly as the measured inductance; hence a similar pattern will be observed.

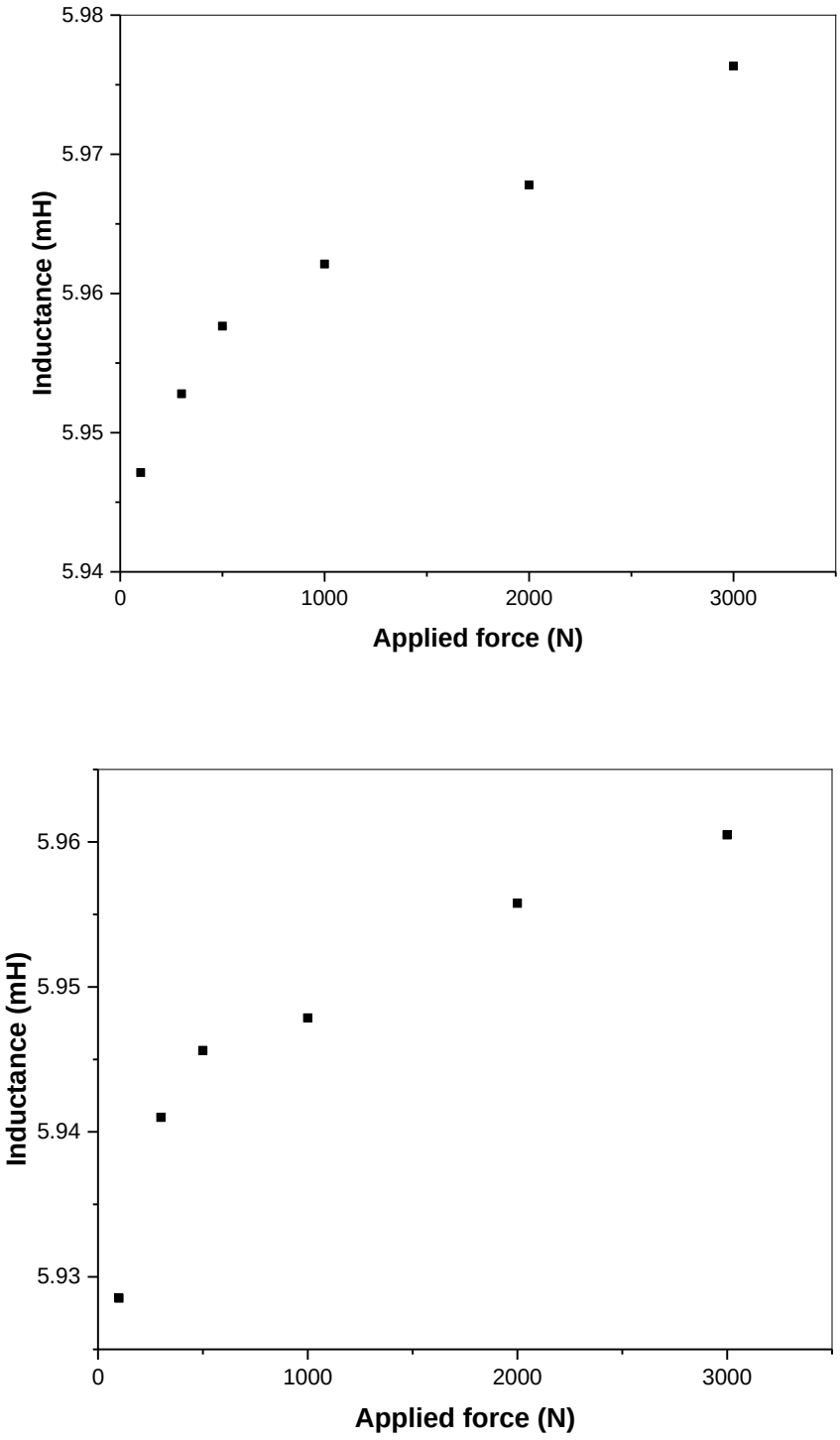

Figure 7.12 Plots showing calculated coil inductance against applied force. Top: insert 1, bottom: insert 2 (adjusted $R^2 > 0.9$**)**

Since the magnetoelastic energy in the amorphous ribbon has been linked to the strain in its domain structure, a reliable way of defining the sensitivity would be to establish a relationship between the modelled strain at the sensor surface and the measured resonant frequency variations in the coil. These plots are as shown in Figure 7.13, where it can be observed that resonant frequency declined continuously with increasing strain.

In insert 1, a shift in the resonant frequency of up to 50.5 Hz was generated by a 780 ppm change in the sensor surface strain whilst an 885 ppm strain change in insert 2 resulted in a 55.5 Hz shift in the measured frequency. This indicates a sensitivity of about 0.066 Hz/ppm in both instances, and is based on the assumption of complete stress transfer between the surface and the amorphous ribbons.

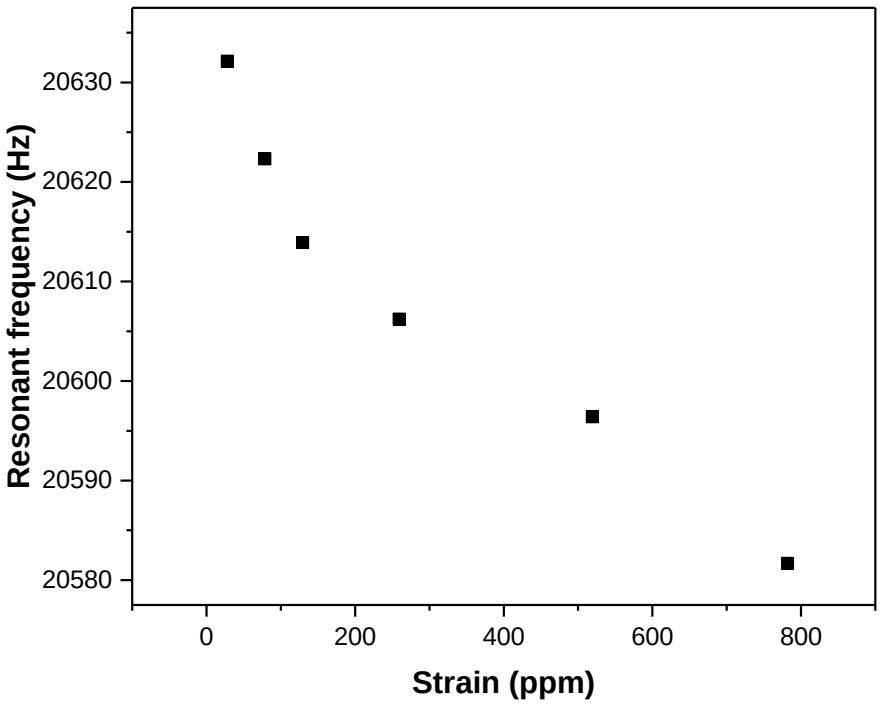

Figure 7.13a Relationship between measured resonant frequency and modelled strain (insert 1)

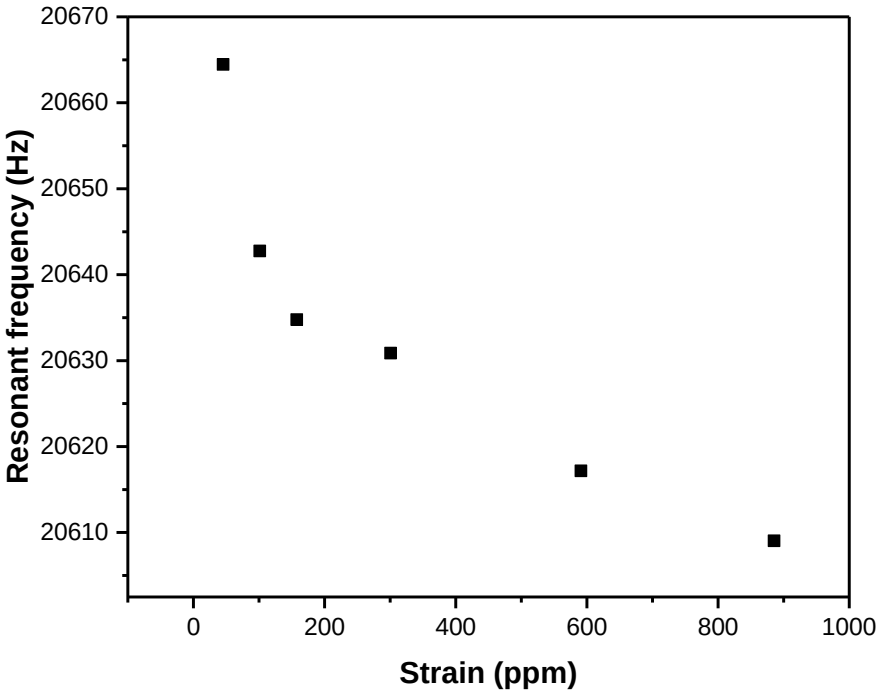

Figure 7.13b Relationship between measured resonant frequency and modelled strain (insert 2)

7.4 Summary

The objective of the work contained in this chapter was to relate the stress in the tibial insert due to the applied force to resonant frequency variations in nearby non-invasive coils. This is due to the inductance changes brought about by changes in the permeability of the embedded amorphous ribbon. It has been established that the applied force on the tibial insert surface and the sensor surface strain vary inversely with the coil resonant frequency, indicating a direct correlation between those quantities and the coil inductance.

References

[1] Kocovic, P. (2017). *3D printing and its impact on the production of fully functional components*. Hershey, PA: Engineering Science Reference, p.47.

[2] Swift, K. and Booker, J. (2013). *Manufacturing process selection handbook.* Oxford: Elsevier, p.234.

[3] 3DPKOREA – Cubeways. *DMLS process*. [online] Available at: http://www.3dpkorea.co.kr/?author=1 [Accessed 15 Jun. 2016].

8. Discussion

8.1 Analysis of experimental results

The objective of this research was to explore the potential offered by amorphous magnetostrictive ribbons as viable sensors for knee implant monitoring, through suitable harnessing of the Villari effect exhibited by these materials when externally stressed. This study has successfully demonstrated that the tibiofemoral contact pressure in knee implants can be measured non-invasively using amorphous ribbons only, without any supplementary embedded components or secondary coil windings.

The initial experiments were carried out to verify that the magnetic properties of the amorphous ribbon are measurable after encapsulation. To achieve this, the frequency dependent sensitivity of the specimens to stress was assessed at a constant peak flux density. Since the aim was to demonstrate a trend, measurements of the loaded specimen were sufficient. The data obtained indicates that the sensitivity varied directly with frequency and this is illustrated by an increasing difference in output voltage. It should be noted that this does not suggest a linear response, but only shows the changes in permeability in the ribbon when stressed. Equation 4.5 explains this, where it can be seen that the induced voltage in the coil varies directly with frequency when other determinants are kept constant.

Due to the fact that the discs utilised were produced using three different approaches, it became necessary to evaluate their sensitivities as the working principle of the proposed sensor is contingent on maximal stress transfer from the UHMWPE to the ribbon. A comparison of the output obtained suggested that the sensitivity was highest in the disc which was fabricated by fusing the UHMWPE powders with the ribbon directly. This can be credited to improved molecular adhesion between the amorphous ribbon and the UHMWPE, which relates to enhanced stress transfer as compared with those of the other manufacturing approaches. It should be noted that normalised output voltages were used for the comparisons made in order to account for the inherent stresses which were inevitably introduced during the manufacturing processes of both the amorphous ribbons and the UHMWPE discs used.

For Fe-based amorphous ribbons with positive magnetostriction, permeability increases with increasing tensile stress which results in more flux generation in the ribbon at any value of applied field. Since the induced voltage in the search coil is proportional to the amount of flux, increasing the tensile stress exerted on the material should proportionally raise the measured coil voltage. However, the results obtained in Chapter 4 showed a reduction in the induced voltage with increasing stress. This is likely due to manufacturing stresses within the amorphous ribbon which were generated during the rapid cooling process necessary to achieve its non-crystalline state. This feature was also observed in subsequent experimental work carried out; however, increased loading eliminated this irregularity.

Although it was established that most favourable manufacturing approach would be molding the UHMWPE powders directly with the ribbon, the next set of experimental work involved embedding the ribbons into two discs machined from solid blocks. This was done to ease the production process, and also to ensure uniform ribbon positioning in the samples used. Also, a solenoidal coil previously supplied the excitation whereas Helmholtz coils were utilised subsequently. In addition to providing a highly uniform area of magnetisation, they are also more practical than the solenoid for the purposes of this research as they are able to accommodate the entire joint.

It was observed that increases to the contact pressure at constant frequency steadily diminished the impedance measured across the LC circuit. As the applied force is increasing, more strain is introduced to the ribbon and ultimately, a corresponding rise in its initial permeability. As the inductance of the coil is proportionate to the effective permeability of the material contained within it, it follows that an increase in the latter will raise the former. The impedance of any inductor is directly proportional to its inductance and in a parallel tuned circuit, this is signified by a drop in the total circuit impedance. In accordance with Lenz's law, the field generated by the Helmholtz coils induces a counter-electromotive force which opposes the current flowing through the coils and this effectively attenuates the potential difference across the tuned circuit. However, this was controlled by keeping the supply voltage fixed, such that any fluctuations in the circuit parameters were purely a function of the inductance changes.

The highest sensitivity obtained was around the resonant frequency, as indicated by the steepest slope (-0.046 Ω/Pa) in the plot of impedance against contact pressure. This

correlation remained linear at all measured frequencies for peak contact pressure up to about 40 MPa, after which the variation dwindled. Despite the magnitude of the impedance varying considerably with applied pressure (over a range of 2 MΩ), the changes in the actual coil inductance were calculated to be about 2 mH which equated to a 0.13% deviation. A direct repercussion of this was that the resonant frequency seemed fairly constant over the range measured. To circumvent this, coils of lower inductance were fabricated to be used subsequently, such that small inductance changes will produce a quantifiable shift in the resonant frequency.

Prior to this point, emphasis had been placed solely on the contact pressure with hardly any knowledge of the associated stresses and strains within the inserts, particularly at the sensor surface. To gain more insight into these variables, finite element modelling was employed. In addition, modifications were made to the inserts previously utilised to better simulate the ones used in contemporary knee replacement systems. The contact pressure was observed to decrease with increasing surface area in the inserts, for any given value of applied force. This corroborates the hypothesis that wear rates are minimised with larger contact areas, since abrasive wear has been associated with contact stress.

The peak contact pressures realised varied between 6.3 - 16.3 MPa and 7.9 - 15.2 MPa in inserts 1 and 2 respectively, which fall within the reported range for assorted knee replacement systems at full extension (0^o flexion angle) and further validates the model utilised [1]. Higher values of peak contact stresses at increased flexion angles have been reported; however, this is due to the reduced tibiofemoral contact surface area as the knee flexes. Plots of the modelled strain at the sensor surface against the applied force showed a linear correlation, which implies operation within the elastic region of the stress-strain curve. This shows that the sensor configuration used in this study can also be applied to cyclic loading conditions, as little plastic deformation takes place at this surface due to the microstrain values.

To develop a proper correlation between the inductance variation and the articulating contact pressure based on the strain values derived, experiments were carried out using the same designs modelled. This time however, the lower inductance coils fabricated were used in this set of measurements and it was demonstrated that the resonant frequency as well as the tuned circuit impedance monotonically decreased with

increasing applied force. With all other parameters fixed, this suggests an increasing coil inductance value and is consistent with the established relationship between permeability and coil inductance. Also, the shape of the inductance-stress curves realised from the experiments (Figure 7.11) correlates with theoretical and modelled studies of amorphous ferromagnetic materials which further validates the proposed measurement method [2, 3]. This variation can be improved by stress-relieving the amorphous ribbons through annealing, such that externally applied forces are more perceptible. Thus, the permeability change in the ribbons will be easier to detect.

The actual forces in implants can vary depending on weight, flexion angle and the activity being undertaken. One issue that may arise with measurements taken under dynamic loading is the mobility of the system. External AC power is required to sweep the frequency of the coils, which renders the system immobile. Even though only static loading conditions were applied during this study, the sensing principle can still be measure forces at various flexion angles during different activities such as squatting, bending and sitting.

8.2 Comparison with existing research

Attempts have previously been made to monitor the forces in knee implants, mostly using non-magnetic approaches as highlighted in Chapter 3. However, these approaches necessitate the embedding of additional active electronic components for data modulation and transmission, and these components often need external powering. In addition, these supplementary components come at a cost which adds to the overall cost of the instrumented prosthesis. Furthermore, some of the designs require significant modification of the prosthesis to complement the geometrical and technical specifications of the sensors and telemetric system used.

Apart from the amorphous ribbon, the measurement procedure used in this thesis does not require any additional embedded circuitry for data retrieval. Minimal modifications were made to the UHMWPE insert, but the tibial tray and stem do not need to be adapted to accommodate any components. Also, the low magnetic field generated by the coils have no adverse effect on the human body, and these make the measurement system suitable for in-vivo observations.

8.3 Repeatability and measurement uncertainty

The repeatability of the experimental work was assessed in terms of the relative standard deviation of the measurements. For each set of measurements taken for every value of applied force, the coefficient of variation c_v in the calculated impedance expressed as a percentage is given by

$$c_v(\%) = \left(\frac{\sigma_s}{\mu}\right) \times 100$$

where σ_s is the sample standard deviation and μ is the mean value used in the analysis. The maximum coefficients of variation were 0.61% and 0.36% in inserts 1 and 2 respectively. These low values are indicative of good repeatability of the procedure.

Assuming that the errors in the voltage and current measurements taken in Chapter 7 are random and uncorrelated, the uncertainty propagation in the impedance calculation using Ohm's law can be summing the fractional uncertainties in quadrature. This is given by

$$\frac{\sigma_Z}{Z} = \sqrt{\left(\frac{\sigma_V}{V}\right)^2 + \left(\frac{\sigma_I}{I}\right)^2}$$

Where σ_V and σ_I are the sample standard deviation values of the measured voltage and current at each frequency, and V and I are the mean values used in the impedance calculation. The maximum uncertainty in inserts 1 and 2 were 0.60% and 0.51% respectively.

8.4 Limitations of this study

In determining the feasibility of utilising amorphous ribbons as sensors for measuring forces in knee implants, this study considered only axial static loading. Although it has been established that axial forces constitute about 95% of the loading in knee implants, the anteroposterior and mediolateral contributions still need to be considered in order to obtain a robust measurement system. Also, the knee implants are usually subjected to dynamic loading during various daily activities which brings about fatigue and creep in the UHMWPE; however, these have not been reflected in this study.

An assumption made in this research is that total stress transfer occurs between the sensor surface and the amorphous ribbons. This is most likely not the case, as some stress will be lost at the boundary between both surfaces due to the discontinuity. Also, additional stresses introduced into the amorphous material during the bonding process were not factored in.

The measurements were taken at ambient temperature which is lower than that in the normal human body; hence, effects of temperature variation have not been accounted for. Also, the ambient conditions inside a knee joint (due to bodily fluids and tissues) cannot be properly simulated without clinical trials, which are beyond the scope of this thesis.

References

[1] Shiramizu, K., Vizesi, F., Bruce, W., Herrmann, S. and Walsh, W. (2007). Tibiofemoral contact areas and pressures in six high flexion knees. *International Orthopaedics*, 33(2), pp.403-406.

[2] Barangi, M. and Mazumder, P. (2014). Straintronics-based magnetic tunneling junction: Dynamic and static behavior analysis and material investigation. *Applied Physics Letters*, 104(16), p.162403.

[3] Tan, E., DeRouin, A. and Ong, K. (2012). Magnetoelastic-Harmonic Stress Sensors with Tuneable Sensitivity. *IEEE Sensors Journal*, 12(6), pp.1878-1883.

9. Conclusions and future work

9.1 Conclusions

The work contained in this thesis proposes a new system for measuring forces in knee implants using a magnetic detection method. This was achieved by integrating amorphous ferromagnetic ribbons into UHMWPE inserts, and measuring the inductance changes in an adjacent coil winding due to applied stress on the insert.

The winding was connected to form part of a tuned circuit, and the variation in coil inductance was detected by evaluating the circuit impedance. The results showed a continuous decrease in this impedance with increasing applied tibiofemoral force, which indicates an increasing inductance. This is as a result of the increasing permeability of the amorphous ribbon located within the coil geometry.

The inductance changes in the coil windings were quantified by tracking the resonance of the tuned circuit whilst varying the applied stress. As expected, the resonant frequency decreased monotonically with increasing applied force, thus buttressing the established inverse relationship between the coil inductance variation and applied stress on the insert.

The described measurement system can be used for non-invasive monitoring of forces in total knee replacement prosthesis, without the need for additional embedded circuitry. This not only preserves the initial design of the prosthesis, but the associated costs of the supplementary components are reduced. Although this system is limited to the measurement of static loads, it can still be applied to measure loads at various flexion angles.

9.2 Future work

Optimal positioning of the ribbons within the insert for maximum stress transfer should be ascertained using finite element analysis. The induction of more strain in the ribbon produces greater changes in the permeability, which will consequently improve the sensitivity.

The actual strain at the sensor surface due to various applied loads should be directly determined using strain gauges. By doing this, the sensor can be better characterised to improve the accuracy of the sensitivity.

In addition, the flexion angle should be varied while applying different load values to produce a data matrix, to enable robust characterisation of the sensor.

List of publications

Okhiria, D., Giebaly, D., Meydan, T., Bigot, S. and Theobald, P. (2015). In Vivo monitoring of orthopaedic implant wear using amorphous ribbons. *IEEE Transactions on Magnetics*, 51(1), pp 1-3. DOI: 10.1109/TMAG.2014.2356715

Okhiria, D., Meydan, T. and Williams, P. (2016). Non-Invasive Measurement of Stress Levels in Knee Implants Using a Magnetic-Based Detection Method. *IEEE Transactions on Magnetics*, 52(5), pp.1-4. **DOI:** 10.1109/TMAG.2016.2521421